TABLE OF CONTENTS

Page

LIST OF TABLES

Page

LIST OF FIGURES

LIST OF ABREVIATIONS

5G	5th Generation
BGA	Ball Grid Array
CPW	Co-Planar Waveguide
CTE	Coefficient Thermal Expansion
E-LIW	Empty LTCC Integrated Waveguide
EM	Electro-Magnetic
ÉTS	École de technologie supérieure
GPS	Global Positioning System
GSM	Global System for Mobile communications
HTCC	High Temperature Co-fired Ceramic
IC	Integrated Circuit
IEEE	Institute of Electrical and Electronics Engineers
LCP	Liquid Crystal Polymer
LIW	LTCC Integrated Waveguide
LTCC	Low Temperature Co-fired Ceramic
LTE	Long-Term Evolution
PCB	Printed Circuit Board
MCM	Multi-Chip Module
MEMS	Micro-Electro-Mechanical Systems

MMIC	Monolithic Microwave Integrated Circuit
RF	Radio Frequency
SiP	System in Package
SIW	Substrate Integrated Waveguide
SMD	Surface-Mount Device
SMT	Surface-Mount Technology
SoC	System on Chip
SoP	System on Package
SRF	Self Resonance Frequency
TOS	Tape On Substrate
TRL	Thru Reflect Line
UHF	Ultra High Frequency
V-LIW	Vertical LTCC Integrated Waveguide
VNA	Vector Network Analyzer
Wi-Fi	Wireless Fidelity

LISTE OF SYMBOLS AND UNITS OF MEASUREMENTS

α_C	Conductor attenuation constant
α_D	Dielectric attenuation constant
α_R	Radiation attenuation constant
α_T	Total attenuation constant
β	Phase constant
BW	Bandwidth
c	Light Speed
C	Coupler coupling factor
η	Intrinsic impedance
$F(a)$	complete elliptic integrals of the first kind
$E(a)$	complete elliptic integrals of the Second kind
f_c	Cut-off frequency
f_0	Center frequency
k	Wave number
λ_g	Guided wavelength
$k_{i,j}$	Coupling factor between resonator i and j
ω	Angular frequency
Q	Quality factor
R_s	Surface resistivity

INTRODUCTION

In recent years, there has been a great deal of interest in miniaturized low-loss circuits which can work in small hand-held devices with limited available power. The trend to integrate as many services as possible in these devices, and also the necessity to be prepared for upcoming services impel designers to include circuits working at different bands in a single unit. For instance, a new smartphone or tablet design is expected to not only support current services like GSM, LTE, GPS and Wi-Fi at microwave frequencies, but also it has to include millimeter-wave bands for upcoming technologies like 5G at 28-40 GHz and wireless ad at 60 GHz. This will require a technology which can offer a high level of integration with excellent performance and also provide such a low-cost solution to be present in end-user devices. System on Chip (SoC) has been introduced in the late 90s to integrate all signal processing subsystems in a single silicon chip. However, the integration of analog and RF circuits on a silicon chip could be challenging. The dissimilarity of RF and digital logic circuitry enforces extra steps during the fabrication process which ultimately leads to the increase of design complexity and fabrication cost. A multi-chip module (MCM) with a combination of printed lines and ball grid array (BGA) interconnections offers an alternative solution to the restriction of integrating different components on the same chip. Using MCM, it is possible to integrate RF, optical and digital chips with different technologies in a single module. However, embedded thin-films is not still available in MCM, and certain components need their own package which leads to the presence of a relatively bulky system board. An alternative solution for the miniaturized system is offered by the System in Package (SiP) technique. In SiP, the packaged or bare chips are stacked up on top of each other to provide a 3D integrated module. However, it still needs bulky passive components and a conventional system board. System on Package (SoP) has emerged to address the challenges of other miniaturized technologies discussed here. In SoP, all subunits share a common multilayer substrate/package. In addition, the passive integration is available in SoP. It means that all passive circuits like matching networks, filters, and antenna

can directly be realized in the package substrate and unlike the surface mounted devices (SMD) there is no more need to have individual packages for each component. This converts passive components to bare thin-film components which are in the order of magnitude smaller than the packaged ones. Also, it is possible to avoid the bulky packages of integrated circuits (IC) and use their core chip in the SoP package. Moreover, the multilayer nature of the SoP concept allows realizing the circuits and interconnection both in-plane and out-of-plane between layers which ultimately make an ultra high density package available and reduce the footprint area, signal routing length and the associated delay and power consumption.

To realize all mentioned capabilities of SoP, both ceramic and organic multilayer technologies are a candidate for 3D integration at microwave and millimeter-wave frequencies. However, a ceramic technology like low temperature co-fired ceramic (LTCC) has been considerably more used in packaging industry since it has a more mature and stable process compared to organic solutions like liquid crystal polymer technology (LCP). The combination of relatively high permittivity low-loss dielectrics and high conductivity metals like silver and gold make LTCC a well-suited technology for integration and miniaturization of 3D embedded circuits which significantly reduces module and package dimensions. In the following sections, we describe the main problems, our objectives, the applied methodology, the achieved results and thesis content.

0.1 Motivation and Challenges

As it has been discussed above, LTCC is a very promising technology to realize 3D SoP concepts. However, there is still room to develop LTCC capabilities to cover more kinds of circuitry and also to provide more suitable solutions to meet requirements for upcoming technologies at higher frequencies. At microwave frequencies and below, LTCC is widely used to make lumped element components to integrate passive circuits inside the package. This reduces the size of components and also makes it possible to have compact multi-functional circuits

which ultimately lead to a significant reduction of circuits' size and weight. LTCC integrated lumped elements have better quality factor compared to lumped elements integrated by other technologies like Monolithic Microwave Integrated Circuit (MMIC). However, the circuits realized with these components still suffer from having more loss compared to bulky distributed planar circuits. Thus, improving the quality factor of these lumped components is of interest to provide solutions for circuits which need to be compact and low loss. Furthermore, till now, LTCC lumped element circuits were limited to work under 6 GHz. There are two main reasons which impose this limit, the first one is the self-resonance frequency of lumped components and the second one is the total size of the circuit which should typically be in the order of magnitude smaller than lambda to provide acceptable results as a lumped element circuit. There is continuing research to overcome these challenges to broaden the frequency range for which it is possible to design LTCC integrated lumped circuits.

In millimeter-wave frequencies, there are different challenges. In this range, lumped components are not applicable at all, and as we go to the higher frequencies, even the planar transmission lines like coplanar waveguides and microstrip become lossy. It has already been shown that substrate integrated waveguide (SIW) is a promising alternative at millimeter-wave frequencies. SIW encompasses the conventional waveguide's advantage of having a lower level of loss and also provide the easy integration capability of printed transmission lines. SIW, like any other structure, is not perfect and it has its own problems and challenges as well. Unlike the conventional rectangular waveguide, SIW is dielectric filled, and consequently, it suffers from having more dielectric loss compared to air-filled waveguides. Since in millimeter-wave frequencies and above, the dielectric loss is the dominant term in the loss performance, it is particularly of interest in these frequencies to eliminate or reduce dielectric loss and enhance SIW's loss performance. Moreover, a set of vias are required to structure SIW's side walls as well as discontinuities for applications like iris filters. As the operation frequency goes higher, the required spacing for adjacent vias becomes challenging and at terahertz frequencies, it is

almost impossible to be fabricated with the current standard ceramic fabrication process. Furthermore, the realization of E-plane structures, which is quite easy with conventional waveguides, is challenging with a conventional SIW structure and standard fabrication process. In this applications, the metallic rectangular waveguides are still widely used as an H-plane to E-plane transition. Also, SIW lines, compared to the other printed transmission lines, usually occupy more footprint area to form a similar circuit functionality. This leads to a significant reduction of available space for potential active components which can only be mounted on the surface. A multilayer fabrication technology like LTCC introduces considerable flexibility in the design of SIW circuits and it can be used to address all these challenges. Thus, it is of importance to develop and advance the multilayer ceramic fabrication techniques to improve the performance of current transmission lines, and also to design and realize new guiding structures to enhance the performance of millimeter-wave LTCC circuits.

0.2 Objectives

This research has been undertaken at Laboratoire de Communications et d'Intgration de la Microlectronique (LACIME), a leading research center which provides solutions for LTCC packaging and circuit component implementation. The objective of this thesis are to advance the state of the art techniques to realize low-loss, 3D and compact LTCC circuits at microwave and millimeter-wave frequencies. The prerequisites to accomplish this objective is to improve the performances of current guiding structures and also introduce new low-loss transmission lines which enable us to design new components and to interconnect efficiently in a 3D manner. The specific research objectives to this end are as follows:

- Investigate possible solutions to improve the performance of lumped element components at microwave frequencies.

- Broaden the frequency range in which the lumped components are applicable to reduce circuit size at microwave frequencies.
- Explore the solutions to implement low-loss transmission lines at millimeter-wave frequencies.
- Investigate potential guiding structures to transfer signal vertically to the LTCC buried layers.
- Design 3D low-loss components in LTCC at millimeter-wave frequencies to reduce the size and make circuits more compact.

0.3 Methodology

The design procedure to realize microwave and millimeter-wave circuits usually starts from a circuit model and then involves full-wave electromagnetic modeling. Next, the performances of designed circuits are tested through a fabrication and measurement process. In all these steps, especially for circuits at millimeter-wave frequencies, the designed parameters and also fabrication process might need optimization. However, as it can be seen in Fig. 0.1, complexity, accuracy and the required time to modify and optimize a design are different at these steps. While the optimization of a parameter in an analytical model could be very fast, the modification of a fabricated circuit is a time consuming and costly process and in many cases needs to re-fabricate the entire circuit. Thus, it is of interest to push the load of optimization toward the earlier steps of realization procedure. This could be done by accurately identifying the materials' properties to increase the precision of modeling in full-wave EM simulators and also by meticulously adjusting analytical and circuit models to better reflect the behavior of a circuit. Based on this discussion, the necessary steps toward achieving the goal in each section of the thesis are as follow:

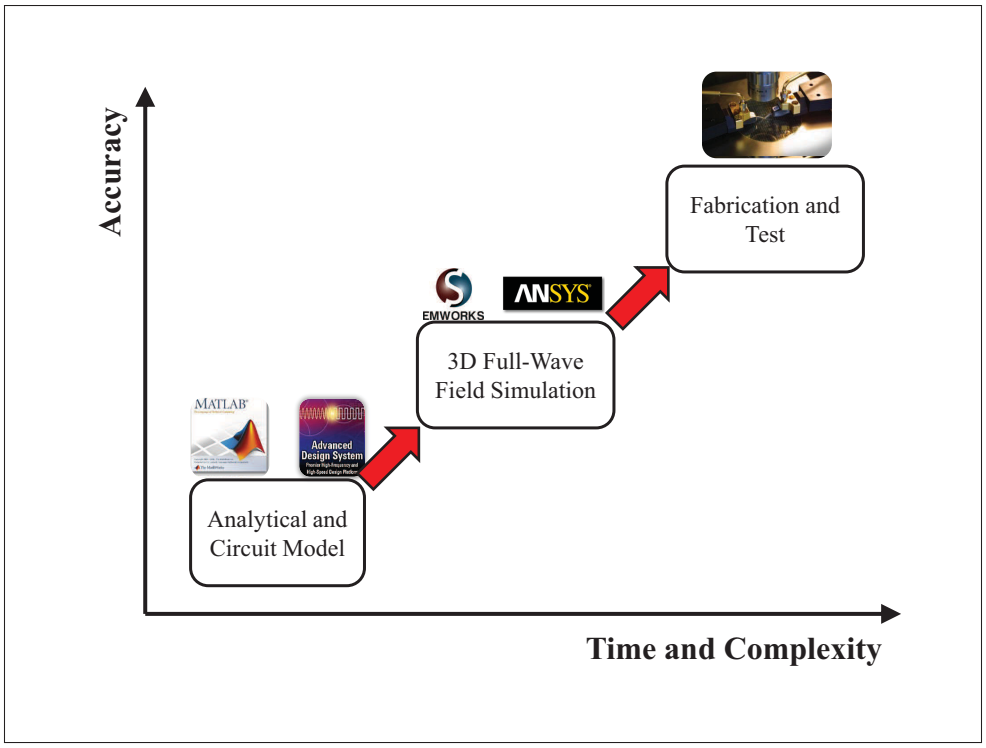

Figure 0.1 Circuit realization process

a. **Design and simulation:** In this step, the desired circuits have been designed and modeled. Whenever an analytical model is available, it has been used to find initial values for different circuit parameters like physical dimensions, coupling, resonances, etc. Afterward, 3D models of the designed circuits have been simulated using full-wave commercial software and each component optimized to provide the best possible results. In certain cases, using the simulation results, the analytical model has been modified to fully present our special cases for future applications. The tools which have been used for analysis and design models are mainly MATLAB and ADS to process analytical and circuit models, and ANSYS Electronics and HFWorks to perform electromagnetic (EM) simulation and optimization.

b. **Fabrication:** The designed components and circuits have been fabricated in LTCC. In this step, the fabrication constraints have been considered, and in many cases, the cur-

rent fabrication process has been upgraded, and new techniques have been developed to provide better and more precise solutions to realize special ultra low-loss structures.

c. **Test and validation:** Each component has been tested after fabrication. Proper TRL calibration kits have been designed and fabricated for each substrate and circuit to remove the impacts of probes and transitions. Furthermore, a Keysight PNA-X network analyzer has been used to carry out the measurement. The results have been compared with EM simulation results. In certain cases, when there was a divergence between results or fabrication process had imposed some limitations, the EM models have been modified based on the measurement results and circuits have been re-fabricated and measured.

0.4 Thesis Contributions

The major contributions of this thesis are listed below:

a. In Chapter 1, we investigate solutions to improve the performance of lumped element components realized in the LTCC substrate. We proposed a new structure to realize float conductors in LTCC. With the aid of these floated conductors and air-cavities under the lumped components, we proposed suspended inductors and capacitors. The suspended components show significantly better loss performance compared to conventional lumped elements integrated by LTCC in terms of both quality factor (Q) and self-resonance frequency (SRF). Using this technique, several virtually suspended inductors and capacitors have been fabricated and successfully measured. For inductors, we achieved a 23 percent improvement for Q while SRF is increased by 70 percent. Furthermore, the designed suspended capacitor shows at least 50 percent improvement for Q and slightly better SRF. Furthermore, using these high-SRF lumped components, a KU band pass-band filter has been designed and successfully measured for the first time.

b. In Chapter 2, we provide a solution to improve the performance of LTCC Integrated Waveguides. In order to reduce insertion loss of this guiding structure, we propose a design technique to realize Empty LTCC integrated waveguides (E-LIW). In our designed E-LIW, we not only implement the air cavities to reduce the dielectric loss but also we used the long rectangular vias in the sidewalls to reduce radiation loss. Moreover, since the designed empty guiding structure has a wider width for the same cut-off frequency, it has lower conductor loss as well. Thus, this technique eventually leads to minimize losses. The proposed structure shows a simulation insertion loss of 0.084 dB/cm at 60 GHz which is considerably better compared to 0.48 dB/cm for the conventional SIW structure in LTCC. Moreover, a ultra compact transition between E-LIW and CPW is proposed in this chapter. A back-to-back configuration including the proposed transition and E-LIW has been fabricated. Measurement results show a maximum total insertion loss of 0.5 ± 0.2dB with better than 20 dB return loss for the entire structure and over the entire frequency band of interest.

c. In Chapter 3, a new vertical guiding structure in LTCC is proposed. This Vertical LTCC Integrated Waveguide (V-LIW) allows designing devices in which out-of-plane structure is needed. Also, it helps us to realize transparent transition and interconnection to the buried at very high frequencies, potentially up to several THz. This vertical integration leads to considerably economize footprint area as well. Moreover, the main building blocks for this new transmission line are presented. This includes a transition to the standard waveguide, a transition to planar printed lines, a 90-degree bend, and a T-junction. These blocks enable us to design a wide variety of passive circuits using V-LIW. Furthermore, applications to the design of V-band and W-band filters, couplers and power-dividers are presented. Several prototypes are fabricated with measurement results showing good agreement with simulation data.

0.5 Content

This thesis follows the paper-based format of ÉTS. Hence, each chapter represents one journal paper as follows:

a. Chapter 1 presents suspended lumped element components which are high Q and high SRF lumped components in LTCC. Also, a KU-band pass-band filter presents using these components for the first time. The related paper was submitted to IEEE Transactions on Components, Packaging and Manufacturing Technology.

b. Chapter 2 discusses the implementation of empty LTCC integrated waveguide and presents a new transition from E-LIW to conventional LIW. The related paper is published in IEEE Microwave and Wireless Components Letters.

c. Chapter 3 introduces a new vertical LTCC integrated waveguide. Transitions to this new guiding structure and also implementations of several circuit components is presented in this paper. The related paper is accepted by IEEE Transactions on Microwave Theory and Techniques.

d. Finally, in Conclusion and Recommendations, we summarize the results of this thesis and proposed several directions as the possibilities of future studies.

0.6 Literature Review and Background on Technologies for LTCC Integrated Circuits

In this sub-chapter, we present a general overview of LTCC fabrication process and also brief review on research have been carried out in the literature on related areas. Since the thesis has been written to follow the paper-based format on ÉTS, each chapter includes its own relevant literature review and discuss how our work contributes to the literature which is partly repeated here.

0.6.1 LTCC fabrication technology

Low Temperature Co-fired Ceramic (LTCC) is a multi-layer, glass ceramic substrate which is co-fired with low resistance metal conductors, such as Ag, Au, and Cu, at low firing temperatures. In the literature, the term "co-fired ceramic" refers to the supporting ceramic structure and any dielectric, resistive, and conductive materials which are fired in a kiln simultaneously, meanwhile the term "low temperature" refers to the fact that the sintering process occurs in less than 1000^{o}C.

A typical LTCC module could consist of several dielectric tapes, connecting vias, external and internal conductors and passive components. Resistors, inductors, and capacitors can be fabricated in LTCC circuits as buried or surface components. Manufacturing of LTCC circuits has several steps as shown in Fig. 0.2. Cutting of single green-sheets (the term for unfired tapes) is the first step of fabrication, and then vias are punched or laser drilled into the green-sheets. The next step is to print conductor lines on the surface of each layer. Finally, these single sheets have to be stacked, laminated and fired together. This fabrication process can save time and money because every single layer can be checked and replaced before firing if it is damaged or built inaccurately; this prevents the need of manufacturing a whole new stack-up.

0.6.2 Advantages of LTCC technology

LTCC has widely been used both by researchers to design circuits for upcoming technologies and by industrial companies to provide solutions for packaging. The reasons that make LTCC an exceptional candidate for the wide variety of applications are discussed in the following. These reasons along with a mature and stable fabrication process as well as the high permittivity dielectrics make ultra miniaturized LTCC circuits feasible.

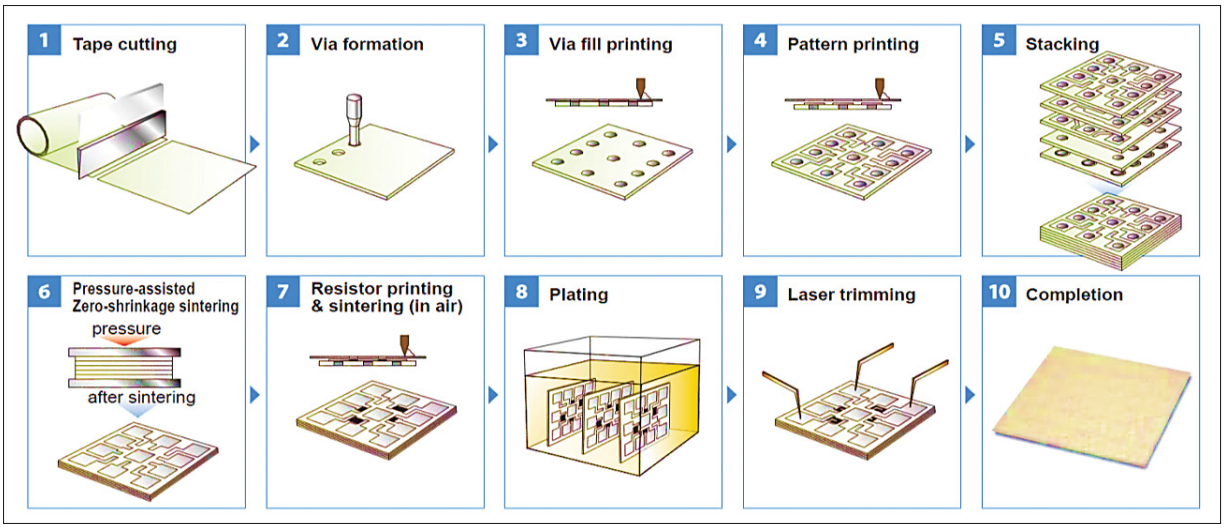

Figure 0.2 Manufacturing process of LTCC (MuRata)

0.6.2.1 High frequency characteristics

What makes LTCC suitable for high frequency applications is its low loss. The high frequency transmission loss can be expressed mainly as the combination of conductor loss and dielectric loss. Dielectric loss is directly related to dielectric loss tangent. Ceramics which are used in LTCC has several times lower loss tangent compared to resin materials. Fig. 0.3 shows signal attenuation due to conductor loss and dielectric loss. As it can be seen in this figure, at frequencies above 1 GHz the effect of dielectric loss is dominated, and the impact of it becomes more conspicuous as frequency increases. On the other hand, since the firing temperature for LTCC is lower than 1000^{o}C, it allows using conductors with a lower conductive loss such as Au or Ag. This does explain why at millimeter-waves, LTCC is a better choice than high temperature co-fired ceramics (HTCC). HTCC is a low-loss aluminum oxide dielectric which must be sintered at about 1600^{o}C. Thus, only conductors with high melting points like molybdenum (Mo) and tungsten (W) are available. The conductivity of these conductors is about 50 times less than silver or gold.

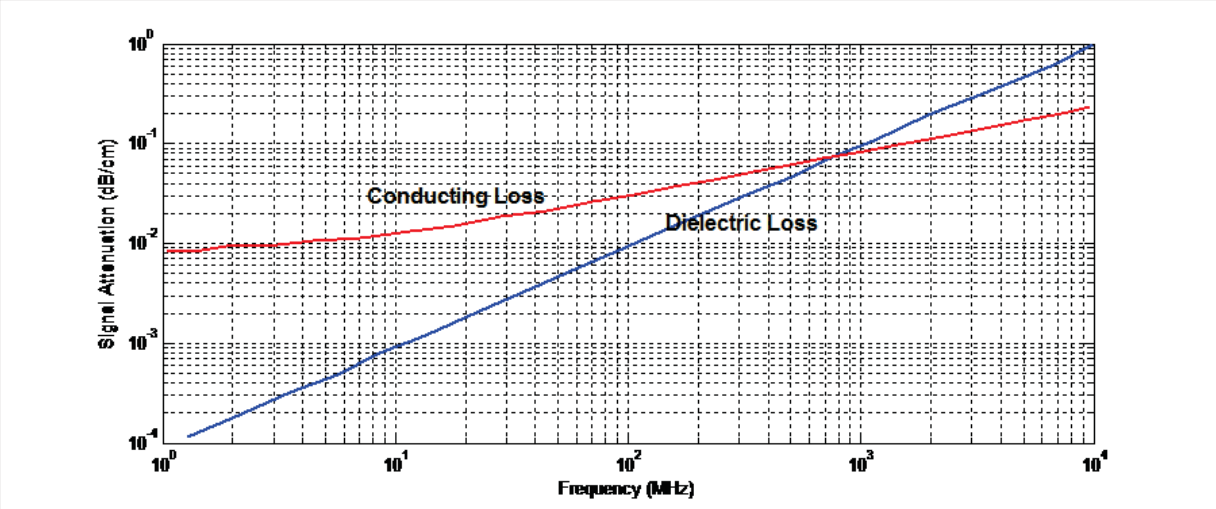

Figure 0.3 Effect of dielectric and conductor loss in signal attenuation (Imanaka (2005))

0.6.2.2 Thermal stability

Assembly process such as soldering electronic components and also reliability tests before shipment can impose certain heat stress on circuit boards and packages. These stresses could lead to the interconnection between board and components lose their connection reliability. LTCC dielectrics have better thermal resistance and thermal expansion coefficient compared to resins, so they offer better product reliability at high temperatures. This is because the substrates are expected to have a thermal coefficient close Si (4.2 ppm/^{o}C) to avoid interconnection cracks due to shrinkage mismatch. A typical LTCC ceramic has a CTE between 5 to 8 ppm/^{o}C while Epoxy resin has a CTE between 30 and 40.

0.6.2.3 Integration of passive components

Integrating various passive components in a single stack-up helps to shorten the interconnection length and also reduce the number of components needs assembly. This eventually leads to a better loss performance and less failure risk. A particular dielectric with a specific permittivity is only suitable for a range of passive components like two or three decades of capacitors. In the

process of manufacturing LTCC circuits unlike resin printed circuit, it is possible to stack and integrate green sheets of different kinds of materials in order to embed passive functions in the substrate. For an instant, as shown in Fig. 0.4, the passive circuit stack-up is a combination of a material with a low dielectric constant of around 5 for high frequency low loss signal routing, a medium dielectric constant material of around 15 which can be used to realize a compact filter, and a material with a high dielectric constant of around 1,000 or more for components like DC coupling capacitors to eliminate signal noise and provide a clean power source (Imanaka (2005)). Thus, using LTCC lead to making the board itself smaller and reducing the parasitic effects.

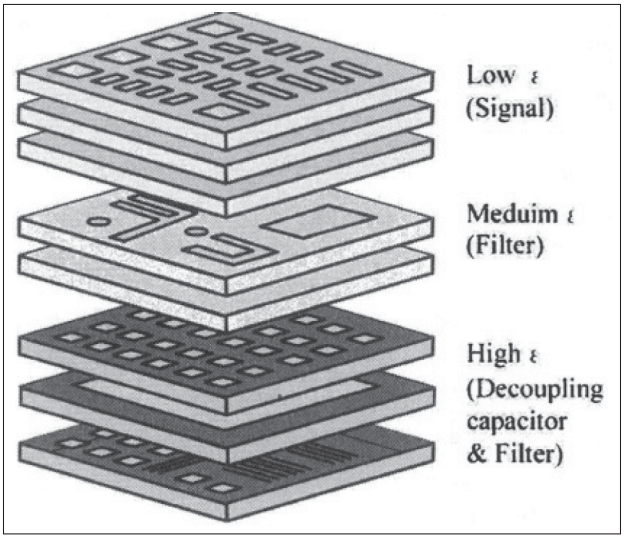

Figure 0.4 Passive components embedded in substrate (Imanaka (2005))

0.6.3 LTCC process challenges

Despite all the interesting features of the LTCC process, it still suffers from several drawbacks. First and maybe the most important one is the shrinkage issue. Most kinds of LTCC ceramic are shrunk in all direction after lamination and sintering. The shrinkage factor is a function of consisting material mainly and also the amount of conductor on each layer. At low frequency,

this could be easily compensated by enlarging the circuit. However, at very high frequencies or when a tight tolerance in dimensions needed, the compensation becomes challenging, and it needs a test prototype and precise measurement of dimension before the final fabrication. This could increase the cost and lead time to the market needed for a product. In recent years, companies like MuRata and Asahi Glass Co. offers materials with zero shrinkage in X and Y direction by solutions like tape on substrate (TOS). These solutions partly solved the problem, however, increase the cost of manufacturing. The other problems which degrade the performance of LTCC circuits particularly at millimeter-wave frequencies are a coarse metal definition and a poor surface finish. A typical fabrication design rule for volume production allows line width and spacing of about 100 μm with a tolerance of $\pm 5\%$ and a surface roughness of about 2 μm. This level of surface roughness makes it impossible to integrate MEMS devices directly on the LTCC substrate. To address these challenges, the laser processing of LTCC tapes are presented in (Shafique *et al.* (2009); Shafique & Robertson (2011)) to make the line width as narrow as 50 μm feasible. Furthermore, a pre-treatment method of backed stack-up to achieve very fine surface are introduced in (Bahloul *et al.* (2016)). The polishing technique presented in that work provides a surface with a sub-micron roughness which is suitable for MEMS circuits. However, both the laser processing and polishing of LTCC circuits increase the fabrication cost significantly which is not acceptable for demands for low-cost mass production solutions.

0.6.4 LTCC lumped element circuits for microwave frequency application

Integrated lumped element circuits are widely used as a miniaturized technique to realize ultra small circuits at different bands, from several megahertz (Zhou *et al.* (2014b)) to several gigahertz (Qian & Tang (2011)). At the heart of any lumped element circuits, there are lumped inductors and capacitors which with different configuration provide different functionalities such as filter, coupler, duplexer, etc. The intrinsic 3D capability of LTCC motivates researchers to

carry out a considerable number of works on LTCC integrated lumped components which only the most important ones are included here.

The lumped elements made in LTCC are introduced for the first time in (Brown *et al.* (1993)), and it was followed by (Wilcox *et al.* (1997); Eurskens *et al.* (1998)). These are early works which only explored the feasibility and simulation techniques to design integrated inductors, capacitors and resonators. The development of integral capacitance has been discussed in (Delaney *et al.* (1999)). In (Sutono *et al.* (1999b)), the performance of a multilayer helical inductor has been investigated. Furthermore, multilayer capacitors and inductors have been used in the development of a power amplifier module in (Sutono *et al.* (2001)). A similar approach to realize LTCC integrated lumped element has been used in numerous other published reports till recent years. In many of them, the main efforts were dedicated to miniaturize circuits either by placing circuit components extremely close to each other in a 3D configuration (Brzezina & Roy (2014)) or by realizing dual-band (Joshi & Chappell (2006)) and multi-functional (Mousavi & Kouki (2016)) devices. Despite all the interesting results have been reported in those works, those lumped circuits suffer from a higher level of loss compared to the alternative circuits realized by the bulky distributed planar transmission lines. Also, the relatively large parasitic capacitance and inductance, due to the presence of high permittivity dielectric between components and ground, push the SRF toward lower frequencies and consequently limit the range where these components are applicable.

Improving the performance of LTCC integrated lumped elements has also been the target of several works. In (Mousavi & Kouki, 2015), the capacitor is connected to the ground by several vias instead of one via to reduce the parasitic inductance and increase SRF. Furthermore, an air-filled cavity has been added under a solenoid inductor in (Aliouane *et al.*, 2011) to increase Q. The same has been used for a spiral inductor in (Eun *et al.*, 2004) to increase both Q and SRF. However, in both works, an extra layer of ceramic is needed to support the inductor's arm.

This layer has a negative impact on loss performance and prevents us to achieve the maximum gain of this technique. It should also be pointed out that in all discussed literature the operation frequency is under 6 GHz. Thus, using conventional methods, we still have to use bulky planar circuits or waveguide structures at microwave frequencies above 6 GHz.

0.6.5 LTCC integrated waveguides

Substrate integrated waveguides have been introduced in (Deslandes & Wu (2001a)) to bring the advantages of rectangular waveguides to the printed circuit boards. Thus, with certain compromises, both convenient integration of printed circuits and low-loss high-power performance of rectangular waveguides becomes available. This planar form of waveguides is particularly of importance in millimeter-waves where they provide a promising alternative for lossy conventional planar transmission lines with an acceptable dimension. This new guiding structure has been of a great deal of interest in last decade and without any exaggeration thousand of articles have been published on that.

Multilayer fabrication technologies, especially LTCC, are well suited to develop the SIW circuits. The inherent flexibilities of these technologies allow to design more complex 3D structures and add more functionalities to a circuit. The first LTCC integrated waveguide has been presented in (Li *et al.* (2003)). Since then, it is widely used to realize variety of circuits such as filter (Zhang *et al.* (2015)), duplexer (Wang *et al.* (2014)), antenna (Cheng *et al.* (2013)).

Although SIW in many ways facilitates integration and realization of the millimeter-wave circuit, it has several drawbacks compared to conventional standard waveguides. First of all, it is a dielectric filled transmission line and suffers from having a dielectric loss. This issue has been the focus of the research in (Belenguer *et al.* (2014)) and (Parment *et al.* (2015b)). In those works, an air-filled SIW for PCB circuits has been presented and also each one proposed a transition from air-filled to the dielectric-filled SIW. However, the transition in (Parment *et al.*

(2015b) is extremely long, and the proposed transition in (Belenguer *et al.* (2014)) is not applicable to LTCC circuits and millimeter-waves. The other important drawback of SIW circuits is the fact that it is difficult to realize the circuits in which an out-of-plane structure is needed. In (Doghri *et al.*, 2015), it has been tried to address this problem by introducing a 3D SIW structure. However, the proposed structure in that paper, is bulky and difficult to integrate which means it eventually misses the key reasons to implement SIW, Furthermore, as another drawback it should be noted that SIW circuits compared to other planar printed circuits usually take more footprint area which could be very precious in design of ultra-small module where too many active and passive devices have to be integrated in a limited area.

CHAPTER 1

DIELECTRIC-FREE SUSPENDED LTCC LUMPED ELEMENTS WITH A NOVEL CONDUCTOR STRUCTURE FOR LOW-LOSS INTEGRATED SYSTEMS

Aria Isapour [1], Aref Pourzadi [1], Ammar Kouki [1]

[1] Département de Génie Électrique, École de technologie superieure ,
1100 Notre-Dame Ouest, Montréal, Québec, Canada H3C 1K3

Manuscript submitted to IEEE Transactions on Components, Packaging and Manufacturing Technology in July 2018.

Abstract

This paper proposes a solutions to improve the performance of lumped element components realized in Low Temperature Co-fired Ceramic (LTCC) substrates. Thanks to the flexibility and precision of LTCC fabrication process, with a combination of inner air-cavity and virtually thick metals, we are able to make our lumped components suspended. This eventually eliminates dielectric loss and enhance quality factor (Q) and self resonance frequency (SRF) of our designed components. Using this technique, several inductor and capacitors have been fabricated. For suspended inductors, an improvement of atleast 23 percent and 70 percent have been achieved for Q and SRF respectively. Also, suspended capacitors have shown that they can provide a significantly better Q with a slightly better SRF compared to the conventional LTCC integrated capacitors. Furthermore, with the aid of these high Q and high SRF lumped components, a KU band pass-band filter has been designed and successfully measured for the first time. The fabricated filter has a insertion loss of 2 dB in the middle band with a total size of 2.5 mm by 4.1 mm.

Introduction

progress of multi-functional wireless products has led to a continuously increasing demand for high performance, low cost, miniaturized and lightweight circuits which can fit in small

hand-held devices and which can work for a long time with small batteries. Low Temperature Co-fired Ceramic (LTCC) technology, with an almost arbitrary number of low-loss dielectric layers and high conductivity metals like silver and gold, is well-suited to provide solutions to such demands. The intrinsic 3D capability of LTCC technology makes it a superior choice to design compact lumped element passive components and circuits. It has already been shown in the literature that LTCC lumped element components do not suffer from the integration limitation of alternative solutions like surface mounted technology (SMT) components in ultra-small circuits (Wu *et al.*, 2004; Sutono *et al.*, 2001). Furthermore, LTCC lumped components offer the possibility of providing continuous elements values rather than discrete ones since they can be properly dimensioned during the design process. The monolithic integration of different lumped LTCC components in single design can also be an advantage for size and part-count reduction.

Since the first appearance of lumped element components in LTCC (Eurskens *et al.*, 1998), considerable research has been carried out in this area. While certain researchers focused on the realization of different RF circuits (Mousavi & Kouki, 2016; Brzezina *et al.*, 2009; Brzezina & Roy, 2014; Zhou *et al.*, 2014b; Joshi & Chappell, 2006), others explored the ways to improve the performance of LTCC lumped element components (Aliouane *et al.*, 2011; Mousavi & Kouki, 2015; Eun *et al.*, 2004; Bahl, 2003). The performance of lumped components in LTCC like any other fabrication technology is limited by loss factors and parasitic capacitors (or inductors). Since, metals with highest conductivity are already available for LTCC circuits, the main focus to enhance the performance has been on reducing dielectric loss and designing structures with lower parasitic values. In (Aliouane *et al.*, 2011), the performance of a solenoid RF inductor has been compared to a spiral inductor, and it has been shown that the former one can provide better quality factor (Q). However, there is almost no improvement in self-resonance frequency (SRF) reported. An air-cavity has been added under a solenoid inductor in (Mousavi & Kouki, 2015) to increase SRF and Q. Using this technique, about 25 percent improvement in Q has been achieved for an inductor in UHF band. The impact of having several grounding vias on the performance of a capacitor was also investigated

in (Mousavi & Kouki, 2015) and and a 23 percent improvement in SRF was reported. An air-cavity has also been used under a spiral inductor in (Eun *et al.*, 2004) where an inductor having an inductance of 2.62 nH, a Q of 51 and a SRF of 9.1 GHz was reported. In all of the above cited studies where an air-cavity was used, an extra layer of the ceramic had been left between the air-cavity and inductor's arms. This extra layer is unavoidable for the mechanical integrity of their design and it negatively impacts the performance improvement provided by this technique. Furthermore, to the best knowledge of the authors, all reported LTCC passive lumped elements are limited to the frequencies below 6 GHz.

In this paper, a new technique that combines the use of inner air-cavities with a new thick suspended conductor structure is proposed to virtually eliminate all dielectric loss from LTCC lumped components. These novel lumped components offer significant performance improvement that enable their use at much higher frequencies. Various lumped component designs are presented and used for the design of a Ku band pass-band lumped element filter for the first time.

The remainder of this paper is organized as follow: in section II, a theoretical summary of key performance metrics and trade-offs in the design of LTCC lumped elements is presented. Section III presents the proposed suspended thick metal structure and its fabrication process. Simulation and measured results for several suspended inductors and capacitors are also presented in this section. Section IV presents the design, fabrication and measurement of a Ku-band lumped element pass-band filter. Finally, conclusions are given in section VI.

1.1 Non-Ideal models for lumped components

In order to quantify the impact of dielectric on lumped element performance and to assess the trade-offs possible, we consider the basic models for LTCC inductors and capacitor.

1.1.1 Inductors

The geometry of a typical LTCC integrated inductor and its equivalent one-port lumped element circuit are depicted in Fig. 1.1 where L is the inductance, R the series resistance, C_c the fringing capacitance between conductor turns, C_{sub} the capacitance between the inductor line and ground, and G_{sub} is the conductance representing the dielectric loss in the substrate. From this circuit model one can easily find the input impedance of a non-ideal inductor by:

$$Z_{in} = \frac{j\omega(L - \omega^2 L^2 C - R^2 C) + A}{B} \tag{1.1}$$

where

$$A = R^2 + \omega^2 R^2 LC + \omega^2 L^2 G + \omega^2 LRC$$

$$B = (1 + RG - \omega^2 LC)^2 + \omega^2 (GL + RC)^2$$

$$C = C_{sub} + C_c$$

Subsequently, the effective inductance is calculated by taking the imaginary parts of the input impedance, namely:

$$L_{eff} = \frac{im(Z_{in})}{\omega} = \frac{1}{B}(L - \omega^2 L^2 C - R^2 C) \tag{1.2}$$

The self-resonance frequency can be calculated by setting the imaginary part of the input impedance equal to zero (Bahl, 2003). Thus the SRF of the inductor is given by:

$$SRF = \frac{1}{2\pi}\sqrt{\frac{1}{LC} - \frac{R^2}{L^2}} \tag{1.3}$$

At microwave frequencies, a widely used equation for finding the quality factor Q from the input impedance below the SRF is Bahl (2003):

$$Q = \frac{im(Z_{in})}{re(Z_{in})} = \frac{\omega(L - \omega^2 L^2 C - R^2 C)}{R^2 + \omega^2 R^2 LC + \omega^2 L^2 G + \omega^2 LRC} \tag{1.4}$$

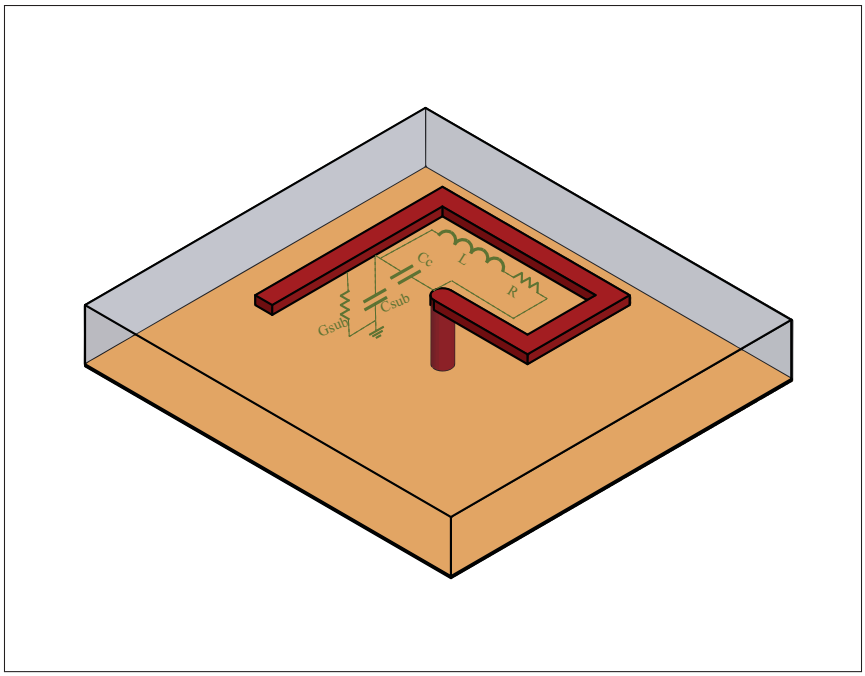

Figure 1.1 Geometry of LTCC integrated inductor

Since increasing performance of an inductor means higher Q and higher SRF, we examine (1.3) and (1.4) to see how this can be achieved for a given effective inductance value. From (1.3), it is clear that decreasing C and R while L is fixed leads to an enhancement of the SRF. Equation (1.4) also shows that by decreasing C and R, as well as decreasing G, one can increase the Q. Removing dielectric, i.e., air-cavities, reduces C, by reducing C_{sub}, while at the same time reducing G. In this paper we will seek to achieve the highest possible reduction of C_{sub} and G by completely eliminating any supporting LTCC layers between the conductor and ground. Reducing R is achieved by using high conductivity thick metal, here we use 8 μm Silver.

1.1.2 Capacitor

Fig. 1.2 depicts the geometry of a typical parallel plate LTCC capacitor and its equivalent one-port model where C is the capacitance between printed metal plates, C_{sub} the parasitic capacitance between the top metal plate and ground, L_s and R_s the inductance and resistance of the via to ground, and G_{sub} is the conductance representing the dielectric loss in the substrate.

Using this model, the input admittance of a non-ideal capacitance can be written as:

$$Y_{in} = j\omega C_{sub} + \frac{j\omega(C - \omega^2 C^2 L_s - G^2 L_s) + A2}{B2} \tag{1.5}$$

where

$$A2 = G_{sub} + RG_{sub}^2 + \omega^2 R_s C^2$$

$$B2 = (1 + RG_{sub} - \omega^2 CL_s)^2 + \omega^2 (G_{sub} L + R_s C)^2$$

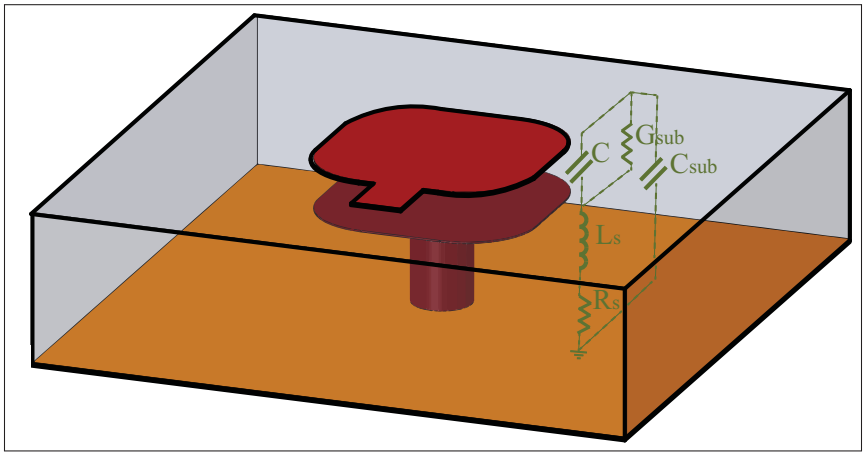

Figure 1.2 Geometry of LTCC integrated capacitor

The effective capacitance can then be extracted from the input admittance by:

$$C_{\text{eff}} = \frac{im(Y_{in})}{\omega} = C_{sub} + \frac{1}{B2}(C - \omega^2 C^2 L_s - G_{sub}^2 L_s) \tag{1.6}$$

The SRF can be found by setting the imaginary part of input admittance equal to zero, and it is given by:

$$SRF = \frac{1}{2\pi}\sqrt{\frac{1}{CL_s} - \frac{G_{sub}^2}{C^2}} \tag{1.7}$$

where C_{sub} has been neglected given that in the vicinity of the resonance frequency the imaginary part of the input admittance has a large slope changing from a big positive number to a big negative one.

Q can be found from (1.5) by:

$$Q = \frac{\omega(C - \omega^2 C^2 L_s - G^2 L_s)}{G_{sub} + R G_{sub}^2 + \omega^2 R_s C^2} \tag{1.8}$$

LTCC capacitors with quality factors around 100 are not uncommon. However, much lower Q is often obtained when using low-cost low-frequency ceramics with higher loss tangents, e.g., Dupont 951 vs Dupont 9K7 or Ferro L8 vs Ferro A6M, or when parallel capacitors require long ground vias. In these cases, the Q, as well as the SRF, can be improved by reducing G_{sub}, L_s and R_s in (1.7) and (1.8). The chosen solution for reducing G_{sub} has already been discussed in the previous subsection and will be used here as well. However, having an air-cavity inside the capacitor, while it increases Q and the SRF, does reduce the capacitance which can be compensated by increasing the capacitor size. For reducing the series inductor and resistor, L_s and R_s the length of capacitor arms in both ends should be made as short as and as wide as possible.

1.2 Suspended conductor: a proposed configuration to enhance performance

1.2.1 Fabrication process

The use of air cavities in inductor design, has been tested in (Mousavi & Kouki, 2015; Eun *et al.*, 2004) and shows promising results. However, in these works, an extra layer of ceramic was left under the inductor to mechanically support the inductor's arm. While such air cavities help reduce C_{sub} and G, having this extra layer limits the performance of the designed inductors. To achieve further reduction in C_{sub} and G, this extra layer must be removed resulting in a suspended conductor. This leads to structural challenge of how to support the conductor. To this end, we propose a new technique that exploits the flexibility of LTCC technology. Indeed, by modifying in the standard fabrication process, the realization of these floating conductors becomes feasible through the following steps.

Step 1: Fig. 1.3 illustrates the proposed modified LTCC process where a single sheet of green tape is used to realize the suspended conductor. The suspended conductor achieves its structural integrity by being printed on both sides of the single sheet with interconnection between the two sides achieved through an array of vias. While via punching and fabrication follows the standard LTCC process, double sided printing required minor process adjustment. The resulting structure works like a virtually thick line at frequencies at which the spacing between the vias is considerably smaller than the corresponding wavelength.

Step 2: the next step is the drilling of internal cavities in each layer. After that, these layers are stacked on top of each other. All the internal cavities are filled with fugitive tape to maintain the structural integrity of green tape stack during the lamination process. The fugitive tape used for this purpose is the LTCC carbon tapes (TCS-CARB-1).

Step 3: the firing process is modified to allow the fugitive tape to completely burn out in order to obtain a clean internal cavity. The modified firing profile for LTCC 9K7 is shown in Fig. 1.4. This profile, compared to the standard profile, has been prolonged in three sections: (i) at 350^{o}C for 60 minutes (ii) at 710^{o}C for 60 minutes and (iii) at 850^{o}C. These three plateaus in firing recipe allow burning completely out all binder components and residual carbons before LTCC pore closure and leave a clean inner cavity .

1.2.2 Validation

To validate the performance of the proposed solution and assess the performance gains that can be achieved, two LTCC inductors of 2.5 nH and 5 nH, were designed and fabricated in two different versions: (i) conventional and (ii) suspended, using Dupont 9K7 green tape with permittivity of 7.1 and loss tangent of 0.001. Fig. 1.5 shows photographs of the two suspended inductors. All inductors were measured using Rohde and Schwartz ZVA vector network analyzer. Fig. 1.6 to Fig. 1.9 show the measured inductance and Q of the conventional and suspended inductors. From these figures, it is evident that both SRF and Q are significantly improved by using air-filled cavities and suspended conductors.

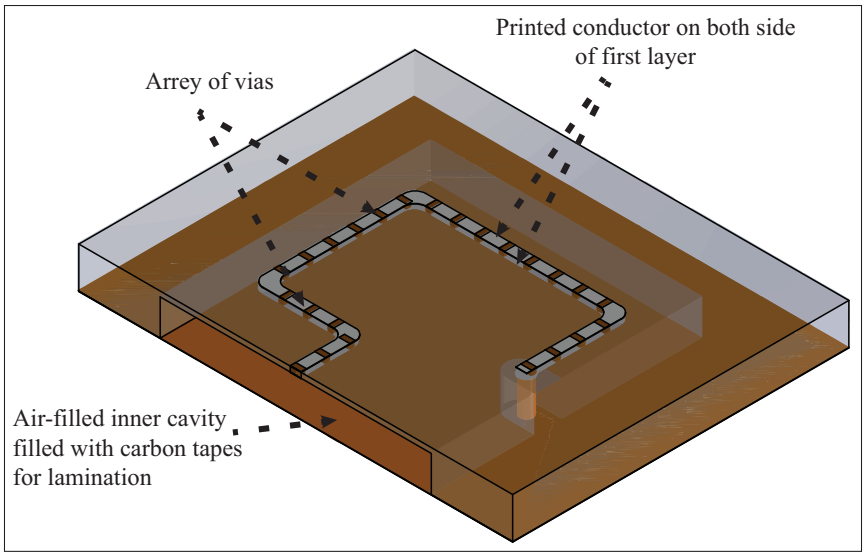

Figure 1.3 Geometry of the designed inductor with suspended conductors and inner air-cavity

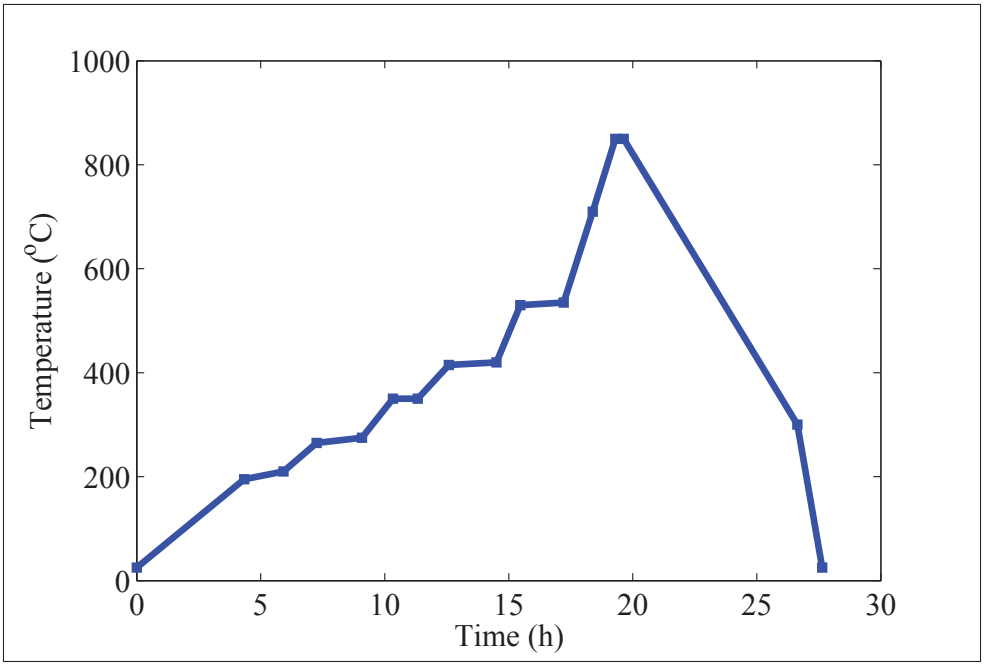

Figure 1.4 The modified firing profile of 9k7 LTCC green tapes

Table 1.1 compares the results of the proposed suspended inductors to several of the best LTCC inductors reported in the literature. As can be seen in this table, the proposed solution outperforms all reported inductors in both Q and SRF with improvements in Q of at least 50% and in

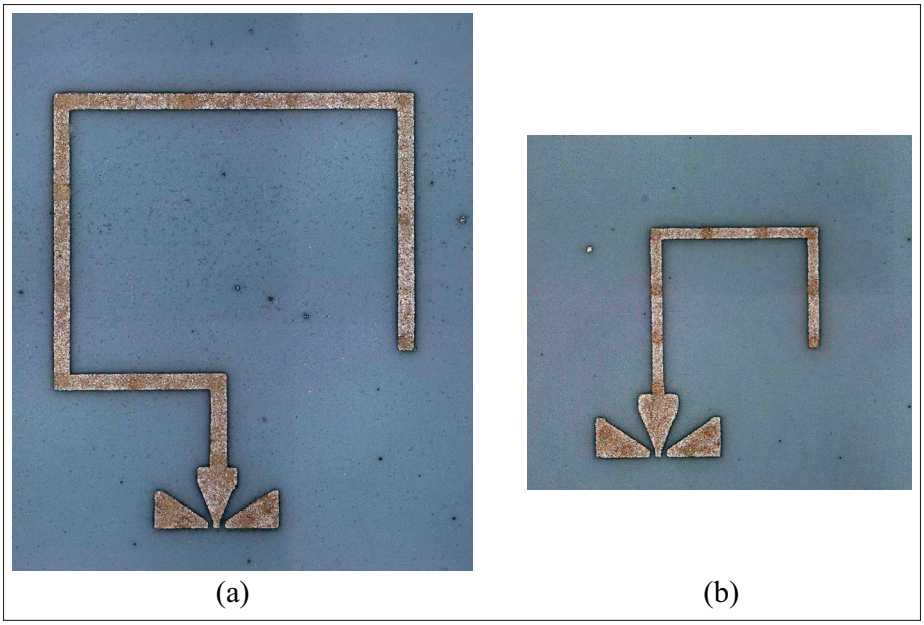

Figure 1.5 The photograph of fabricated suspended inductors (a) 5nH, (b) 2.5 nH

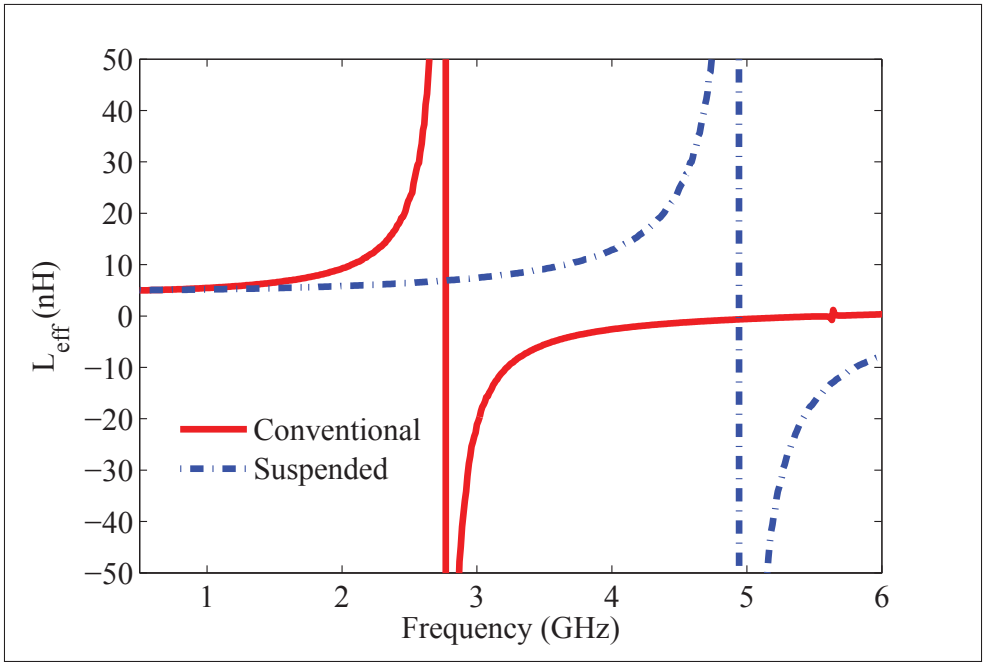

Figure 1.6 The measured effective inductance of two 5 nH inductors, one suspended inductor and the other one a conventional inductor

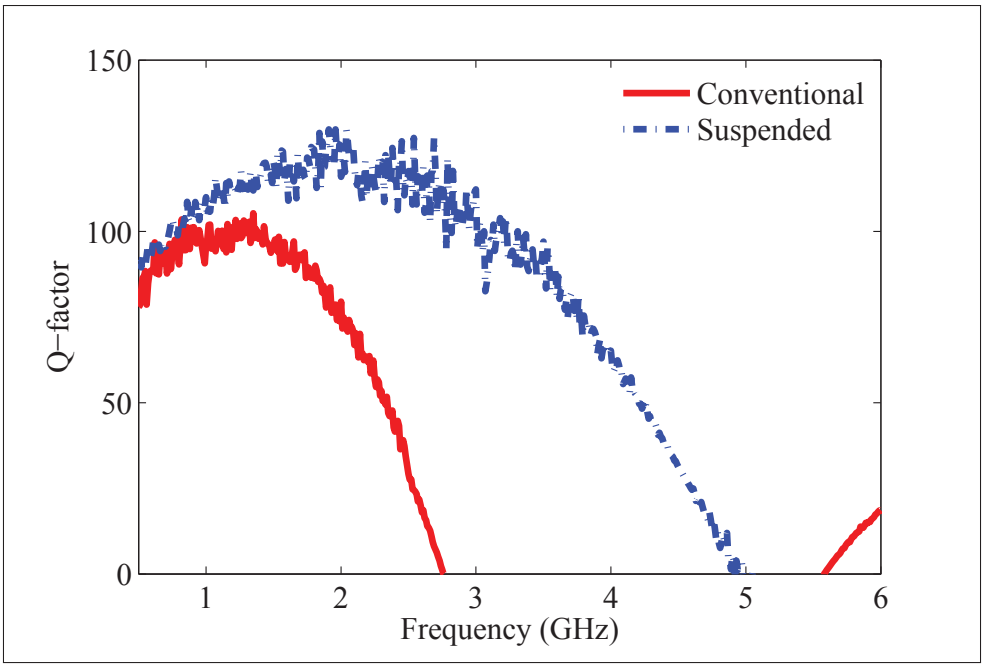

Figure 1.7 The measured Q-factor of two 5 nH inductors, one suspended inductor and the other one a conventional inductor

SRF of at least 10% for similar inductance values. Furthermore, the suspended inductors show better performance despite having thinner substrate.

Table 1.1 Comparison between performance of presented inductor and literature

Ref.	**Inductance**	**Thickness**	**Qmax**	**SRF**
This work	2.5 nH	448 μm	134	10 GHz
This work	5 nH	448 μm	125	5.05 GHz
Ref. (Aliouane *et al.*, 2011)	5 nH	896 μm	65	2.5 GHz
Ref. (Sutono *et al.*, 2001)	5.4 nH	914 μm	60	4 GHz
Ref. (Sutono *et al.*, 2001)	2.5 nH	548 μm	70	4.5 GHz
Ref. (Sutono *et al.*, 2001)	1.2 nH	548 μm	100	7.2 GHz
Ref. (Sutono *et al.*, 1999a)	5 nH	640 μm	81	4.48 GHz
Ref. (Eun *et al.*, 2004)	2.63 nH	570 μm	51	9.1 GHz

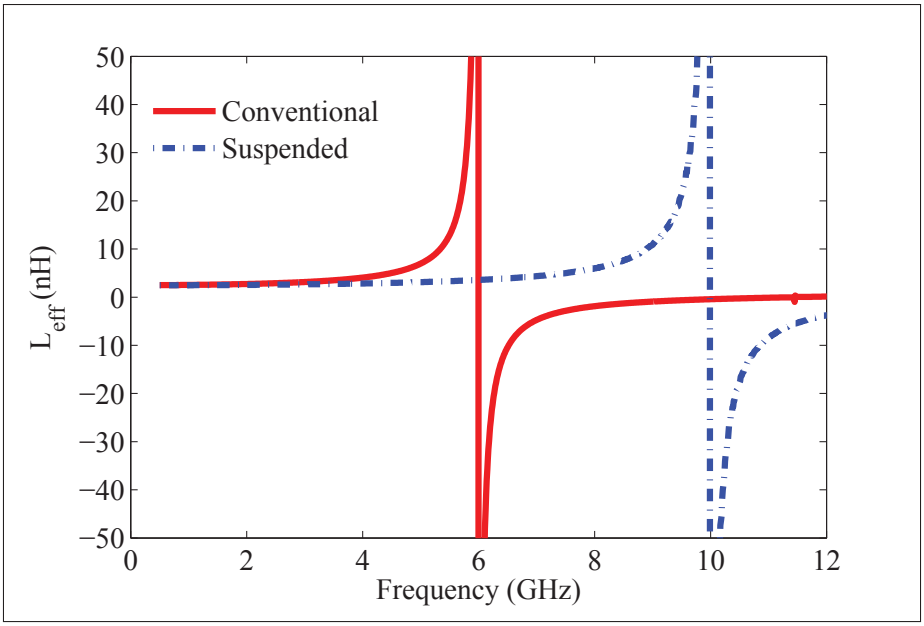

Figure 1.8 The measured effective inductance of two 2.5 nH inductors, one suspended inductor and the other one a conventional inductor

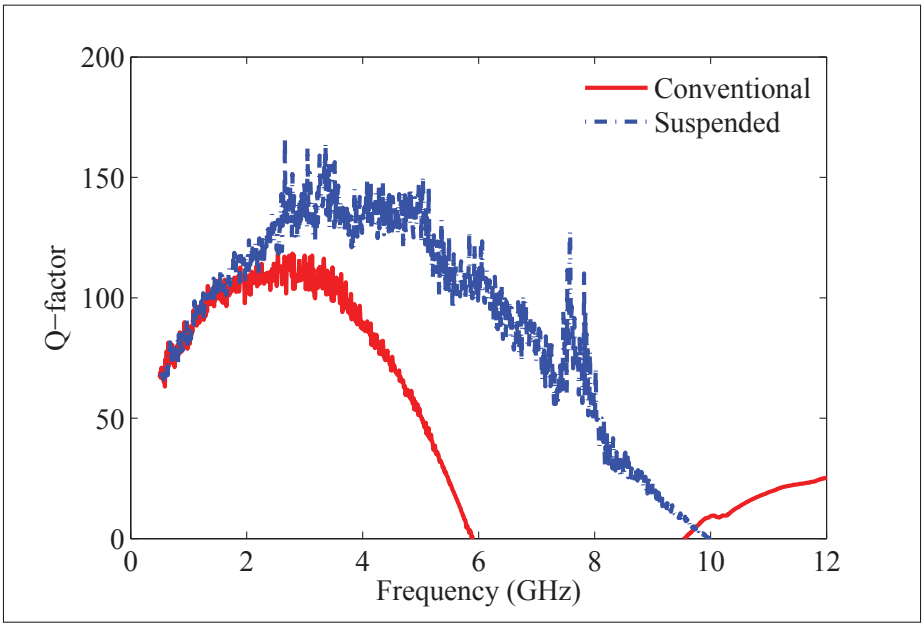

Figure 1.9 The measured Q-factor of two 2.5 nH inductors, one suspended inductor and the other one a conventional inductor

To further validate the performance of the proposed solution for capacitors, an air-filled cavity is added between the capacitor's metallic plates with the top one being suspended as shown in Fig. 1.10. This reduces considerably the dielectric loss and therefore increases Q. Furthermore, an array of vias is used to decrease the series inductance and resistance. These two solutions ultimately provide the highest possible SRF and Q for a desired capacitance with given materials and substrate thickness.

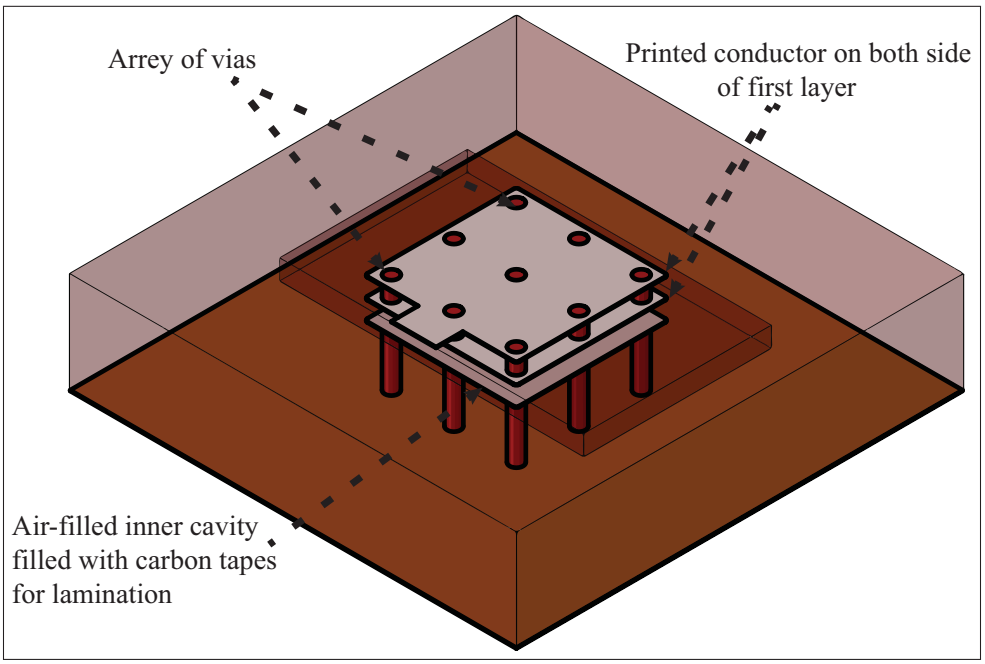

Figure 1.10 Geometry of the designed capacitor with suspended conductors and inner air-cavity

Two 1-pF capacitors, one with a conventional structure and another with suspended plate, are designed using Dupont 951 green tape with permittivity of 7.8 and loss tangent of 0.006. Another two 0.5-pF capacitors, one conventional and one with suspended plate, are designed using Dupont 9K7 green tape with permittivity of 7.1 and loss tangent of 0.001. Fig. 1.11 and Fig. 1.14 show 3D field simulated effective capacitance and Q of all capacitor versions. As can be seen from these plots, the SRF and Q are both improved by adding the air-cavity. However, one notices that at higher frequencies the conventional capacitor structure has slightly higher Q

than the proposed one. This is mainly due to the slightly higher radiation loss of the air-filled capacitor at higher frequencies.

It should be noted that, the designed capacitors have not been measured directly due to difficulties in measuring such high Q components. Indirect measurements can be obtained by integrating the capacitor in a filter as will be shown in the next section. Still, the use of 3D electromagnetic field simulation for such structures is very well established and provides excellent accuracy with very good agreement with measurements when feasible.

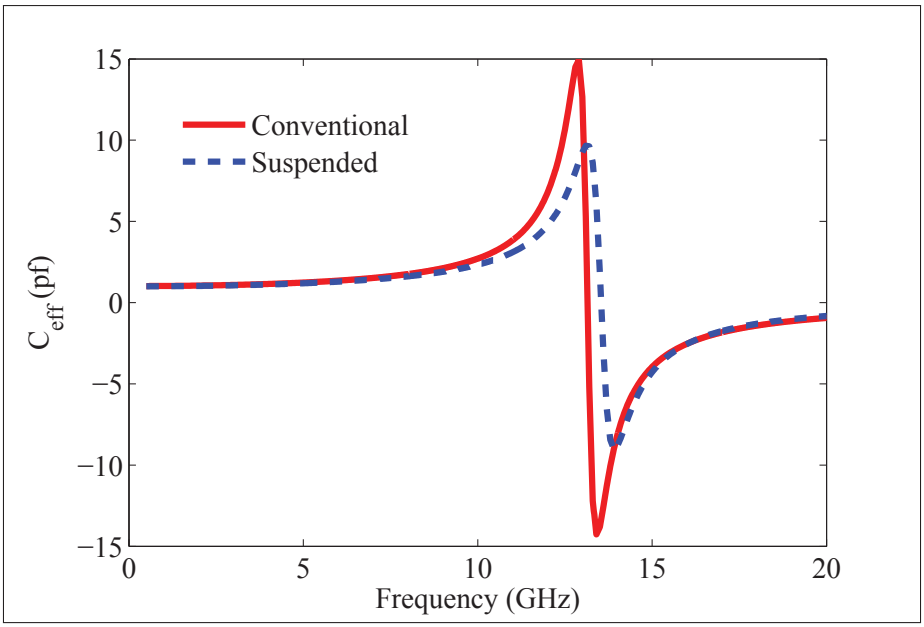

Figure 1.11 Comparison between effective capacity of two 1 pf capacitors with and without air-filled cavity in Dupont 951 ceramic

Table 1.2 present a comparison in performance between the proposed capacitor structure and those in the literature. As can be seen from this table, the proposed capacitor provides significantly higher Q and higher SRF even for higher loss substrates.

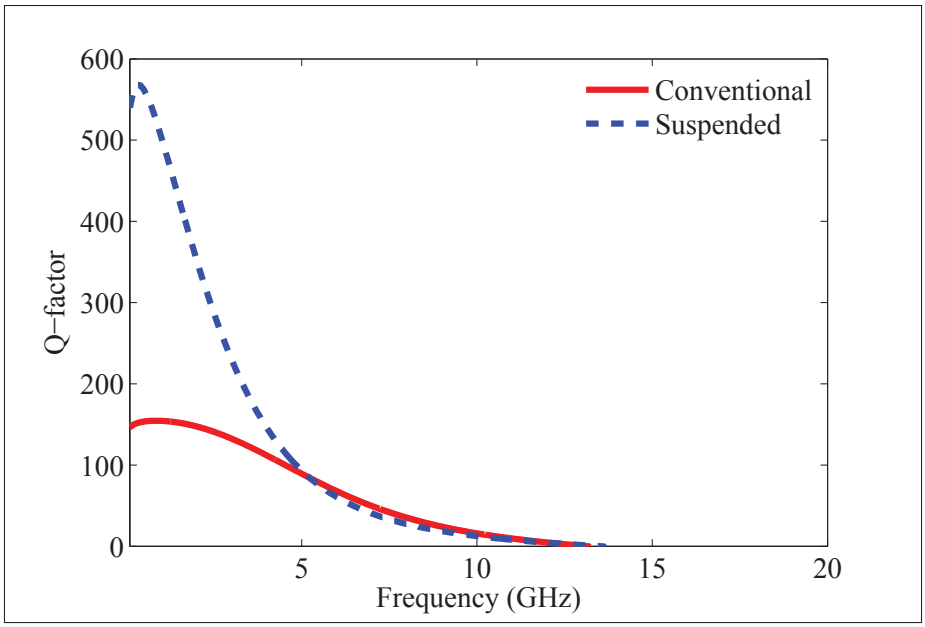

Figure 1.12 Comparison between Q-factor of two 1 pf capacitors with and without air-filled cavity in Dupont 951 ceramic

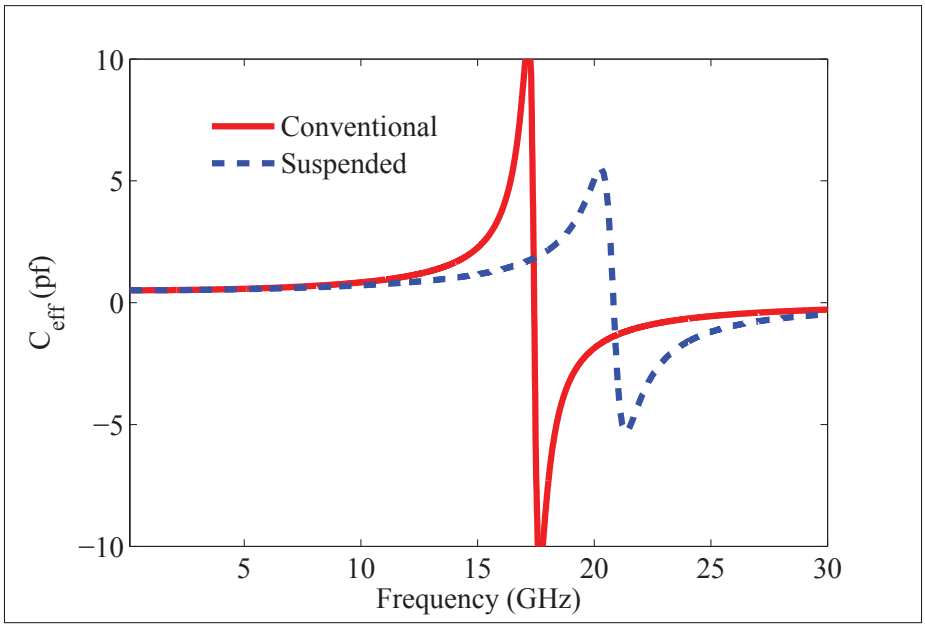

Figure 1.13 Comparison between effective capacity of two 0.5 pf capacitors with and without air-filled cavity in Dupont 9k7 ceramic

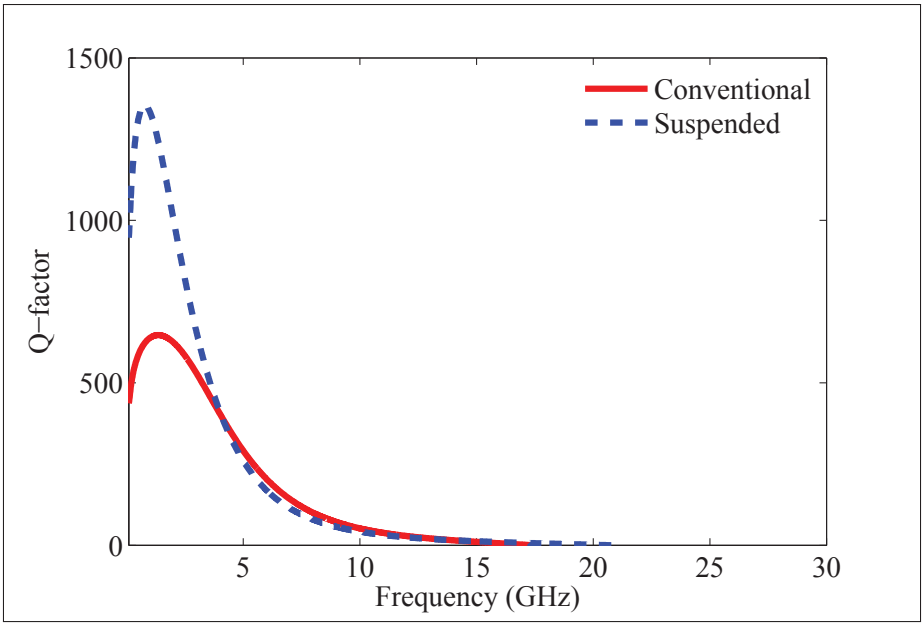

Figure 1.14 Comparison between Q-factor of two 0.5 pf capacitors with and without air-filled cavity in Dupont 9k7 ceramic

Table 1.2 Comparison between performance of presented capacitor and Literature

Ref.	**C (pF)**	**Thickness (μm)**	**tanδ**	**Qmax**	**SRF (GHz)**
This work	1	796	0.0060	567	13.5
This work	0.5	784	0.0010	1354	20.8
Ref. (Brzezina *et al.*, 2009)	0.95	800	0.0020	245	–
Ref. (Sutono *et al.*, 2001)	1.4	–	0.0015	90	6.8
Ref. (Brzezina & Roy, 2014)	1.7	720	0.0020	290	–

1.3 Ku-band lumped element filter

The fact that the proposed suspended lumped elements can achieve high Q with high SRF enables us to consider designing lumped element circuits at much higher frequencies. These circuits will operate under the lowest SRF frequency of any of its components. To illustrate this, we proposed the design of a 2-pole bandpass lumped element filter at Ku band.

Fig. 1.15 depicts the circuit model of a direct capacitive coupled band-pass filter which we select to realize here. The procedure of finding the components' value for this type of filter is already well formulated in the literature and it can be found in (Cohn, 1957). This procedure has a degree of freedom to select the parallel inductor for which we choose a 1 nH inductor to have practical values for other components in the circuit. The desired filter's parameters are summarized in Table 1.3. To design a filter with these parameters, first, we simulate each of capacitors and the inductor individually and then join them together to simulate the entire circuit, as shown in Fig. 1.16. Each component is realized using the techniques described in the previous sections to maximize the SRF and Q. For realizing small series capacitors, two printed plates are placed edge to edge and an air-cavity underneath to reduce the parasitic capacitor to the ground. Furthermore, the designed filter has been optimized to compensate the impact of interconnections between components.

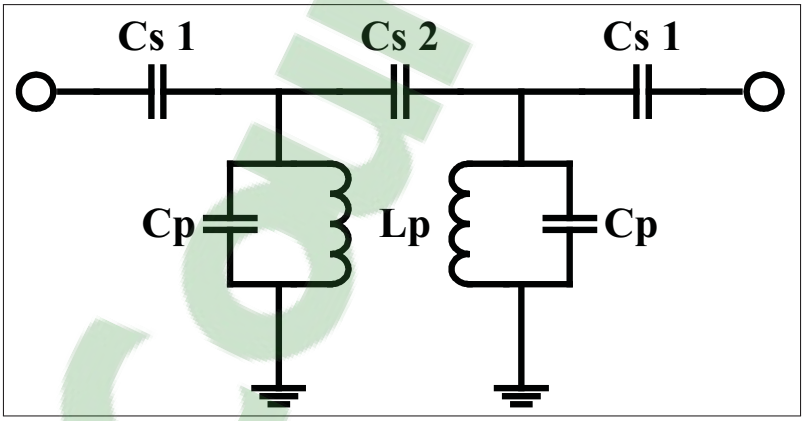

Figure 1.15 Circuit model of q two pole direct capacitive coupled band-pass filter

The total size of this filter is about 2.51 mm by 4.14 mm which is quite small compared to the other filters fabricated using LTCC ceramics at this band. The optimized pass-band lumped element filter has been fabricated using discussed procedure and successfully measured. A photograph of fabricated KU-band filter is shown in Fig. 1.17. The simulated and measured S-parameters of this filter are plotted in Fig. 1.18 and they are in a good agreement. The measured results show that the fabricated filter has an insertion loss of 2 dB and a return loss of

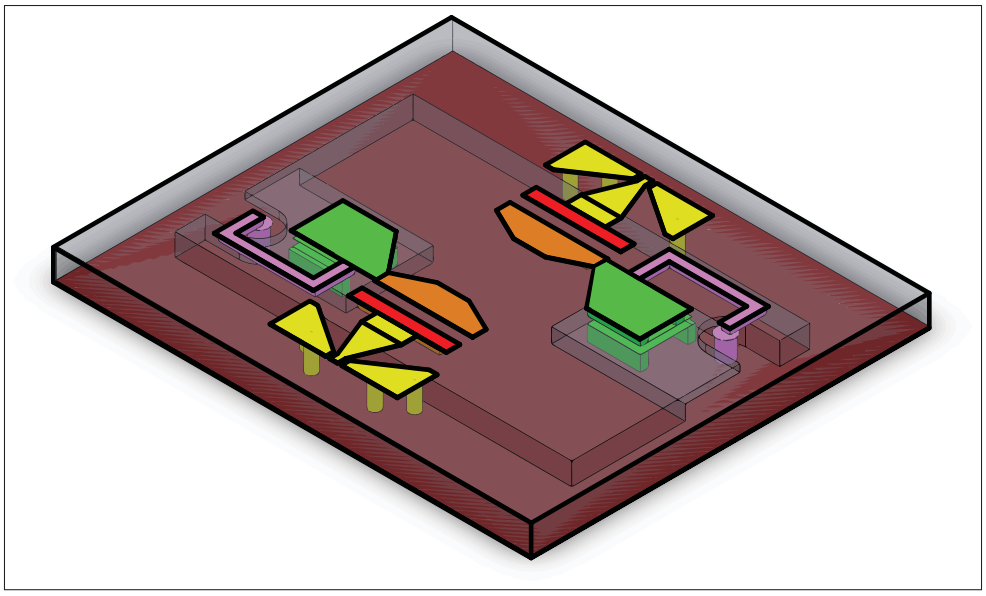

Figure 1.16 The geometry of simulated model of the designed band-pass filter

Table 1.3 Ku-band filter parameters

Parameter.	**Value**	**Parameter**	**Value**
f_0	$11.95\,GHz$	BW	$500\,MHz$
Order	2	Ripple	0.05
Permittivity	5.7	Loss tangent	0.001
C_s1	$55.1\,fF$	C_s2	$12.2\,fF$
C_p	$112.4\,fF$	L_p	$1\,nH$

-18.8 dB at 12 GHz. Furthermore, the designed filter provides a very good out of band rejection which is better than -20 dB up to 30 GHz.

1.4 Conclusion

A new metal configuration has been proposed along with using inner air-cavity to design suspended LTCC integrated lumped elements. The proposed suspended components show significantly better performance in terms of Q and SRF compared to the conventional designs.

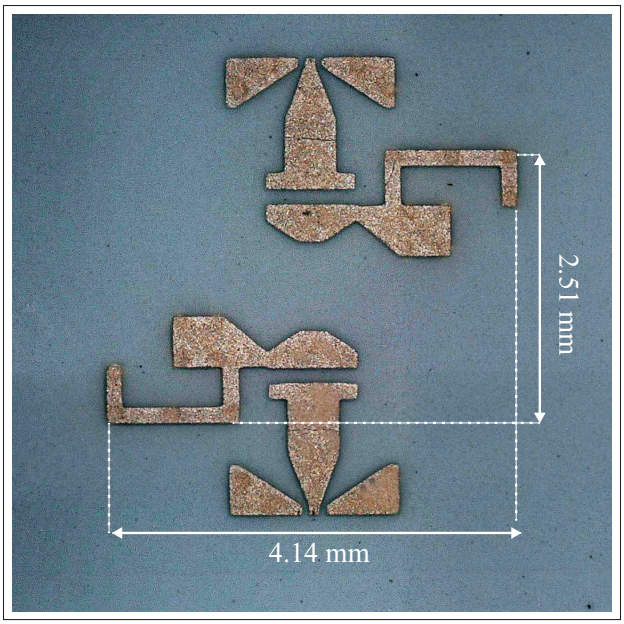

Figure 1.17 A photograph of fabricated filter

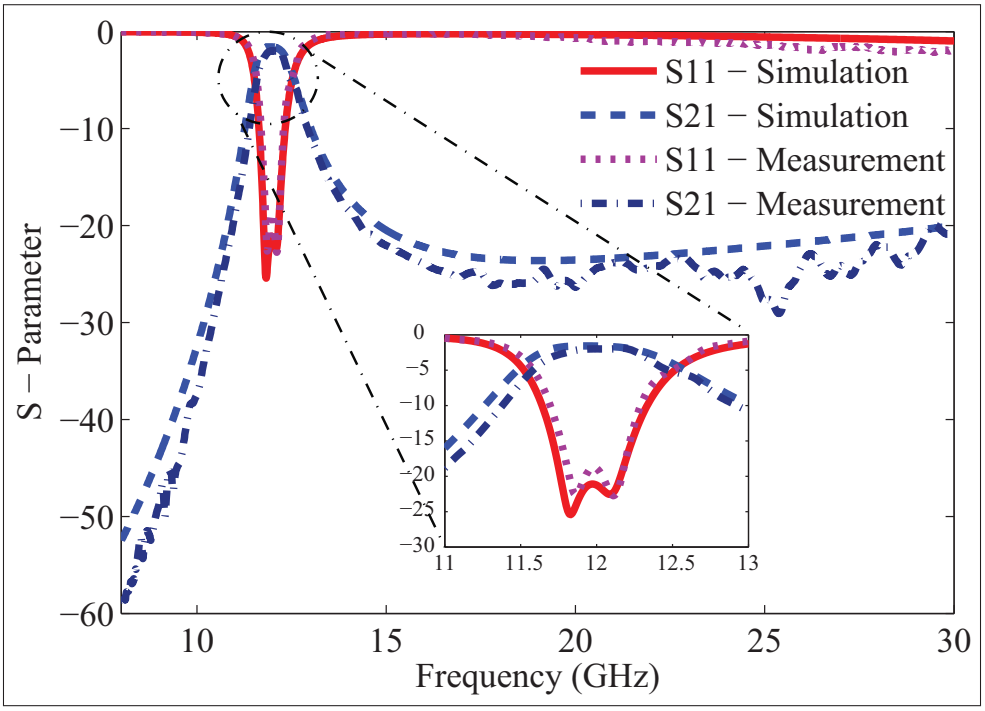

Figure 1.18 The measurement results for KU-band pass-band filter

Furthermore, using these enhanced SRF elements, we have design a lumped element filter at

KU-band for the first time. This filter and several inductors have been fabricated and successfully tested with excellent low loss performance.

CHAPTER 2

EMPTY LTCC INTEGRATED WAVEGUIDE WITH COMPACT TRANSITIONS FOR ULTRA-LOW LOSS MILLIMETER-WAVE APPLICATIONS

Aria Isapour [1], Ammar Kouki [1]

[1] Département de Génie Électrique, École de Technologie Superieure ,
1100 Notre-Dame Ouest, Montréal, Québec, Canada H3C 1K3

Manuscript published in IEEE Microwave and Wireless Components Letters in October 2017.

Abstract

An Empty LTCC (Low Temperature Cofired Ceramics) Integrated Waveguide (E-LIW) for the 57-64 GHz band is proposed. In addition to being air-filled, this SIW-like structure uses long rectangular side-wall vias to reduce conductor and radiation losses. In simulation, the proposed structure shows an insertion loss of 0.084 dB/cm at 60 GHz compared to 0.325 dB/cm, when the same structure is dielectric filled, and 0.48 dB/cm when it is dielectric filled but with conventional cylindrical vias. A very compact transition between E-LIW and CPW is also proposed. A back-to-back configuration including the proposed transition and E-LIW has been fabricated. Measurement results show a maximum total insertion loss of 0.5 ± 0.2dB with better than 20dB return loss for the entire structure and over the entire frequency band of interest. These results are in good agreement with those obtained by 3D field simulation.

Introduction

Low Temperature Cofired Ceramics (LTCC) technology offers the possibility of having an almost arbitrary number of layers using very low loss dielectrics and highly conductive metals such as silver and gold. It is a promising technology for the realization of 3D integrated and miniaturized passive circuits with mature fabrication processes. The advantages and capabilities of LTCC in the design of high performance, cost effective planar and 3D passive components in microwave and millimeter-wave frequencies are well documented in large body of

literature, see for example (Wolff (2007a); Lee *et al.* (2005); Imhof & Schless (2007)). Furthermore, LTCC covers a very wide range of applications such as packaging, industrial sensors, biomedical applications, etc. It also has well established fabrication processes that ensure, among other things, excellent alignment of multiple layers.

It is well known that conventional printed guiding structures, e.g., microstrip, stripline, CPW, etc., suffer from high loss at high frequencies. Substrate Integrated Waveguide (SIW) has been proposed (Deslandes & Wu (2001a)) as alternative to take advantage of the lower loss of conventional rectangular waveguides while maintaining printed circuit integration capabilities. This technique is well-suited for implementation in LTCC technology owing to this latter's multi-layer nature (Huang & Wu (2003)). However, whether using conventional PCB material or LTCC ceramics, SIW structures still suffer from dielectric loss in addition to the unavoidable conductor loss. In order to reduce or eliminate the dielectric loss, the concept of an air-filled SIW was introduced in (Ranjkesh & Shahabadi (2006)). This work focused on basic computational analysis with no consideration for practical implementation issues nor transitions to conventional planar transmission lines. An air-filled waveguide transmission line in LTCC for G-band frequencies was introduced in (Henry *et al.* (2008)). Unexpectedly, the fabricated line of this work results a transmission loss close to other planar line. Furthermore, no transition to other structures was reported in (Henry *et al.* (2008)). In (Belenguer *et al.* (2014)), an empty SIW with transition to microstrip using a milling process was proposed and used to design and test filters up to 20 GHz with demonstrated loss reduction. However, the proposed transition restricts the SIW height, which should be higher to reduce loss, to be the same as the microstrip substrate thickness, which should be lower to be usable at higher frequencies. In parallel, a similar air-filled SIW design with a two-step transition to CPW using a 'sandwiching' of multilayer PCBs was presented in (Parment *et al.* (2015b)) with simulation up to 60 GHz but measurements to 40 GHz. This design resulted in long transitions, leading to increased size and insertion loss. In both (Belenguer *et al.* (2014)) and (Parment *et al.* (2015b)), circuit fabrication is sensitive to alignment, which is more critical at mm-waves.

In this paper, a new Empty LTCC Integrated Waveguide (E-LIW) is presented combining the advantages of SIW and LTCC while virtually eliminating dielectric loss. A new very compact, two-step transition from E-LIW to CPW with vertical probe excitation is proposed.

2.1 Empty LTCC integrated waveguide structure

The structure of the E-LIW is depicted in Fig. 2.1. The bottom layer consists of a printed metal on top of one LTCC sheet. Several LTCC sheets with rows of rectangular vias, to form the side walls of the LIW, and air cavities, to form the inside of the LIW, are then stacked on top of the bottom layer. A specially designed metallized LTCC sheet, consists of rows of vias and a printed silver conductor, forms top layer that completes the structure. This special design is needed to respect the limitation of the fabrication process of printing on one side only. Via spacing and size were determined to reduce loss while still respecting the fabrication design rules of our in-house process (Gravel (2016)).

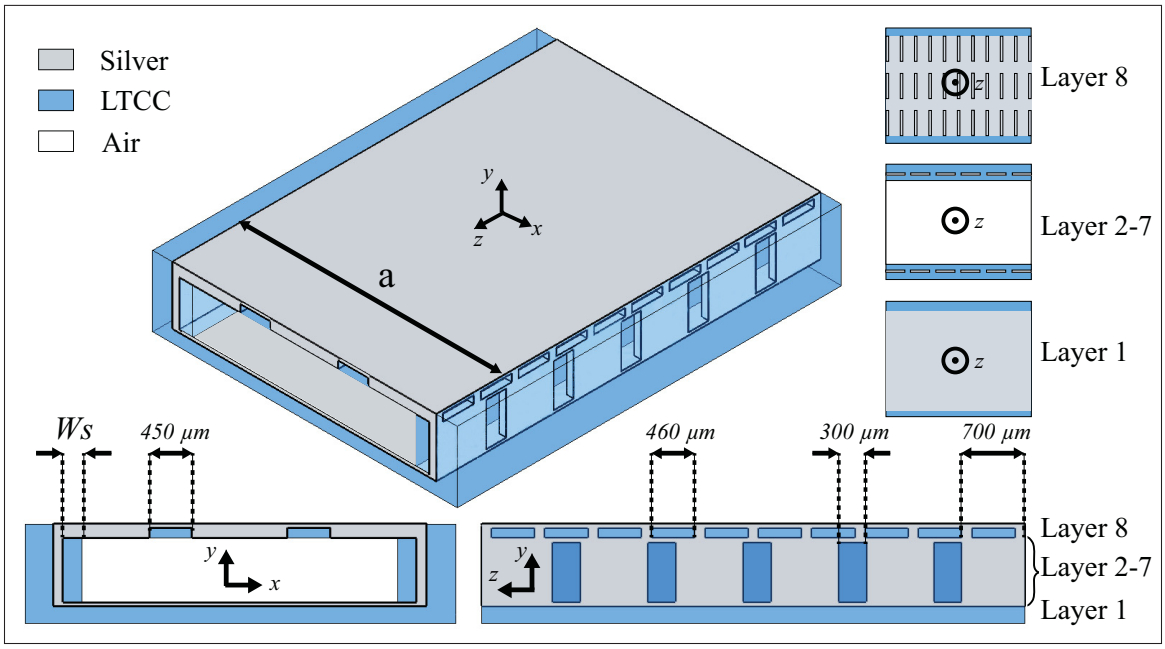

Figure 2.1 Proposed empty LTCC-integrated waveguide structure

To compare the transmission loss performance of the E-LIW and the conventional LIW we focus on the 60 GHz unlicensed band and start by designing guiding structures that will operate between 57 and 64 GHz. A cutoff frequency of 35 GHz is selected for both structures such that the operation frequencies are located within the region of minimal loss and dispersion. For a completely air-filled waveguide with fully metallized side walls, the cutoff frequency is given in terms of the speed of light, c, and the width of the waveguide, a, by $f_{c10} = c/2a$, which leads to a waveguide width of 4.285 mm for a cutoff of 35 GHz. For our proposed LIW, two dielectric slabs on either side of the guide are required in order to allow for proper filling of the side vias, see Fig. 2.1, as well as for maintaining the mechanical integrity of the structure during the fabrication process. The dielectric slabs lead to a partially filled waveguide and therefore they will impact dielectric loss and the cutoff frequencies. In fact, the cutoff frequency of the dominant TE10 mode, assuming continuous side-walls, can be found from (Parment *et al.* (2015b)):

$$tan\left(\frac{2\pi\sqrt{\varepsilon_r}f_{c10}w_s}{c}\right) = \sqrt{\varepsilon_r}cotan\left(\frac{\pi f_{c10}(a-2w_s)}{c}\right) \tag{2.1}$$

where ε_r is the dielectric constant of the LTCC sheets and w_s is the width of the slabs. Using slabs of $200\mu m$ width each with a ε_r = 7.1 and a = 4.285 mm, the cutoff frequency is found to be 34.85 GHz, which is little changed compared the completely air-filled waveguide. To take into account the use of vias for sidewalls one can use the closed-form model for predicting the cutoff frequency (Che *et al.* (2008a)) for cylindrical vias or 3D EM field simulation for general shaped vias. Here we opt for the latter option in order to compute the impact side vias on the cut-off frequency as well as on the dielectric loss. For our desired cut-off frequency of 35 GHz, these calculation lead to a width of 4.2 mm, including the effect of side dielectric slabs of $200\mu m$ each.

Next, we assess the performance of the proposed E-LIW by comparing the attenuation constant per cm (α_T) for 5 structures using the same metals and dielectrics and having the same cutoff frequency of 35 GHz: (i) an air-filled conventional waveguide, (ii) a dielectric filled conven-

tional waveguide, (iii) a LIW with cylindrical vias, (iv) a LIW with rectangular vias and (v) the proposed E-LIW. For (i) and (ii) theoretical expressions for α_T are used. For the remaining three structures, α_T is computed from the S-parameters obtained by 3D field simulation using Degerstrom *et al.* (2008):

$$\alpha_T = -8.68 \frac{ln\left(|S_{21}|^2\right) - ln\left(1-|S_{11}|^2\right)}{2l} \quad (dB/cm) \tag{2.2}$$

where l is the length of the waveguide structure in cm. The results of these calculations, considering the effect of surface roughness, are shown in Fig. 2.2 where the insertion losses for these lines at 60 GHz are 0.058, 0.305, 0.483, 0.325, and 0.084 dB/cm respectively. It can be seen that the proposed E-LIW outperforms all other structures except for the fully metallized air-filled conventional waveguide. It should also be noted that using rectangular vias, which is relatively easy to do in LTCC, does lead to reduced losses compared to using cylindrical ones.

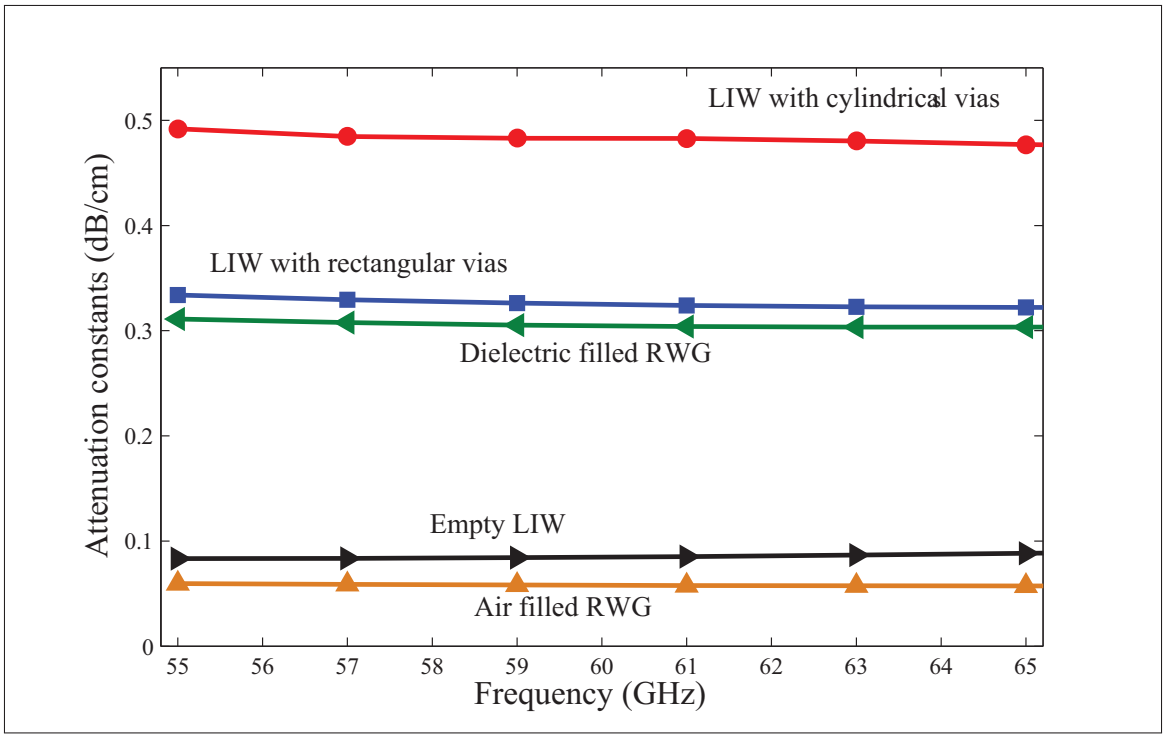

Figure 2.2 Theoretical and simulated comparison between E-LIW and LIW

2.2 Compact transition to E-LIW

A transition from E-LIW to CPW is desired in order to be able to measure the structures and, ultimately, to integrate various other components on its surface. As stated, the size of such transitions can be critical from loss standpoint. Here we propose a new compact two-step transition as depicted in Fig. 2.3. Fig. 2.3a shows the transition from E-LIW to LIW while Figs. 2.3b and 2.3c show the probe-type transition from LIW to CPW.

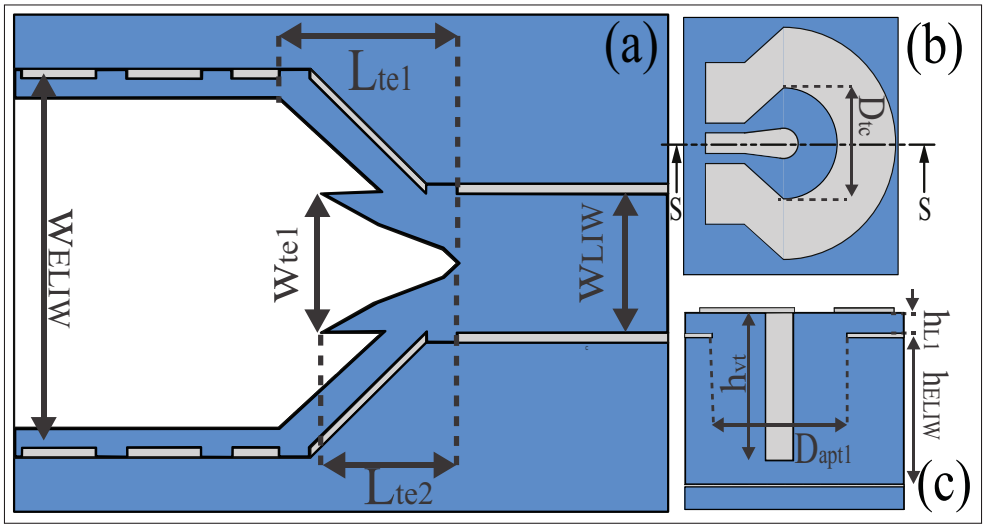

Figure 2.3 (a) Transition from E-LIW to LIW. (b) Transition from LIW to CPW, top view and (c) side view at section cut s-s.

To design the transition from E-LIW to LIW two options were considered: either tapering the dielectric from the LIW to E-LIW as in (Belenguer *et al.* (2014)) or, inversely, tapering the air from the E-LIW inside the LIW as in (Parment *et al.* (2015b)). The transition in (Belenguer *et al.* (2014)) will have shorter length but will be difficult to match for high dielectric constant contrast. On the other hand, the transition in (Parment *et al.* (2015b)) results in longer dimensions but easier matching. Furthermore, given that the electric field of the TE_10 mode is strongest in the middle of the waveguide, choosing the second transition shape would reduce the amount of dielectric to which electric field is exposed, which in turn would lead to lower dielectric loss. For these reasons we chose the second transition shape.

To reduce the size of this transition, we again exploit the fact that the electric field is concentrated in the region with higher permittivity to introduce compensating dielectric wedges as shown in Fig. 2.3a. This results in a compact 1.4 mm transition with reduced insertion loss and good matching. The LIW to CPW transition is realized with a tapered 50 Ω CPW line that connects to a one-layer vertical half-coaxial line, with the central conductor becoming a vertical probe inside the LIW. The size of this transition is 1.1 mm. All transitions have been optimized with ANSYS HFSS and the results are shown in Fig. 2.4. It should be noted that the simulation time for each frequency on a Core-i7 machine is about 200 seconds.

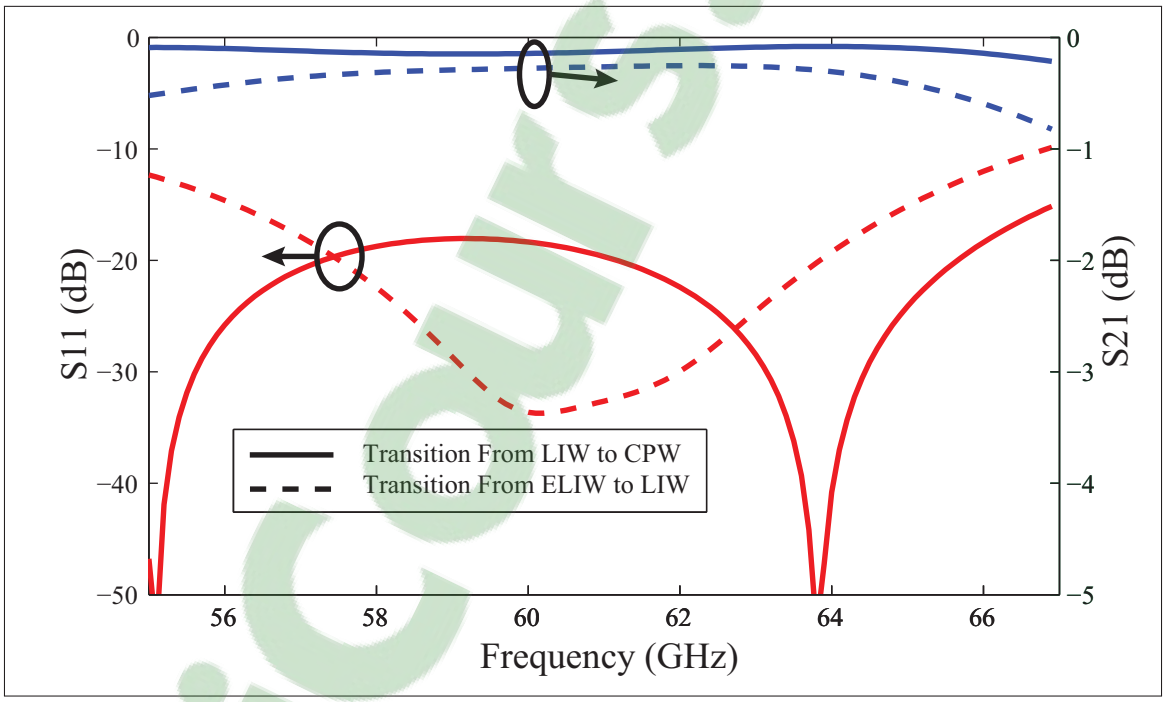

Figure 2.4 Simulation results for back to back transitions using HFSS

2.3 Fabrication and measurement results

A 2.3 mm section of an E-LIW with transitions at both ends as illustrated in Fig. 2.3 was fabricated using eight 112 μm thick layers of Dupont's 9k7 green tape having a permittivity

of 7.1 and a dielectric loss tangent of 0.001. Vias were filled and metals printed using silver. Carbon tapes were used to fill the cavities in order to maintain their structural integrity during the stacking and laminating steps. These are fugitive tapes that sublimate at $600°C$ during sintering.

Fig. 2.5 shows a photograph of the fabricated E-LIW structure with its end to end transitions. This structure was measured using a probe station and a PNA-X network analyzer. Fig. 6 shows the measured and simulated results which include both transitions. A better than 20 dB return loss has been measured with a total back to back insertion loss of 0.5 ± 0.2 dB from $57 - 66$ GHz band. Based on Fig. 2.4 This insertion is entirely attributable to the transitions with the E-LIW section having negligible loss. In fact, HFSS simulation of the 2.3 mm section of E-LIW gives an insertion loss of 0.019 dB, which is consistent with the results of Fig. 2.2 and even less than the uncertainty of network analyzer (keysight,2017).

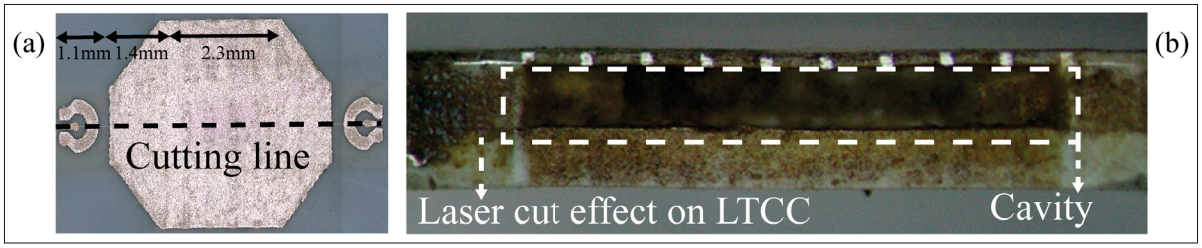

Figure 2.5 Photograph of fabricated E-LIW (a) completed structure (b) cut in the middle (at the cutting line) by laser in order to show the inner air cavity

Table 2.1 presents a comparison of transition performance and size based on measured data for this work, the one in (Parment *et al.* (2015b)) and the simulated one in (Belenguer *et al.* (2014)). It is worth noting that our measured loss includes both two-step transitions, from E-LIW to LIW and LIW to CPW, while those in (Belenguer *et al.* (2014)) only include the first transition. Despite this, and the fact that our work is at a higher frequency, we still obtained better return and insertion losses. Furthermore, we obtained much electrically smaller transition size. This improvement is due to the short length of transition from E-LIW to LIW and the probe-type excitation which makes it possible to have very thick LIW, which also reduces the transmission

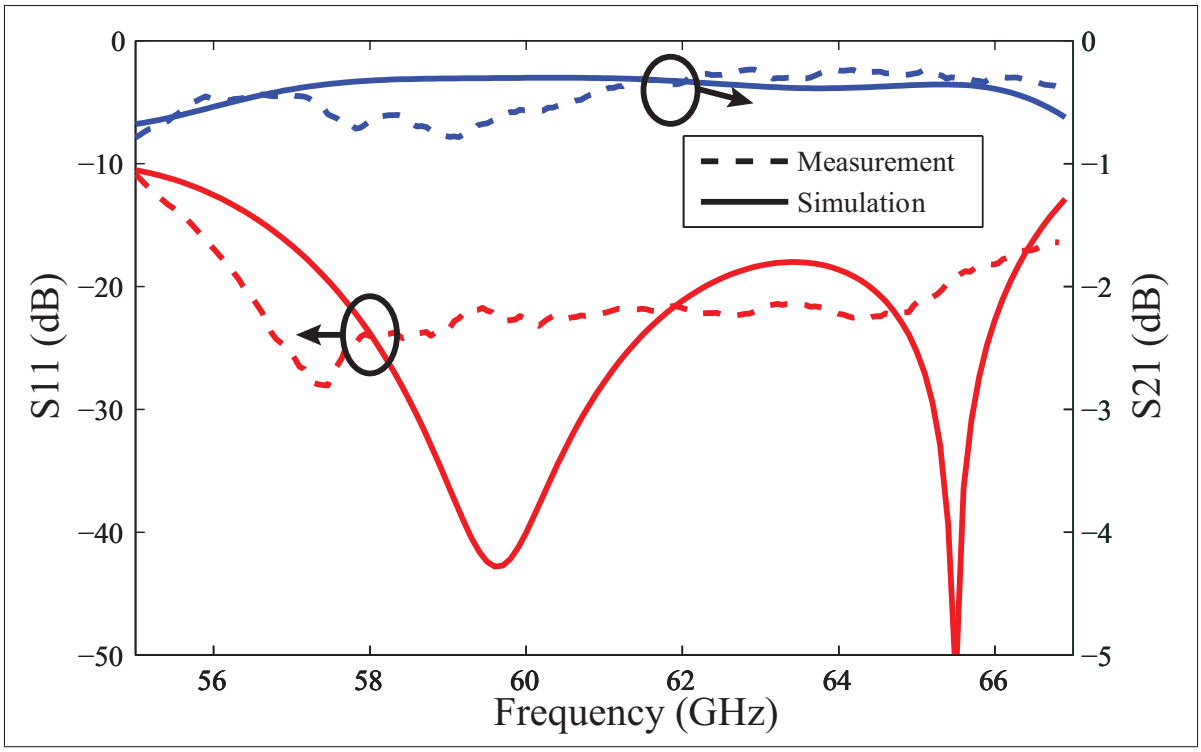

Figure 2.6 Measured and simulated results for end to end transitions

loss. The relative bandwidth obtained here is narrower compared to (Belenguer *et al.* (2014); Parment *et al.* (2015b)) due to (i) the large difference between the permittivities of LTCC and air in the LIW to E-LIW transition and (ii) the presence of a probe-type CPW to LIW transition, which is required for thick substrates and has intrinsically limited bandwidth.

2.4 Conclusion

Eliminating the dielectric inside substrate integrated waveguides and using rectangular vias in LTCC have been proposed to design ultra-low loss guiding structures. Compact transitions from empty LTCC integrated waveguide (E-LIW) to filled LTCC integrated waveguide (LIW) and from LIW to CPW have also been proposed. An end-to-end guiding structure with transitions, for the unlicensed 60 GHz band, has been successfully tested with excellent low loss performance.

Table 2.1 Comparison of the transitions

Ref.	**f (GHz)**	**BW (%)**	**IL (dB/Transition)**	**RL (dB)**	**SIW to ESIW (λ)**	**SIW to CPW (λ)**
(Belenguer *et al.* (2014)) Simulation	$18-26$	36.3	0.25	22	0.55	-
(Parment *et al.* (2015b))	$27-40$	38.8	0.3 ± 0.1	15	3.77	3.77
This work	$57-66$	14.6	0.25 ± 0.1	20	0.74	0.59

CHAPTER 3

VERTICAL LTCC INTEGRATED RECTANGULAR WAVEGUIDE, AND TRANSITIONS FOR MILLIMETER-WAVE APPLICATIONS

Aria Isapour [1], Ammar Kouki [1]

[1] Département de Génie Électrique, École de Technologie Superieure ,
1100 Notre-Dame Ouest, Montréal, Québec, Canada H3C 1K3

Manuscript accepted to IEEE Transaction on Microwave, Theory and Techniques on November 2018.

Abstract

A new vertical guiding structure in Low Temperature Co-fired Ceramics (LTCC) substrates is proposed. This Vertical LTCC Integrated Waveguide (V-LIW) allows transmitting signals and realizing components in the body of the LTCC substrate perpendicular to its surface. This vertical integration leads to considerable footprint reduction while opening the door to higher frequency coverage as well as easy implementation of E-plane structures. Discontinuities in V-LIW and transitions between the proposed V-LIW and conventional horizontal guiding structures such as coplanar waveguides, standard rectangular waveguides and substrate integrated waveguides are also introduced. Applications to the design of V-band and W-band filters, couplers and power-dividers are presented. Several prototypes are fabricated with measurement results showing good agreement with simulation data.

Introduction

The rapid progress of multi-functional hand-held devices in a context of growing numbers of wireless applications and cloud-based services leads to a daily increase in demand for more bandwidth. The crowded microwave radio spectrum has limited bandwidth for today's multitude of wireless services and cannot provide a long-term solution for the increasing bandwidth

demands. It is, therefore, an unavoidable necessity to migrate to millimeter-wave frequencies where we can take advantage of both large available bandwidth and less crowded channels.

In millimeter-wave frequencies, the loss of conventional planar guiding structures e.g., microstrip, CPW, and stripline are significant. On the other hand, air-filled metallic waveguides show better loss performance but at the expense of bulkiness and integration complexity. Substrate Integrated Waveguides (SIW) (Deslandes & Wu (2001a)) offer a viable alternative through printed guiding structures to combine low loss performance of conventional rectangular waveguides with integration convenience of printed planar transmission lines. Since (Deslandes & Wu (2001a)), in a large body of literature, researchers have explored SIW's characteristics such as design considerations (Cassivi *et al.* (2002)), loss mechanism (Deslandes & Wu (2006)), and transitions (Isapour & Kouki (2017)), as well as the analytical (Che *et al.* (2008a)) and numerical (Shahvirdi & Banai (2010)) modeling of SIW. Moreover, substrate integrated waveguides are widely used in the realization of a wide variety millimeter-wave circuits, e.g., filters (Chen & Wu (2008a)), phase shifters (Cheng *et al.* (2010)), antennas (Cheng *et al.* (2012)), etc.

Despite the interesting features of SIW, it still suffers from certain limitations and drawbacks. One of the most important ones is the implementation difficulty at very high frequencies. It is well-known that the realization of SIW circuits at frequencies of higher than 150 GHz with current ceramic fabrication technology is challenging (Wang *et al.* (2016)) and it becomes almost impractical at terahertz frequencies. This is due to the fact that the SIW relies on a set of vias to form waveguide side walls and also to perturb the fields inside the waveguide in applications like iris filters. The spacing between the adjacent in the same layer at higher frequencies would be too small to be fabricated with a regular multilayer ceramic process. Furthermore, SIW circuits, compared to their counterparts, usually use more footprints to realize components. This leads to a significant reduction of space for potential active circuits which can only be mounted on the surface. Moreover, for waveguide applications where E-Plane structures are needed, conventional SIW cannot be utilized in a standard fabrication process. In these

applications, metallic rectangular waveguides are still widely used as an H-plane to E-plane transitions (Zhang & Lu (2008)).

In recent years, three-dimensional (3D) SIW structures were introduced to realize E-plane components (Khatib *et al.* (2012)), to make the millimeter-wave systems more compact (Doghri *et al.* (2015, 2012a, 2013)) and reduce the footprint size (Doghri *et al.* (2012b)). However, all the reported works in (Khatib *et al.* (2012); Doghri *et al.* (2015, 2012a,b, 2013)) do so by a Lego-like assembling of one PCB substrate perpendicular to another substrate, which is not a standard PCB process and therefore structures are subjected to lateral misalignment and gaps between pieces (Doghri *et al.* (2013, 2015)). In fact, these 3D SIWs are two conventional SIWs which are only attached together in a L-type configuration. These designs are also relatively bulky since the region between two sections of SIW is unusable.

Multi-layer fabrication technologies, including Low Temperature Co-fired Ceramic (LTCC) technology, are well-suited for implementation of SIWs (Huang *et al.* (2003)) and they can be an excellent candidate to realize the 3D SIWs as well. The well-established fabrication process of LTCC allows us to realize passive circuits by the almost arbitrary number of layers having very low loss and high permittivity dielectrics. Moreover, the relatively low sintering temperature makes it possible to utilize the high conductivity metals; gold, and silver. These all together, enable LTCC to be a superior choice in the design of high performance three-dimensional passive components from microwave frequencies (Wolff (2007a)) to optical (Heilala *et al.* (2005)), and from exclusively packaging (Kim *et al.* (2005)) to realize the entire RF module (Zhou *et al.* (2017); Lin *et al.* (2004)).

In this paper, we propose a new type of LTCC Integrated Waveguide (LIW) suitable for realizing true 3D SIW structures at mm-waves and beyond and for their eventual mass production. In particular, we will introduce Vertical LIW (V-LIW) structures and building blocks that can be fabricated using a standard LTCC process and we show how they can be used to implement various function at mm-wave frequencies. Combined with horizontal SIW-type guides when needed, complex functionality, including E-plane structures, can be implemented over limited

surface areas. The rest of the paper is organized as follow. Section II describes the vertical LTCC integrated waveguides, provides an empirical formula to find the propagation constant and cut-off frequency, and explains the loss mechanism and design consideration. Section III presents proposed transitions to standard waveguides and planar transmission lines. These transitions are the essential parts for measurement purpose as well as circuit realization. In section IV, the interesting features of V-LIW in design of millimeter-waves passive circuits through design will be demonstrated through simulation and successfully measurement of three elementary circuits: a power divider, a coupler, and two filters. Finally, conclusions are given in section V.

3.1 V-LIW structure and design considerations

At mm-wave frequencies, the wavelength becomes sufficiently small to make it possible to realize a number of distributed circuits vertically rather than horizontally. The basic element of such vertical circuits is a new guiding structures which can transfer mm-wave signals in a perpendicular direction to the surface. Fig. 3.1 illustrates how such a structure can be realized in a multi-layer printed circuit technology, particularly LTCC, and compares the proposed V-LIW structure to the conventional SIW alternative. However, in order design and build meaningful circuits and functions, a number of building blocks are required in addition to the V-LIW. The main such building blocks are illustrated in Fig. 3.2 and will be addressed in the subsequent sections of the paper.

3.1.1 V-LIW structure's basics

In the LTCC process, each layer of green tapes can have a different combination of filled vias and printed metallic lines. Thanks to the powerful laser processing, as long as the mechanical integrity of green tapes is preserved, the vias can have almost arbitrary shapes. To have a perfect vertical dielectric filled rectangular waveguide, four rectangular vias are required to form the side and the broad walls. However, this leads to the complete detachment of the dielectric between vias. Thus, in the proposed V-LIW, two rectangular vias are used as the

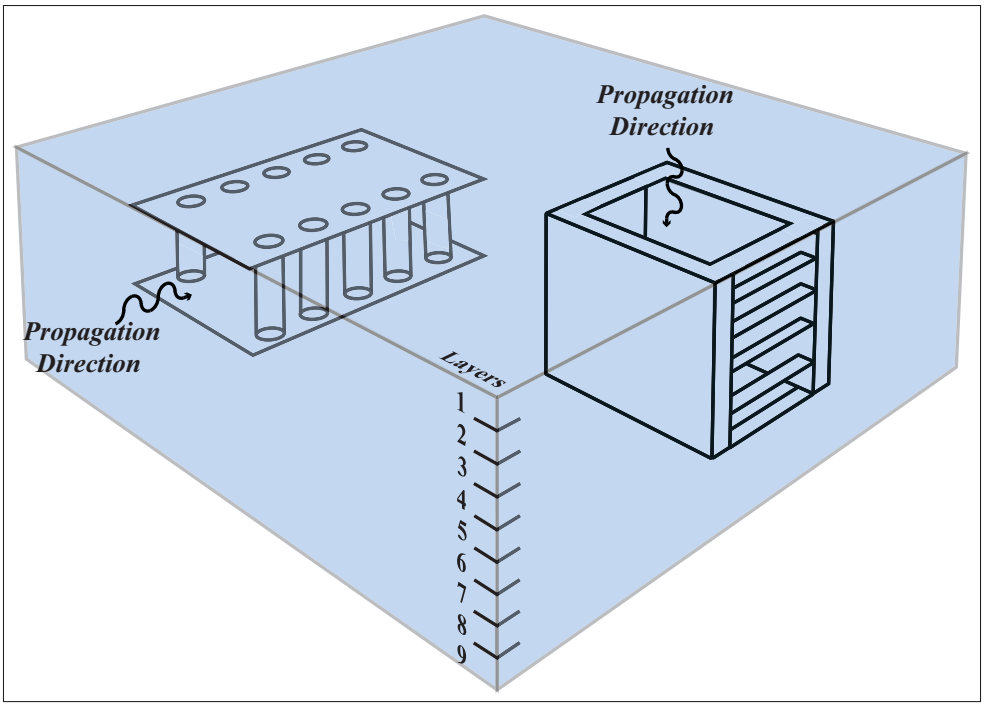

Figure 3.1 Vertical LTCC Integrated Waveguide (V-LIW) vs conventional SIW

broad walls, while the two other vias replaced with printed metallic strips. Fig. 3.3.a illustrates the geometry of each of these green tapes. As it can be seen from this figure, two rectangular vias are punched in each layer and then filled with silver paste. The metal residues leaves around each via during via filling process are cleaned using a laser process. Thereafter, the strips are printed on each layer. These filled and printed layers are then stacked precisely with four alignment points to form the proposed 3D guiding structure.

With the aid of proposed guiding structure, we can transfer signals vertically to the buried ceramic layers and also realize passive components in a perpendicular plane to the surface. The introduced vertical LIW will address all the limitations and drawbacks of conventional SIW and Lego-like 3D SIWs, mentioned earlier in introduction section. It will not only significantly reduce the footprint size of the components and save the circuit's surface for mounting active components, but also it will allow for easy implementation of E-plane structures. Moreover, the proposed Vertical LIW (V-LIW) can push the upper-frequency limit of realizing passive

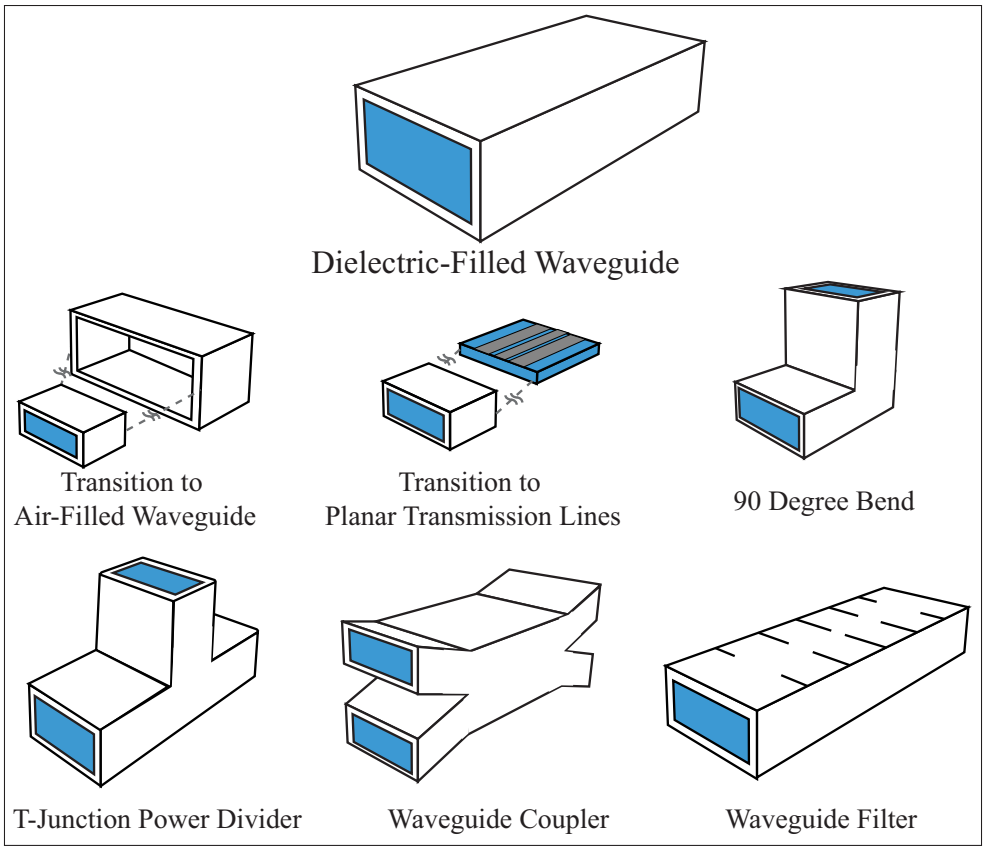

Figure 3.2 Main building blocks in a waveguide system

components with SIW. In our proposed V-LIW, printed metallic strips, are used instead of vias. These metallic strips can be as close as 18.5 μm to each other and enable V-LIW to potentially operate at much higher frequencies and eventually in terahertz frequencies.

The working mechanism of V-LIW is very similar to its antecedents, rectangular waveguide, and SIW, however utilizing the metallic strips instead of continuous side walls or vias could change its properties and the design considerations. Thus, in the following subsections, we will discuss the main properties of a guiding structure: propagation constant, cut-off frequency and loss performance.

3.1.2 Propagation constant and cutoff frequency

Fig. 3.3.b depicts the geometry model of V-LIW with all impactful parameters. It should be noted that in this geometry, and also throughout the paper where it is not essential, the dielectric is made transparent to show more details of the designs. The discontinuities of side walls, realized by metallic slots, has an impact on the propagation constant and consequently on the cut-off frequency of the waveguide. This impact can be simulated with full-wave finite element commercial softwares such as HFSS (ANS) and HFWorks (HFW). It should be noted that, like any other SIW structure, since the current on the side walls cannot be continuous, the V-LIW only supports the propagation of TE_{n0} modes. The phase constant for dominant mode of V-LIW, TE_{10}, can be calculated from the phase difference between the transmission coefficients of two length of a line, given by (Deslandes & Wu (2002)):

$$\beta_{SIW} = \frac{\angle S_{21}^{L2} - \angle S_{21}^{L1}}{L_1 - L_2} \tag{3.1}$$

Furthermore, the cut-off frequency of V-LIW can be found by calculating the propagation constant for different frequencies and finding the frequency in which the real and imaginary parts of the propagation constant are equal (Deslandes & Wu (2006)). However, it would be beneficial to find the equivalent rectangular waveguide width as a function of V-LIW's parameters in order to estimate the phase constant of V-LIW in the guiding region to facilitate the analysis of this guiding structure. Later, this equivalent waveguide can be used in all design processes before the final simulation. An empirical expression in (Xu & Wu (2005b)) and a theoretical formula in (Che *et al.* (2008a)) have been presented for the equivalent rectangular waveguide width of the conventional SIWs with cylindrical vias, however those cannot be used here due to too much differences in the shape of vias between our work and those. In order to find the equivalent width, the propagation constant for a series of V-LIWs with different geometries has been calculated, then the width of rectangular waveguides which produce the same propagation constants has been found, and finally an empirical formula for equivalent

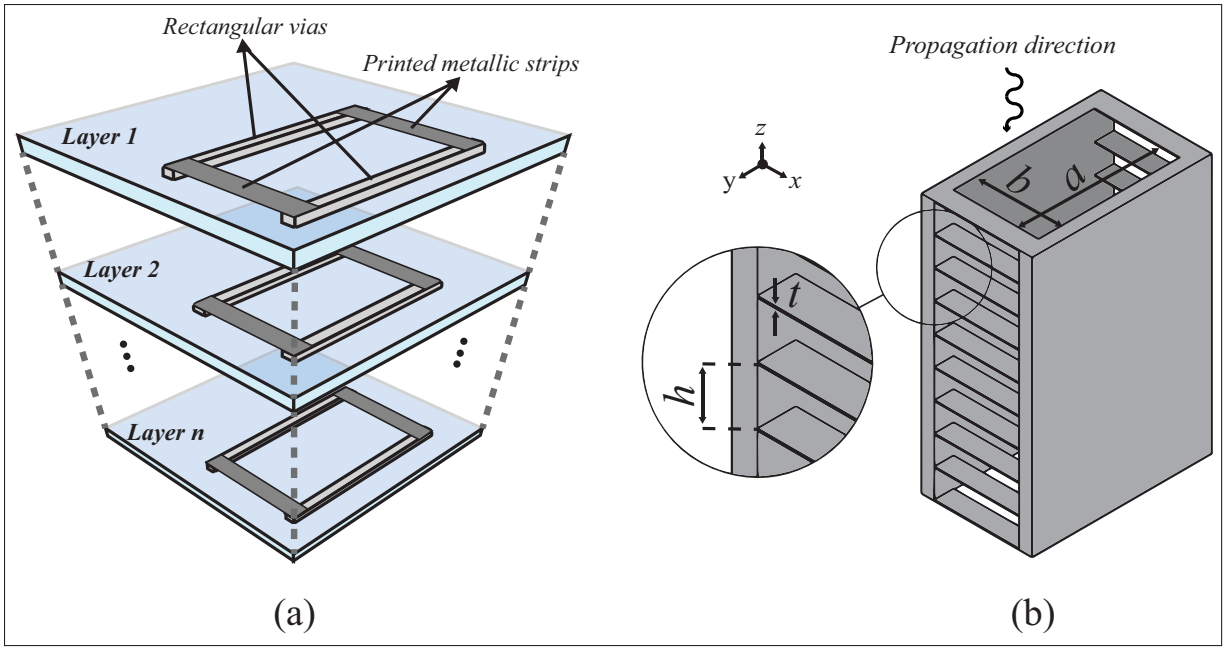

Figure 3.3 (a) Multilayer LTCC process forming V-LIW. (b) Geometry of Vertical LTCC Integrated Waveguide after stacking

width has been obtained by applying the least square approach (Chapra (2005)). This procedure leads to the following expression:

$$a_{eq} = a\left[0.995 + 0.2017\left(\frac{h-t}{a}\right) + 0.7748\left(\frac{h-t}{a}\right)^2 + 0.005\left(\frac{t}{h}\right)^2\right] \tag{3.2}$$

where a_{eq} is the equivalent rectangular waveguide width, a is the actual width of V-LIW, t is the thickness of printed metals, and h is the gap between two consecutive printed strips which equals to the number of layers between them times thickness of each layer. To verify the accuracy of (3.2), the phase constant for two different frequency bands, V-band and W-band, and also for two different widths of V-LIW are simulated and plotted in Fig. 3.4 and Fig. 3.5 along with the phase constant for rectangular waveguides with equivalent widths given by (3.2). It should be noted that the chosen dielectric for V-band and W-band are Dupont 9k7

(ε_r : 7.1) and Ferro A6M (ε_r : 6.21) respectively. As we can see in these figures, results are in agreement. In fact, (3.2) provides a precision better than 0.2% in the non-dispersive region and it is valid for $h << \lambda_g/2$.It should be noted that for the case, t equals to h, a_{eq} approaches a. This behaviour follows our expectation from the geometry of our integrated waveguide, where the V-LIW becomes a simple rectangular waveguide.

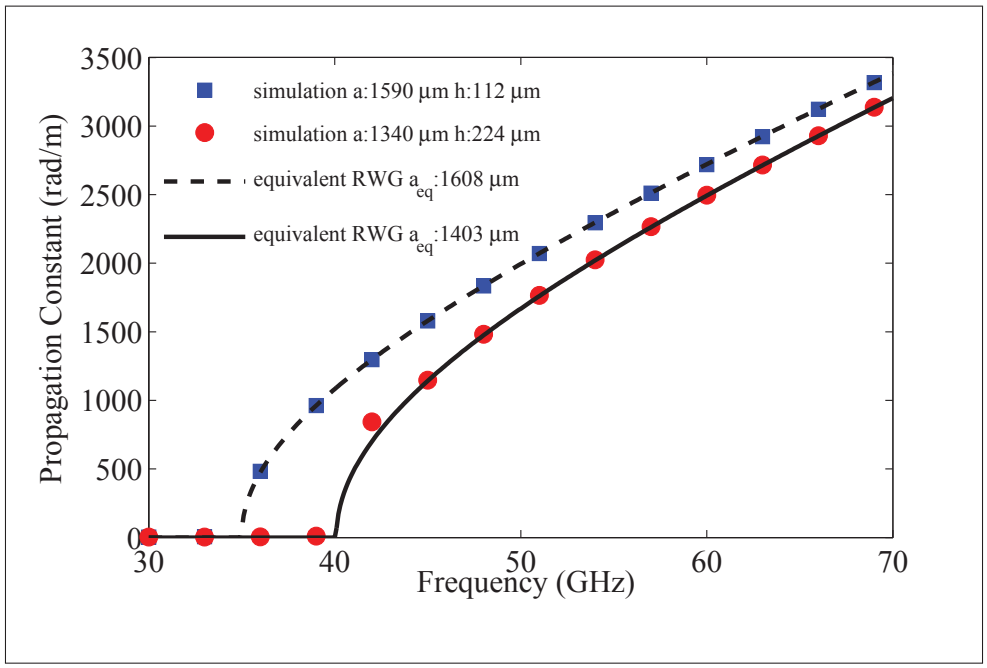

Figure 3.4 Comparison between phase constant of equivalent rectangular waveguide and simulated of V-LIW in V-band

3.1.3 Loss mechanism

RF signals passing through the V-LIW are attenuated due to losses. α_T is the total attenuation constant of V-LIW and like any other guiding structure, has three parts: Conductor loss (α_C), Dielectric loss (α_D) and Radiation loss (α_R):

$$\alpha_T = \alpha_C + \alpha_D + \alpha_R \tag{3.3}$$

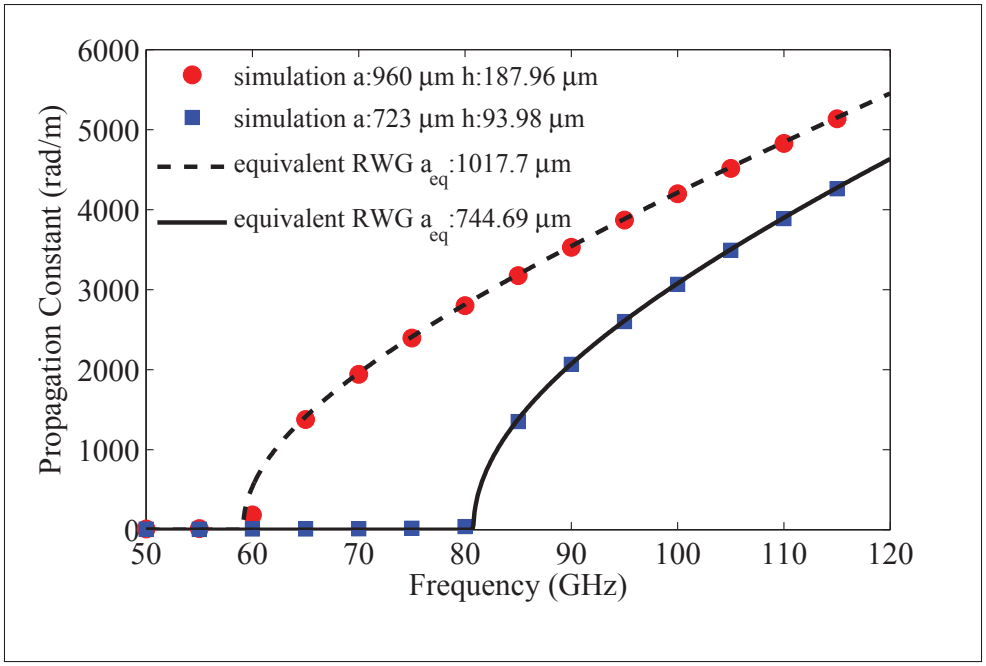

Figure 3.5 Comparison between phase constant of equivalent rectangular waveguide and simulated of V-LIW in W-band

The first two parts are due to the lossy materials with which the V-LIW is constructed and they are almost identical to the ones for the conventional filled rectangular waveguide with the same dimensions and materials, given by (Pozar (2009)):

$$\alpha_D = \frac{k^2 tan\delta}{2\beta} \tag{3.4}$$

$$\alpha_C = \frac{R_s}{a^3 b\beta k\eta}(2b\pi^2 + a^3k^2) \tag{3.5}$$

where k is the wave number of the unbounded homogeneous medium, β is the phase constant, Rs is the surface resistivity, $tan\delta$ is the dielectric loss tangent of LTCC green tapes, and η is the intrinsic impedance of the waves in the dielectric.

For LTCC systems with crystallizing dielectric like DuPont 9k7 and Ferro A6M, which are usually used in the millimeter waves, the dielectric loss tangent at frequencies around 60 GHz

is about 0.001 ± 0.0005 leads to a dielectric loss about $0.2\,\mathrm{dB/cm}$ from (3.4). Furthermore, the metals in LTCC systems are usually silver and gold with the conductivity of 6.1×10^7 and 4.1×10^7, respectively. The conductor loss factor for these conductivities lies in about $0.15\,\mathrm{dB/cm}$ using (3.5).

Radiation loss, unlike conductor and dielectric loss, depends on the form and geometry of the waveguide. Since the V-LIW is not a closed structure and it does not have complete walls on all sides, a part of travelling signal radiates from the gaps between the slots forming the side walls. In order to calculate radiation loss, one can use numerical methods or full-wave simulation software. The attenuation constants, extracted from simulation, for a V-LIW designed for V-band is illustrated in Fig. 3.6.

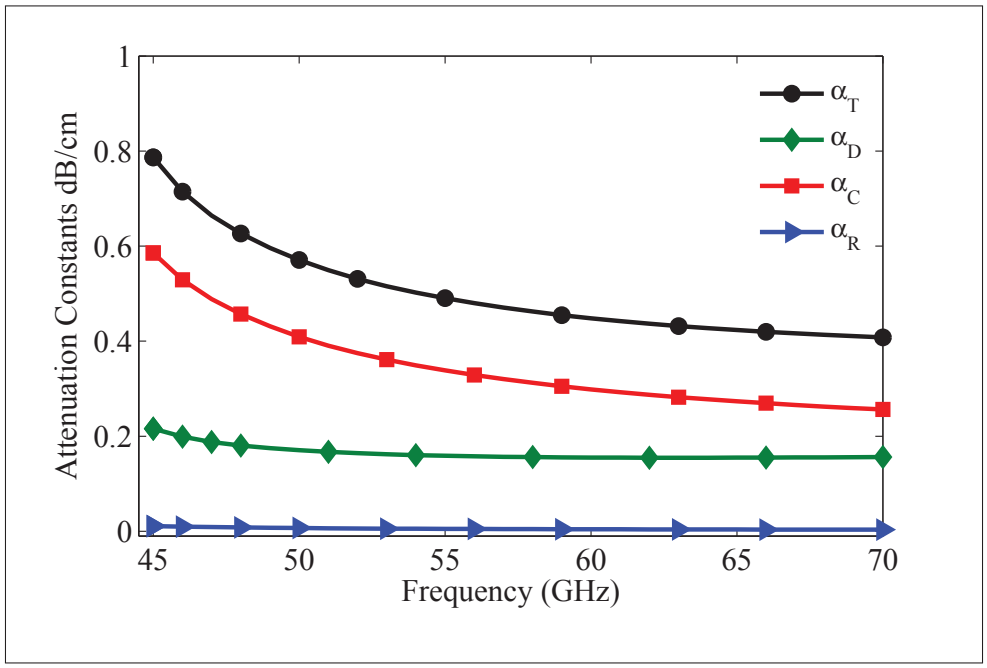

Figure 3.6 Attenuation constants for a V-LIW at V-band;
$a : 1340\mu m, b : 700\mu m, h : 224\mu m, t : 8\mu m$,
and surface roughness $2\mu m$

For this waveguide, which is a practical V-LIW of interest, the radiation loss is almost zero. However, if the pitch of printed strips increases, by increasing the number of layers between

the printed strips or using thicker LTCC layers, the radiation loss will increase. Nominal LTCC tape thickness range from 20 μm to 300 μm for a single tapes. To assess the impact of spacing between strips on rdaiation, Fig. 3.7 shows the simulated radiation loss versus the normalized spacing between strips (h) at 60 GHz, the mid-band frequency at V-band. From this figure and with the previous knowledge that the conductor and the dielectric losses are about 0.2 dB/cm and 0.1 dB/cm respectively, we can find that the pitch should be smaller than the quarter of wavelength before the radiation loss becomes dominant. This condition could be always met without difficulty; noticing that the thickness of LTCC green tapes is usually less than 300 μm which is much smaller than the wavelength in millimeter-wave frequencies. On the other hand, considering that 20 μm LTCC green tapes (Ferro A6M) have recently been available, the proposed V-LIW potentially works up to 1.5 THz before the radiation loss becomes dominant. Fig. 3.7 shows different regions of V-LIW operatoin when the spacing between printed metalic strips increases. In this plot, the guiding region is the region where radiation loss is not dominant and is less than conductor and dielectric losses. The leakage region is the region where the radiation part is larger than the conductor and dielectric loss by several orders and V-LIW can be used in the design of applications like an antenna. Between these two regions, the structure has radiation losses too high to be a viable waveguide and too low to be a leaky-wave antenna. This region, known as the forbidden region (Deslandes & Wu (2006)), should be avoided.

3.2 V-LIW circuits building blocks

In order to use V-LIW interconnections in a millimeter-wave system and also to be able to realize V-LIW passive circuits, certain building blocks which are commonly utilized in numerous communication systems are introduced here. These blocks include (i) Transition from WR15 (WR10), standard waveguide for V-band (W-band), to the V-LIW (ii) Transition from CPW to V-LIW, and (iii) Transition from conventional horizontal LIW to the V-LIW (90-degree bend) (iv) T-Junction. A back to back transition from CPW to V-LIW, which is essentially a combination of transition (ii) and (iii), is also presented.

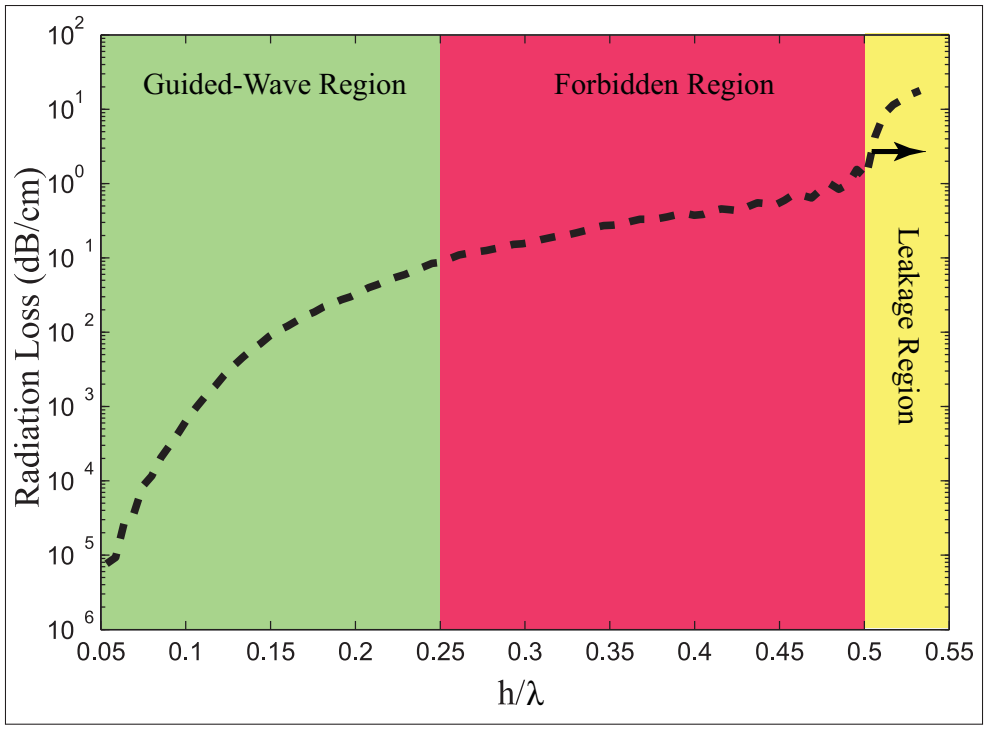

Figure 3.7 Radiation loss for a V-LIW as a function of the pitch of printed strips normalized to the wavelength at 60 GHz; $a : 1340\mu m, b : 700\mu m, h : 224\mu m, t : 8\mu m$, and surface roughness $2\mu m$

3.2.1 Transition from V-LIW to standard waveguides

Waveguide adaptors are widely used to connect millimeter-wave components to measuring equipment. These adaptors essentially consist of pieces of hollow waveguides, and a flange for joining sections. The dimensions of these hollow waveguides are generally identical to the standard waveguide for the desired band of frequency. A transition from the proposed V-LIW to those empty standard waveguide should, therefore, be considered for measurement by these adaptors.

For the same cut-off frequency, the dimension of V-LIW and the standard waveguide are very different, since the V-LIW is a type of high permittivity dielectric filled waveguide contrary to standard air-filled waveguides. Thus, to have a smooth transition, the dimensions of the waveguide should progressively be increased and also the dielectric should gradually be removed.

The geometry of designed transition is illustrated in Fig. 3.8.

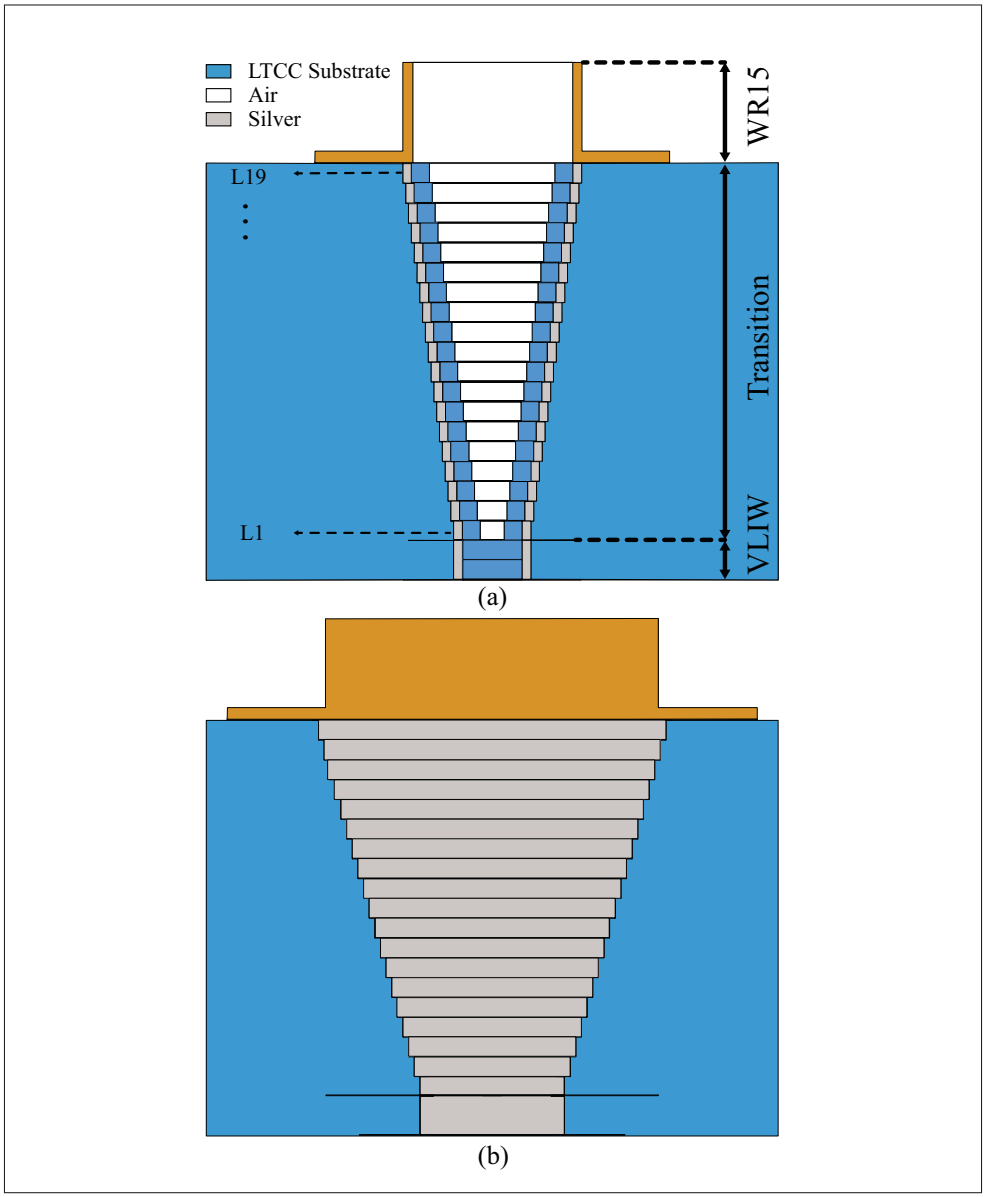

Figure 3.8 Geometry of transition from standard waveguides to V-LIW (a) front view and (b) side view

This transition is designed for V-band frequencies and it consists of 19 LTCC green tape layers, with the thickness of 224 µm each. The width and height of the waveguide are linearly increased in each layer to go from V-LIW's width and height to the ones for WR15, the V-

band standard waveguide. As a starting point, the dimension of cavities can be selected by Klopfenstein impedance taper method (Pozar (2009)) for the transition of the wave impedance from V-LIW to WR15. Klopfenstein method guarantees the optimum return loss for a given taper length (Pozar (2009)), however it is not true in our case. This is because there are unavoidable slabs of dielectric next to the rectangular vias which are needed for the mechanical integrity of the structure in the fabrication process. These slabs make it impossible to realize the required impedance, needed by Klopfenstein method, in the last several layers toward the standard waveguide. Therefore, the dimensions of the cavities should be optimized to obtain the best result.

It should be noted that, if one is interested only in a portion of the band, not the entire V-band, the length of transition could be significantly smaller. In order to show this, here we also optimized this transition with only 8 LTCC layers for operating frequencies from 57 GHz to 64 GHz, which is a very popular unlicensed band of interest in V-band. Furthermore, a same type of transition in W-band, from V-LIW to WR10, is designed and simulated. All optimized dimensions for these three transitions are listed in Table. 3.1 and the simulation results are shown in Fig. 3.9, Fig. 3.10, and Fig. 3.11. It should be noted that although this transitions shows good performance on entire band, they are still subject to all limitations and drawbacks of rectangular waveguide like dispersion region and higher order modes.

A pair of optimized transition for V-band frequencies has been fabricated and measured in a back to back configuration using WR15 waveguide adaptors and N5247A PNA-X network analyzer. Photographs of fabricated transition are shown in Fig 3.12. A TRL calibration has been carried out to eliminate the effect of waveguide adaptors (Williams (2010)). The measurement and the simulation results for the entire back to back transitions are plotted in Fig 3.13. Furthermore, this transition enables us to solely measure a V-LIW transmission line using TRL calibration at V-band and extract its loss performance. Fig. 3.14 compares the simulated and measured loss performance of fabricated V-LIW. Overall, the measured return loss is better than 15 dB from 53 GHz to 67 GHz.

Table 3.1 Parameters of V-LIW to the standard waveguides transition

Parameters	**V-band**	**Unlicensed 60 GHz**	**W-band**
LTCC type	Dupont 9k7	Dupont 9k7	Ferro A6M
Permittivity	7.1	7.1	6.21
Number of layers	19	8	16
a	1340 μm	1340 μm	960 μm
b	672 μm	672 μm	336 μm
Layers' Thickness	224 μm	224, μm	187 μm
Slab's width	400 μm	400 μm	400 μm
W1	214 μm	350 μm	203 μm
W2	363 μm	683 μm	356 μm
W3	496 μm	1025 μm	509 μm
W4	627 μm	1386 μm	664 μm
W5	760 μm	1708 μm	821 μm
W6	890 μm	2095 μm	979 μm
W7	1000 μm	2975 μm	1138 μm
W8	1150 μm	3205 μm	1296 μm
W9	1310 μm	-	1454 μm
W10	1480 μm	-	1609 μm
W11	1650 μm	-	1762 μm
W12	1820 μm	-	1912 μm
W13	2070 μm	-	2058 μm
W14	2390 μm	-	2201 μm
W15	2575 μm	-	2340 μm
W16	2670 μm	-	2476 μm
W17	2800 μm	-	-
W18	3150 μm	-	-
W19	3554 μm	-	-

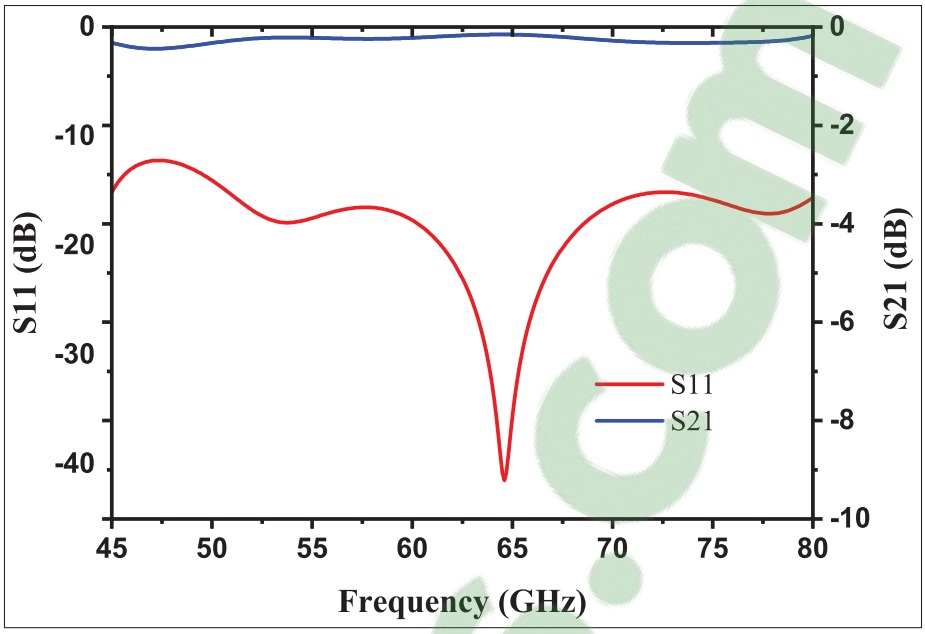

Figure 3.9 Simulation results for transition from V-LIW to WR15 standard waveguide for V-band

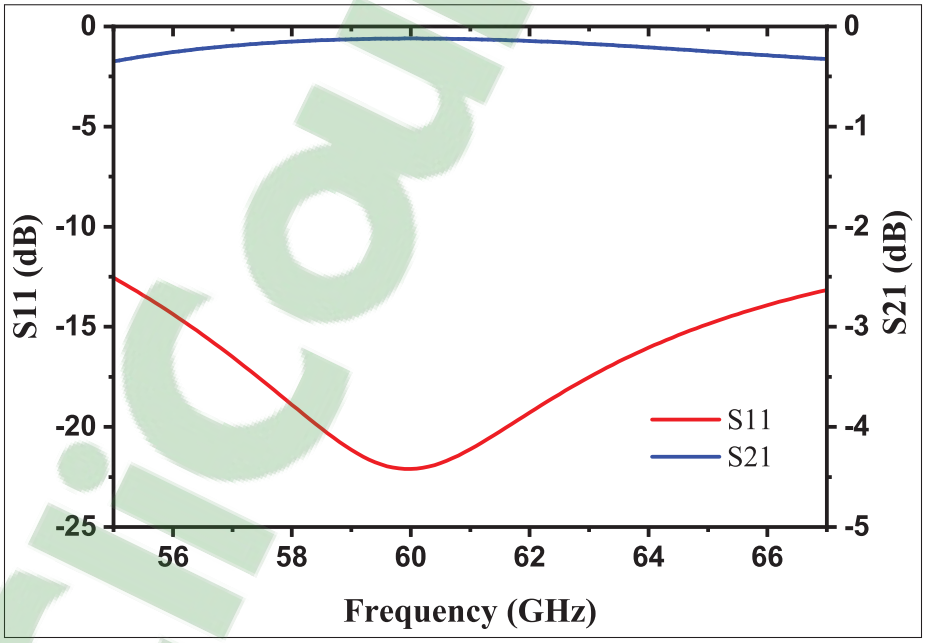

Figure 3.10 Simulation results for transition from V-LIW to WR15 standard waveguide for unlicensed 60 GHz

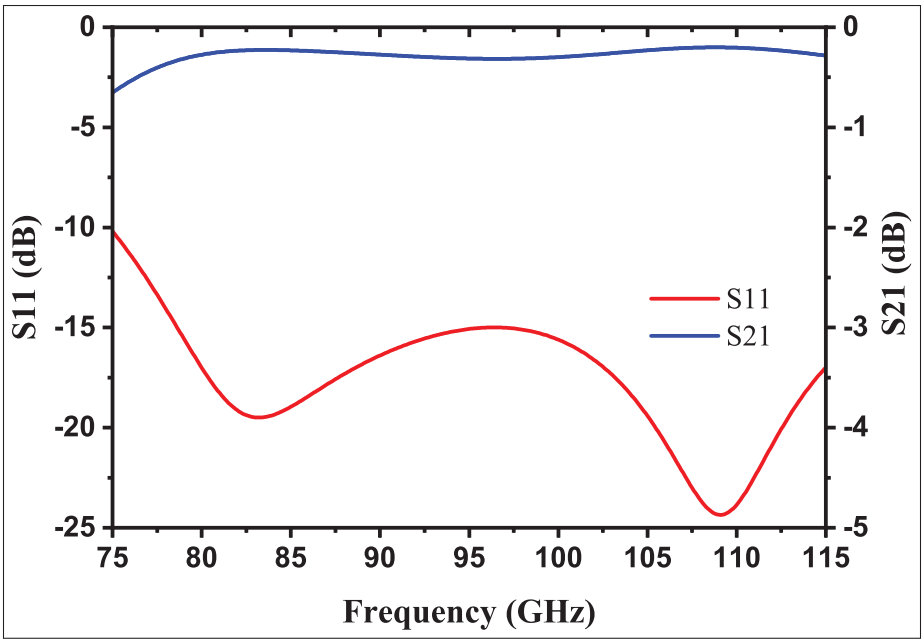

Figure 3.11 Simulation results for transition from V-LIW to WR10 standard waveguide for W-band

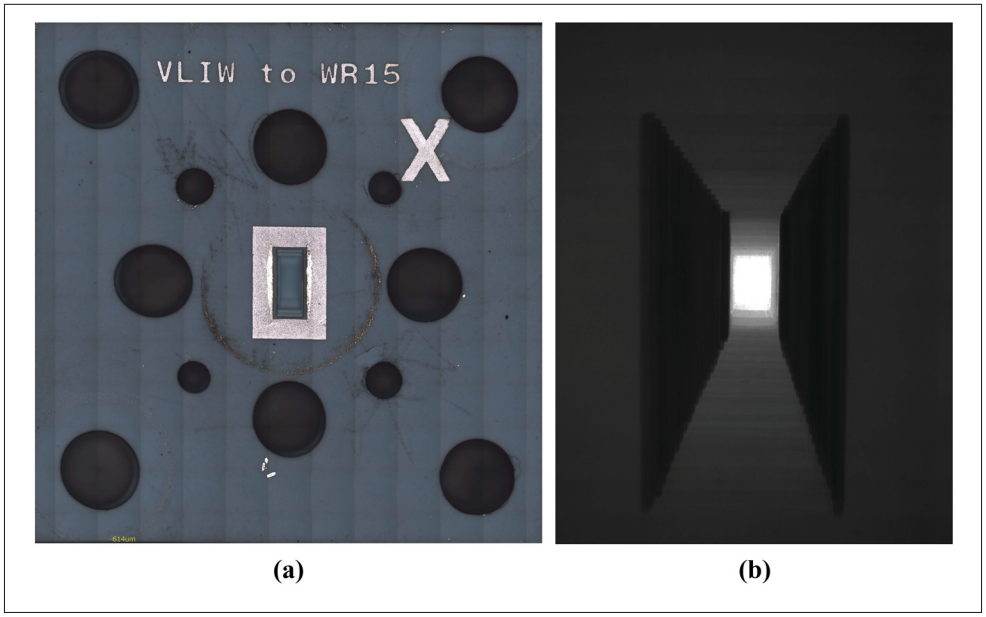

Figure 3.12 Fabricated transition from V-LIW to the standard waveguide for V-band frequencies; (a) top view photograph (b) X-ray photograph of inside of transition

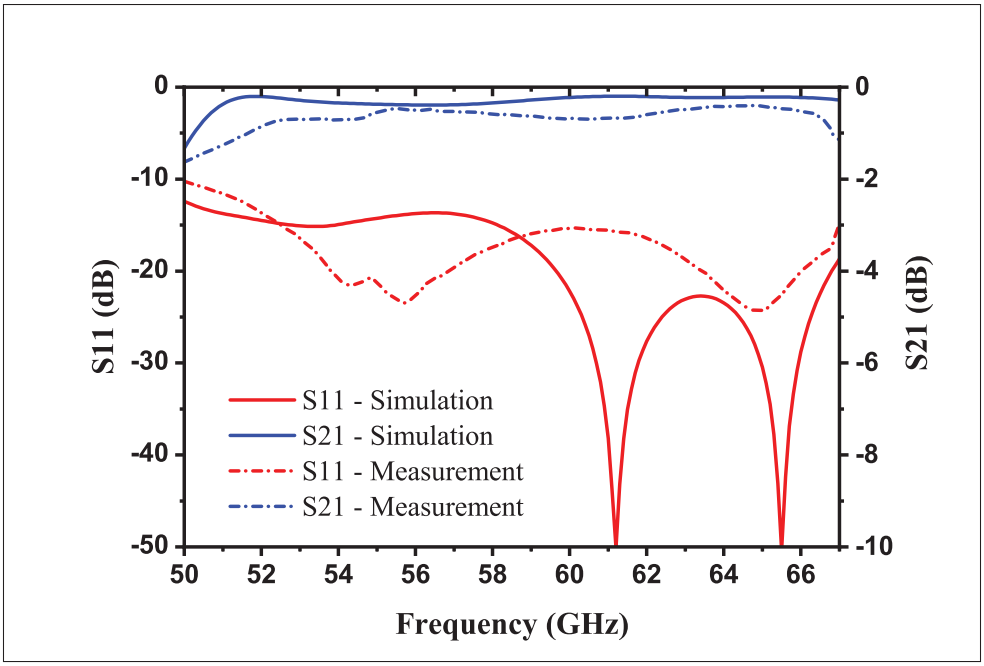

Figure 3.13 Simulation and measurement results for back to back transition from V-LIW to WR15

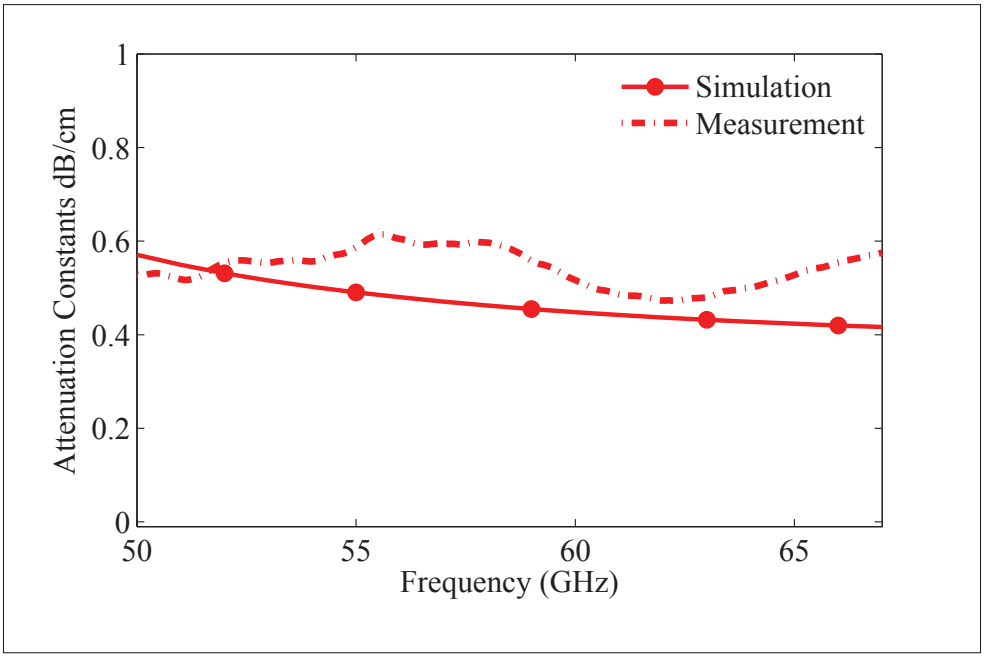

Figure 3.14 Simulated and measured loss performance of a V-LIW transmission line at V-band frequencies

3.2.2 Transition from V-LIW to CPW

The interconnection between the V-LIW and other millimeter-wave components such as active devices and MEMS switches usually requires a transition to planar transmission lines. This transition can also be used to connect the V-LIW passive components to high-frequency CPW measurement probes.

Fig. 3.15 and Fig. 3.16 depict two proposed transitions from V-LIW to CPW. In these transitions, an L-shape loop is used to excite TE_{10} mode of V-LIW and then this loop connects to a CPW line. These two transitions are almost the same except in the former the CPW is directly connected to the V-LIW, while in the latter one layer of half coaxial line is used between V-LIW and CPW.

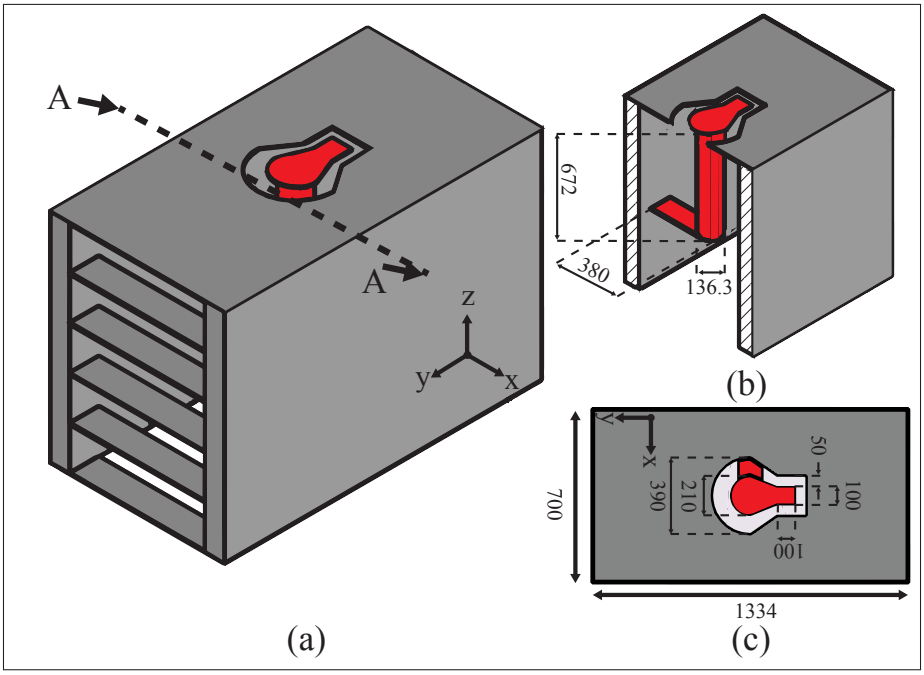

Figure 3.15 (a) Geometry of direct V-LIW to CPW transition (Transition 1), (b) section cut at AA, and (c) top view. Dimensions are given in μm

The idea of waveguides excitation with an L-shape loop has been previously used in the end-launcher coaxial to waveguides transitions (Wheeler (1966)). As it can be seen in the Fig. 3.15,

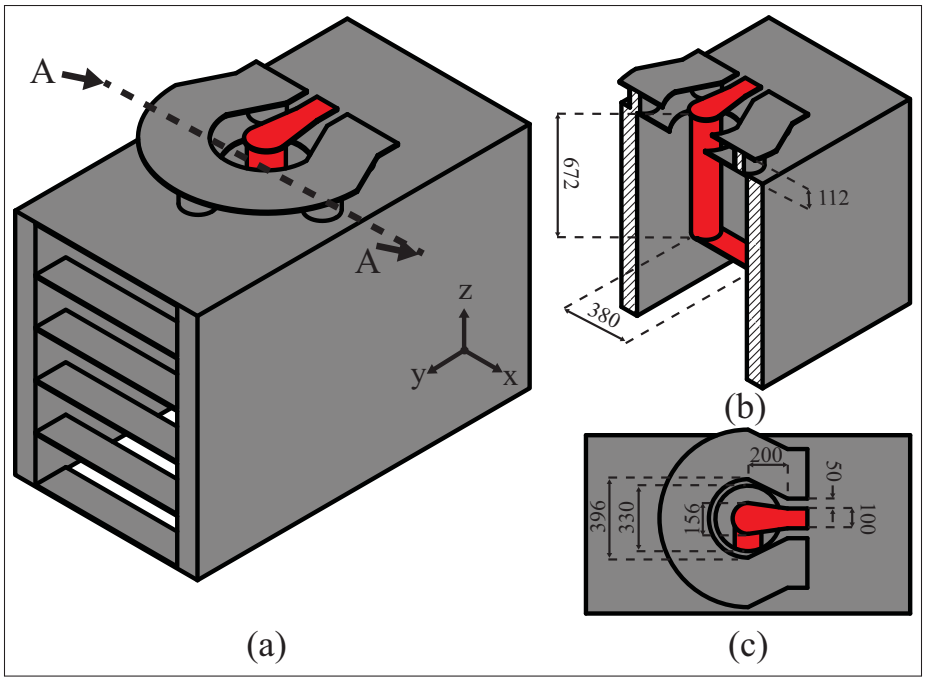

Figure 3.16 (a) Geometry of V-LIW to CPW transition by one layer half coax middle section (Transition 2), (b) section cut at AA, and (c) top view. Dimensions are given in μm

a via-probe which is shorted to the body of V-LIW forms a current loop to excite magnetic fields of TE_{10} mode. The length and the position of this via-probe, and also the length and the width of the shorting strip should be selected as such the transition provides the same impedance as the CPW line on the top. The analytical expression for real and imaginary parts of the input impedance in a waveguide entrance using the loop coupling model and the probe coupling model have been provided in (Deshpande *et al.* (1979)) and (Saad (1990)), however since not every length of via-probes can be fabricated and we are limited to the discrete number of LTCC layers, an optimization using commercial softwares is required to obtain best possible matching and return loss. The proposed transition has been simulated and optimized using ANSYS HFSS to operate at 60 GHz. The optimized dimensions for these transitions considering the Dupont 9k7 tapes are shown in the geometry figures. The simulated scattering parameters of these transitions are illustrated in Fig. 3.17. As it is expected for a probe-type transition, about 10 percent fractional bandwidth is achieved. This is mainly because the inductance of the via-probe, which should be cancelled during the transition, is highly frequency dependent.

It should be noted that the optimized direct transition shows better return loss and it is good for the case where one wants to test a V-LIW component. On the other hand, the second transition with a half coaxial is more convenient than the first transition for integration with other components.

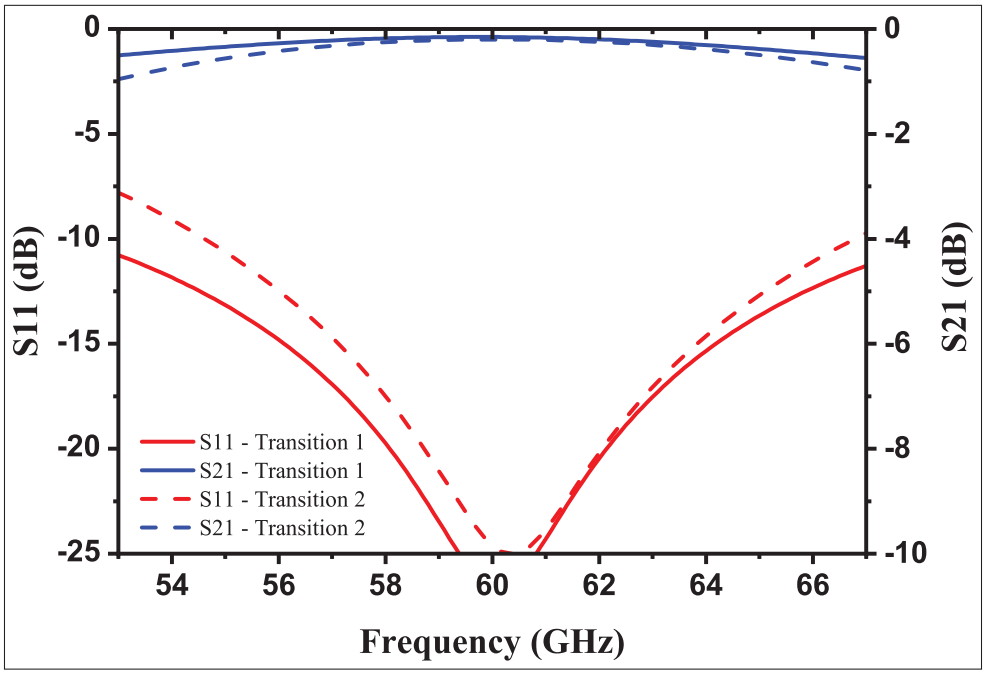

Figure 3.17 Simulation results for the transitions from V-LIW to CPW

3.2.3 Transition from V-LIW to H-LIW

Completing V-LIW library to be used in microwave systems still needs another transition; a transition to conventional SIW which, for the sake of uniformity of notation is called horizontal LTCC Integrated Waveguide (H-LIW) here. This transition, which is essentially a 90-degree bend, along with the previous transition to CPW, enables us to transfer electromagnetic waves from the top layer to the buried layers using V-LIW and then bring it back to the top.

The geometry of proposed transition is illustrated in Fig. 3.18. This transition consists of two parts: (i) the part in the V-LIW is an L-Shape end-launcher transition which is discussed in

the previous subsection, and (ii) the part in H-LIW which is a probe type waveguide transition from the broad-wall.

The operation mechanism of the proposed transition in the second part is based on the probe excitation of rectangular waveguides which is widely used in the design of coaxial to conventional waveguides transitions (Wade (2006); Fabregas *et al.* (1992)) and also more recently in CPW to SIW transitions (Mukherjee *et al.* (2013); Deslandes & Wu (2005)). In this type of transitions, a metallic probe rod operating as a monopole antenna excites the electric field inside the waveguide. This probe is placed vertically along to the smaller side of the waveguide to be parallel to electrical fields of TE_{10} mode (Singh & verma (2009)). Furthermore, a short-circuiting plane at a distance behind the probe is required to ensure the proper radiation in waveguide propagation direction (Fabregas *et al.* (1992)). The distance for the case that we neglect the inductance of the probe is a quarter wavelength, but in fact, for a practical case, it must be less than that to cancel out the inductance introduced by the probe rod. This distance along with the length, the diameter, and the off-center positioning of the via are the parameters of the transition that should be optimized to achieve a smooth transition from V-LIW to the H-LIW. An experimental method to design this type of transitions is presented in (Wade (2006)). Furthermore, Mumford in (Mumford (1953)) showed that with only two of three parameters including length, off-center positioning and distance to the short-circuiting plane of probe rod, one can match any impedance less than waveguide characteristic impedance. Moreover, a method to find optimum dimensions to provide the widest possible bandwidth for a waveguide to coaxial cable transition is provided in (Mumford (1953)).

An alternative way to realize the transition from V-LIW to H-LIW is to make a quarter-wavelength corner using steps formed by rectangular vias, Fig. 3.19. This transition can provides us better bandwidth. However, by respecting the minimum via to via spacing for our in-house LTCC process, this transition has slightly more insertion loss due to small radiation from corners.

The proposed transition and the corner transition, considering Dupont 9k7 dielectric, have been optimized using ANSYS HFSS at 60 GHz. The simulation results are plotted in the Fig. 3.20 and it shows that the optimized transitions cover the entire unlicensed band around 60 GHz.

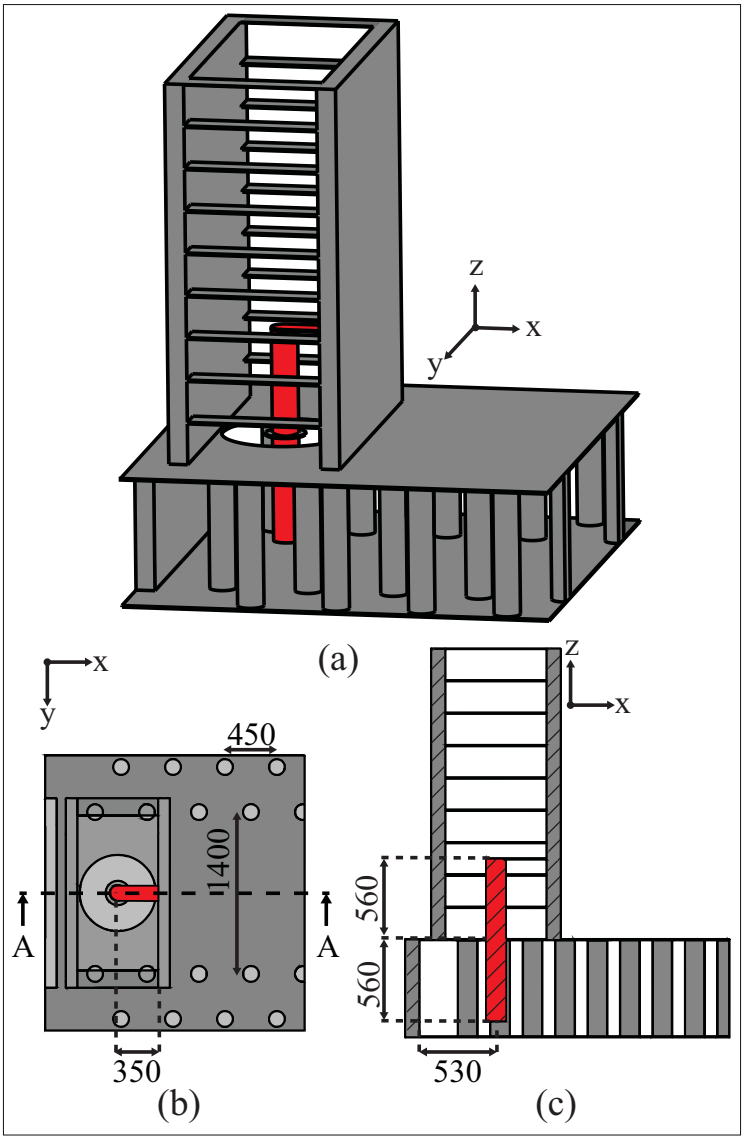

Figure 3.18 Geometry of V-LIW to H-LIW transition
(a) 3D view (b) top view (c) section cut at AA

In order to examine the proposed transitions and verify the simulation results, a back to back structure consists of both transitions to CPW and H-LIW is designed and fabricated. As it is

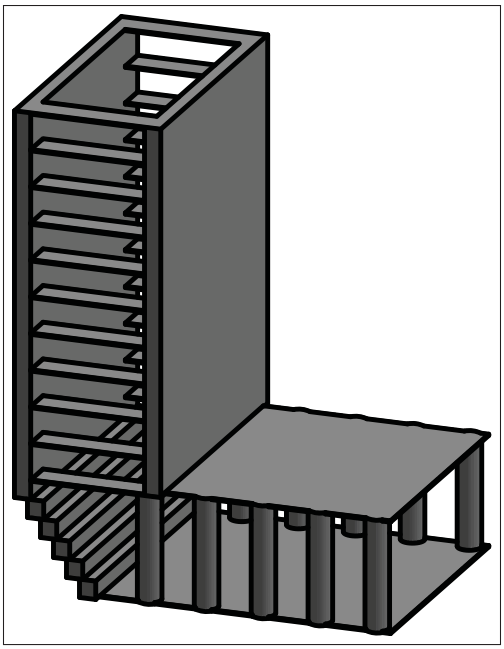

Figure 3.19 Geometry of V-LIW to H-LIW corner transition

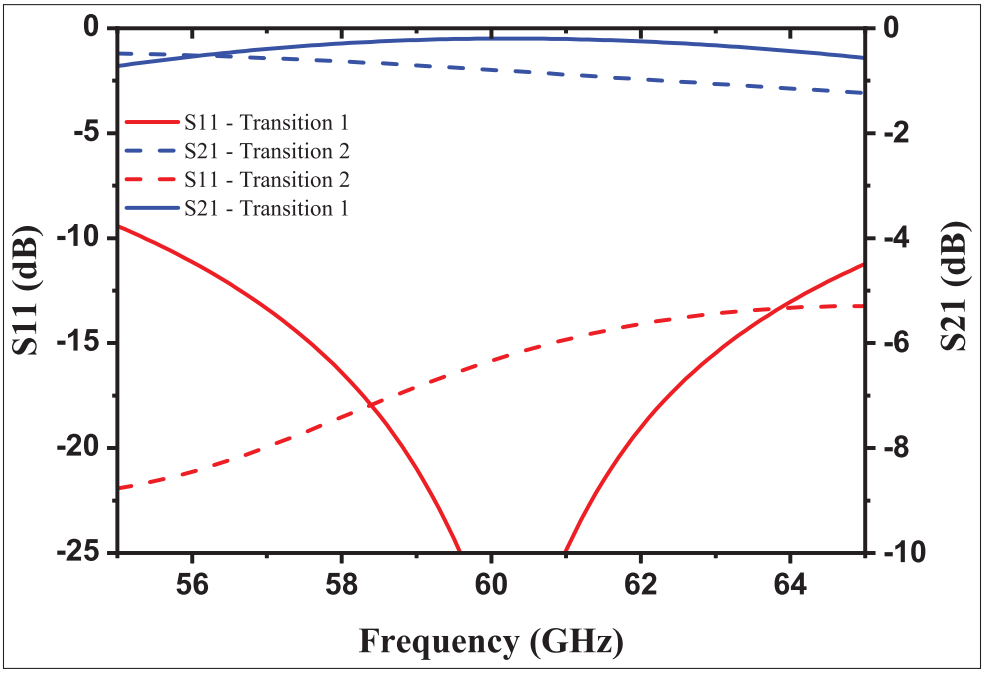

Figure 3.20 Simulation results for transition from V-LIW to H-LIW

depicted in Fig. 3.21, this structure at both sides is terminated to the CPW lines and it can be easily measured using high-frequency CPW probes. The simulation and measurement results of the back to back transitions are plotted in Fig. 3.22 which shows a good agreement between simulation and fabrication.

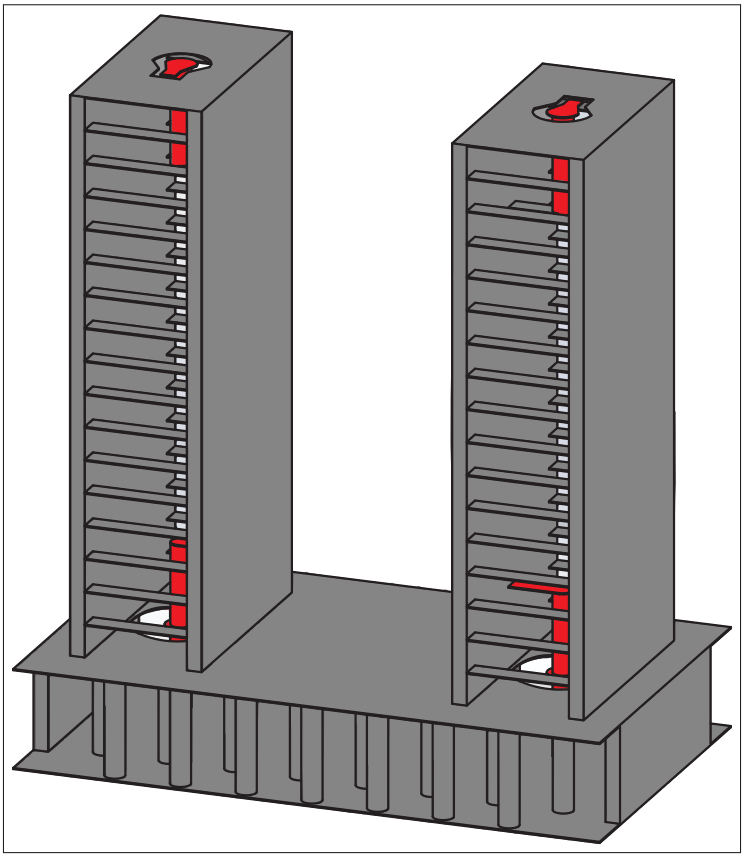

Figure 3.21 Geometry of the back to back transition

3.2.4 V-LIW T-Junction

One of the main blocks in many communication systems such as feeding networks of antennas, is a Tee waveguide junction. Fig. 3.23 shows the geometry of an E-plane V-LIW T-junction, which is not easy to realize with conventional SIWs. In the middle arm of proposed design, a three layers pseudo-wedge is added. This pseudo-wedge helps to optimize the power division and minimize the return loss (Yang & Fathy (2009); Hirokawa *et al.* (1991)).

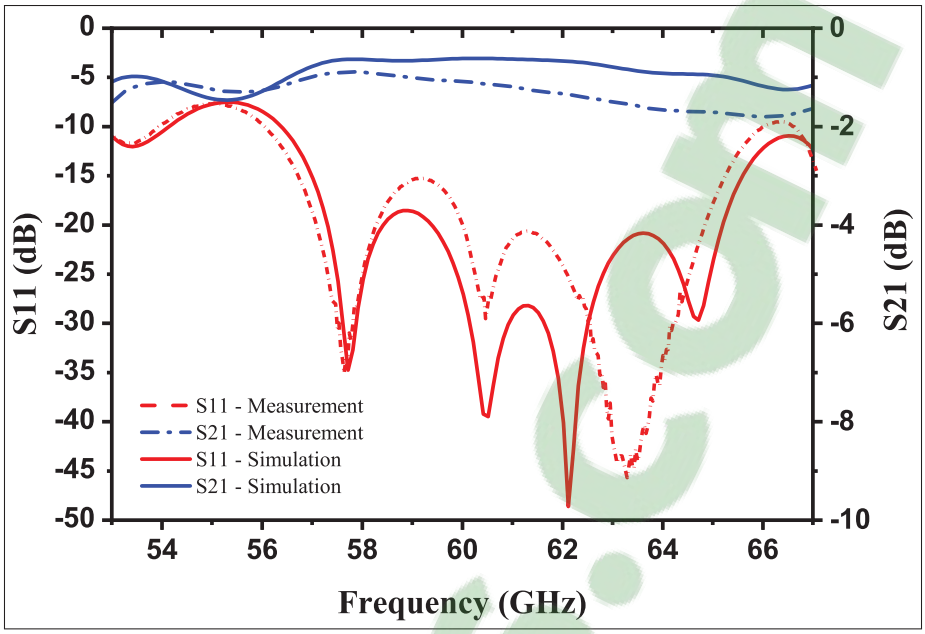

Figure 3.22 Simulation and measurement results of the back to back structure from V-LIW to CPW

The designed T-junction has been optimized for the unlicensed band around 60 GHz. The optimized scattering parameters of this structure are plotted in Fig. 3.24.

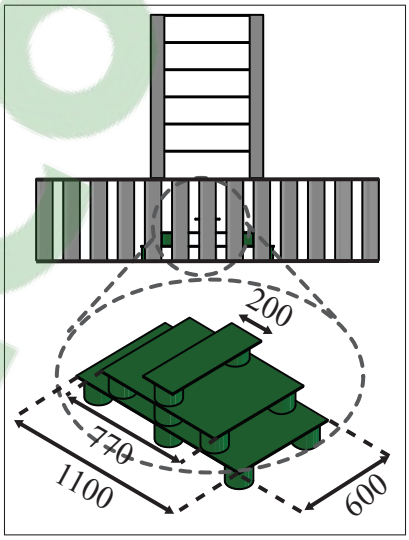

Figure 3.23 Geometry of E-Plane V-LIW T-Junction side view, and matching wedge

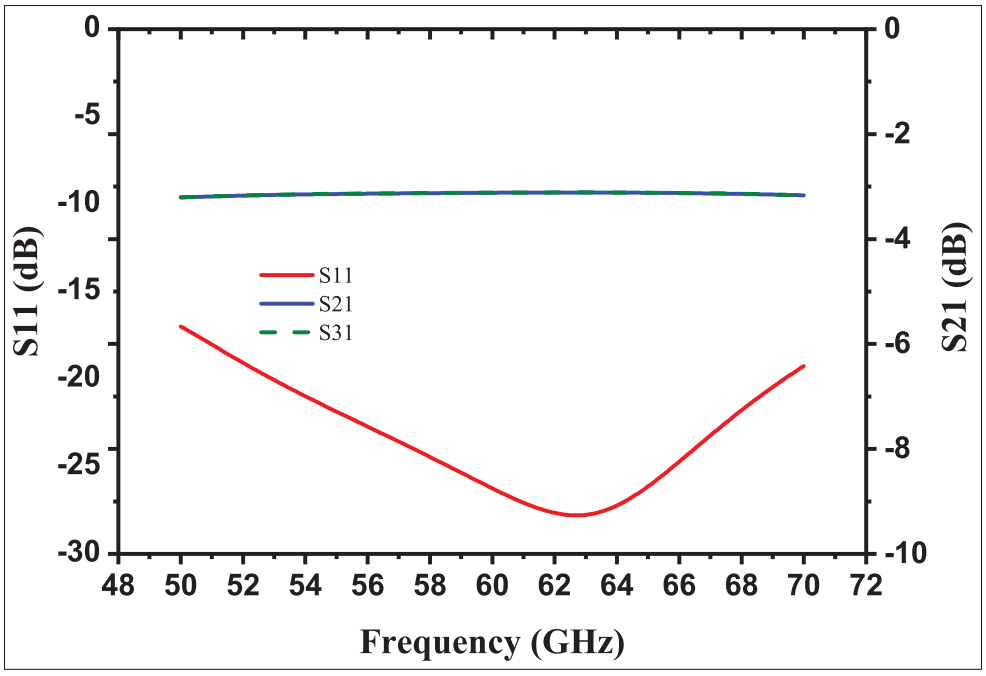

Figure 3.24 Simulation results of a T-Junction V-LIW

3.3 V-LIW application to design passive circuits

The Proposed Vertical LTCC Integrated Waveguide has been fully characterized in the previous sections together with the main building blocks which are required to realize almost every communication system. In this section, the V-LIW's interesting features and capabilities, will be demonstrated by designing and testing three frequently used passive components: a E-plane power divider, a coupler, and two filters.

3.3.1 V-LIW E-Plane power divider

The E-plane power divider, as a basic component, is widely used to introduce new guiding lines (Germain *et al.* (2003); Parment *et al.* (2015b)). As one of the interesting capability of our proposed V-LIW transmission line, we designed a highly compact anti-phase E-plane T-junction power divider. The geometry of the designed power divider is illustrated in Fig. 3.25. This power divider is essentially a combination of a V-LIW T-junction, two 90-degree V-LIW bends, and the CPW to V-LIW transitions which are used in the input and output sections, to

conveniently measure the power divider with CPW probes. Moreover, a 90-degree CPW bend is attached to two of the outputs to facilitate probe alignment in the 3-port measurement set-up.

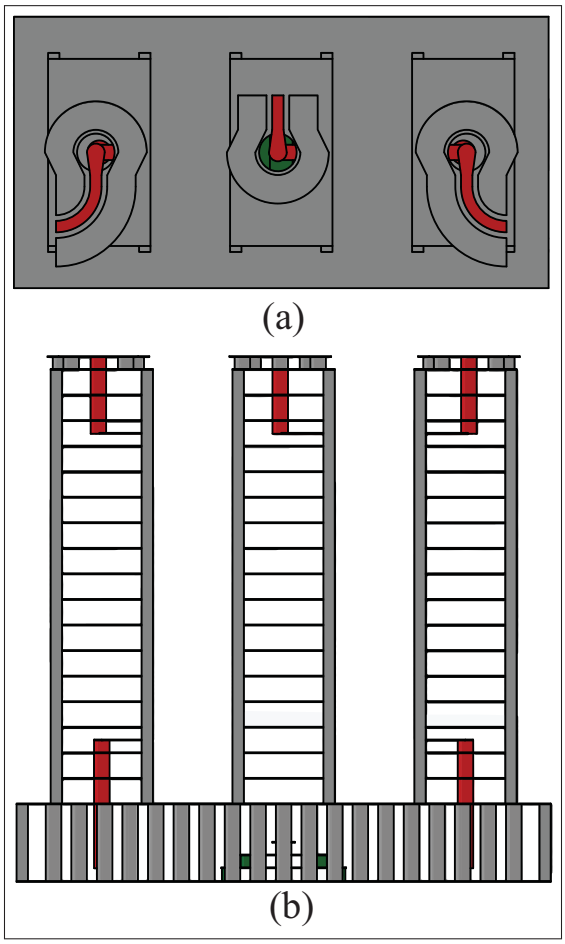

Figure 3.25 Geometry of V-LIW E-plane power divider (a) top view, and (b) side view

The designed power divider has been optimized to operate between 57 GHz and 64 GHz; in the unlicensed segment of the V-band. The simulated and measured return loss and insertion loss are given in Fig. 3.26. This figure shows the designed power divider has a return loss of better than 14 dB (11.4 dB measured) over the entire unlicensed band. The simulation transmission loss from port 1 to port 2 and port 3 are 3.8 ± 0.1 in the desired band. An amplitude imbalance

of ± 0.05 dB (0.5 dB measured) and a phase imbalance of better than $\pm 0.8^{\circ}$ (0.8° measured) has been achieved for this power divider.

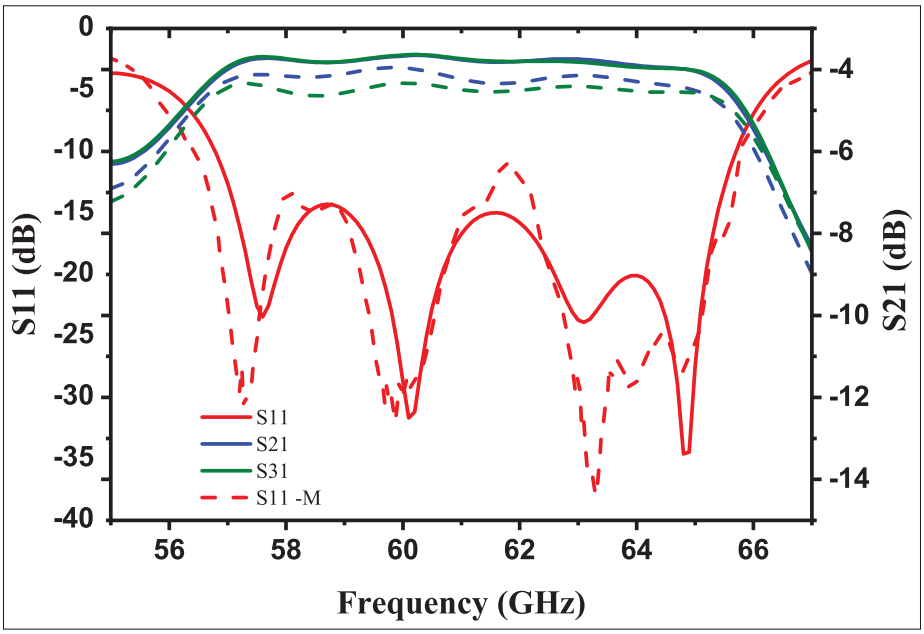

Figure 3.26 Scattering parameters of the V-LIW E-Plane power divider. Solid lines are simulated and dash-lines are measured results

3.3.2 V-LIW multihole bethe directional coupler

Another basic component that we have selected to implement by our new guiding structure is multi-hole Bethe coupler. This type of couplers consists of one or several small holes that couple the wave from a rectangular waveguide to another which have a broad wall in common (Pozar (2009)). The holes could be circles, rectangles or any arbitrary shapes, however, we are limited to the rectangular holes for implementation with V-LIW.

The designed V-LIW directional coupler in V-band frequencies is illustrated in Fig. 3.28. It is worth mentioning that to realize the apertures between the V-LIWs, we have partially drilled the rectangular vias in corresponding layers, thus the non-drilled parts works like a coupling aperture between two waveguides.

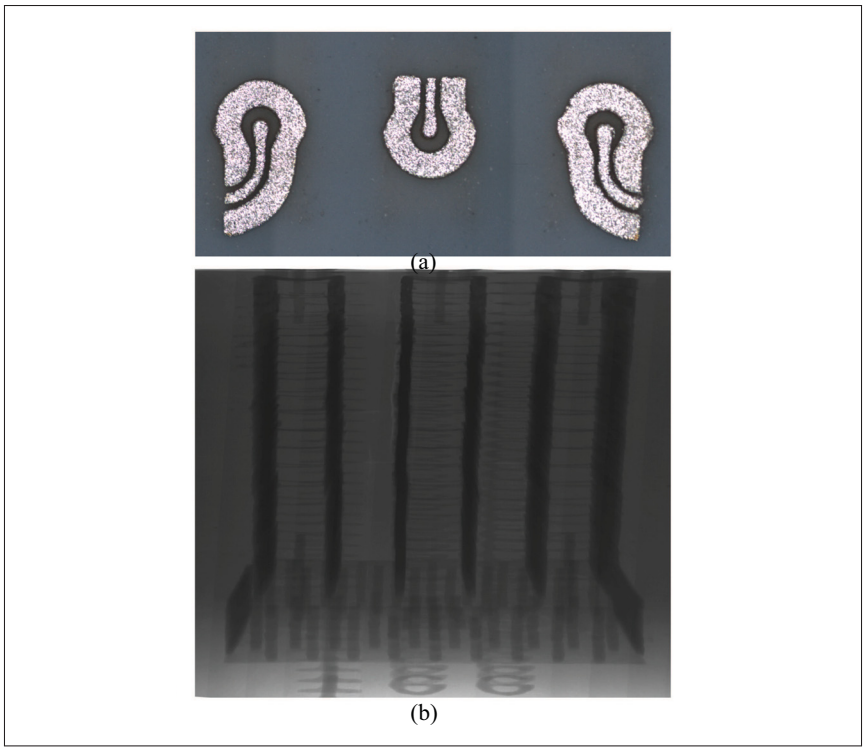

Figure 3.27 Fabricated E-plane power divide, (a) top view photograph (b) X-ray photograph of inside of LTCC

In order to find the parameters in this geometry, we followed the design procedure presented in (Pozar (2009)) with some modifications for the rectangular slot. Following this procedure, it can be found that the spacing between the center of the rectangular slot and the center of the waveguide (s) should be a quarter of the waveguide's width ($a/4$) to maximize the isolation. Subsequently, with this spacing, the coupling for two identical rectangular slots is given by:

$$C(dB) = -20log\left(\frac{\pi\varepsilon\omega\beta^2}{16P_{10}k^2}\right) - 20log(2l_a w_a^2) \tag{3.6}$$

where P_{10} is defined by:

$$P_{10} = \frac{ab\beta}{k\eta} \tag{3.7}$$

It should be noted that in the derivation of (3.6), the electric and magnetic polarizabilities of a rectangular slot are considered identical and equal to $\frac{1}{16}\pi l_a w_a^2$ (Montgomery *et al.* (1948)).

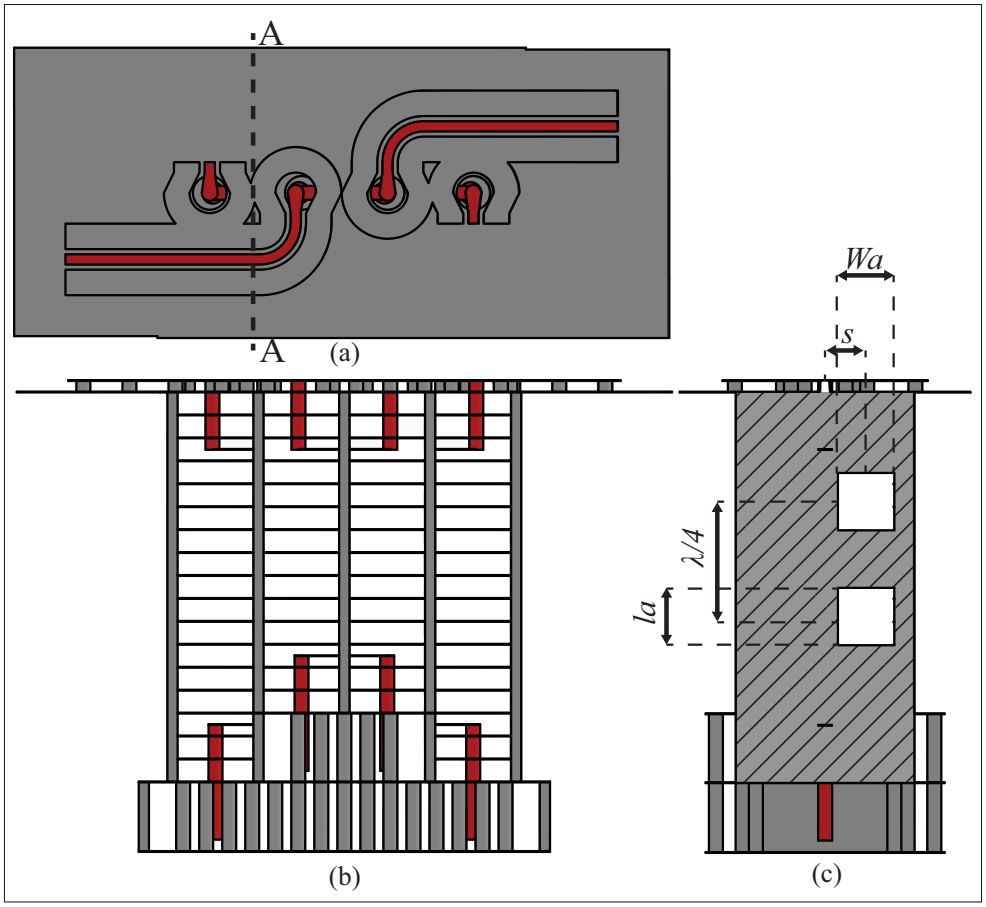

Figure 3.28 Geometry of V-LIW coupler; (a) top view, (b) Side view, and (c) section cut at AA

Furthermore, since the spacing between two slots should be a quarter of guided wavelength, we recommend selecting a width of the V-LIW for that the equivalent waveguide width provides us an integer number of layers for this spacing.

Table. 3.2 lists the coupler's optimized parameter to have a 20 dB coupling at 60 GHz. It is worth mentioning that we have only optimized the width of the slot which was 430 µm in the calculation. The difference is mainly because, in the derivation of the coupling factor, there is an estimation assuming the radiation from a small aperture in a thin metal layer between two waveguides which is not the case here. Fig. 3.29 is the photographs of fabricated coupler with DuPont 9k7 dielectric. The simulation and measurement results of the optimized coupler are illustrated in Fig. 3.30. As it can be seen from this figure, the designed coupler provide about

the 20 dB (22 dB measured) coupling from the 58 GHz to 62 GHz, the return loss, and isolation in this band are better than 17 dB (13.3 dB dB measured) and 32.5 dB (25 dB measured) respectively. It should be noted that the level of coupling is proportional to the size/number of the side apertures. In the vertical arrangement, these parameters are limited by the thickness of the LTCC stack. The more layers we use or the higher frequency we go to, the higher the maximum achievable coupling level becomes.

Table 3.2 Parameters of V-LIW coupler

Parameters	**Value**	**Parameters**	**Value**
LTCC type	Dupont 9k7	Permittivity	7.1
a	1296.5 μm	b	740 μm
$\lambda/4$	$6 \times 112\,\mu m$	s	322.5 μm
l_a	560 μm	w_a	550 μm

3.3.3 V-LIW filter

The substrate integrated waveguide has been widely used in the design of millimeter-waves directed coupled cavity filters (Dancila *et al.*, 2011; Deslandes & Wu, 2003a; Choi *et al.*, 2004; Deslandes & Wu, 2003b; Yun *et al.*, 2005). In these filters, the cavity resonators are usually coupled to each other using iris post walls (Chen & Wu, 2008a) or apertures in case cavities are located in different layers (Hao *et al.*, 2005).

In order to show the suitability of proposed V-LIW in filter realization, we have designed two filters: a simple 5th order fully V-LIW direct coupled resonators filter at W-band and also a 9th order filter at V-band which has the 90-degree bend and transition to CPW.

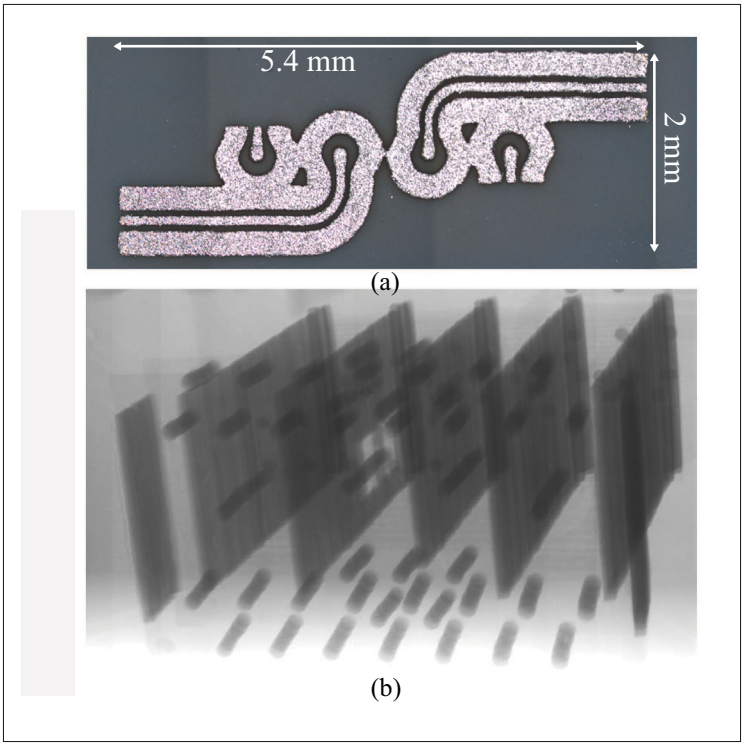

Figure 3.29 Fabricated coupler, (a) top view photograph (b) X-ray photograph of inside of LTCC; the X-ray photo has been taken from downside to show the coupling apertures

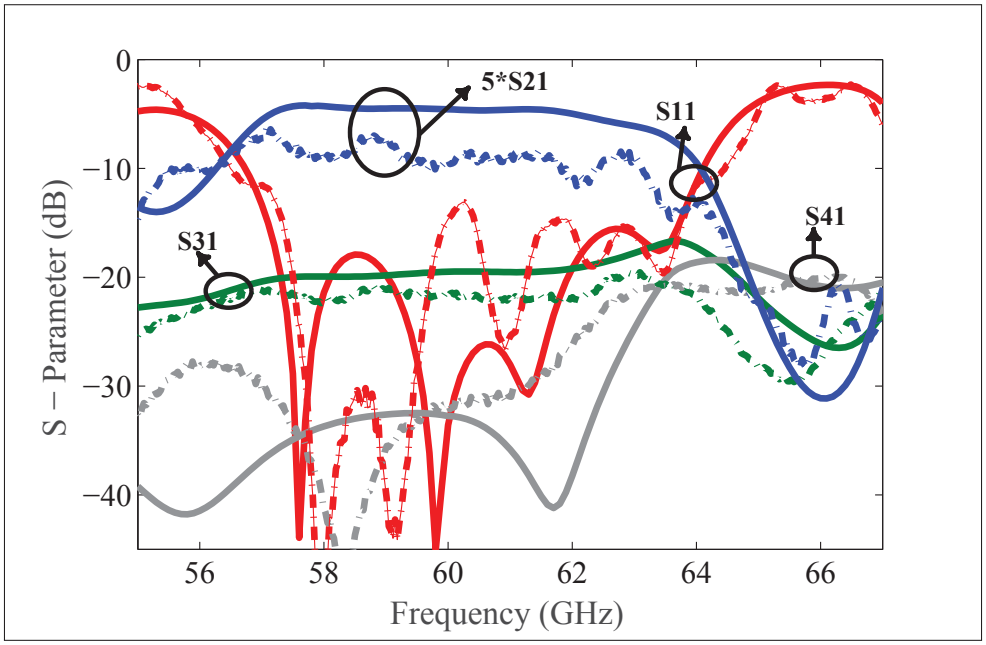

Figure 3.30 Simulation and measurement results of V-LIW coupler; S21 is multiplied by 5 to show more detail

3.3.3.1 5th order W-band Chebyshev filter

The geometry of designed filter based on V-LIW is illustrated in Fig. 3.31. It is composed by five cavity resonators in a row. These cavities are coupled by iris discontinuities which are formed by printed metals. The design parameters of this filter are the length of cavities (li) and irises' opening length (di). In order to determine these parameters, a method that is a combination of the methods in (Bui *et al.*, 1984) and (Cohn, 1957) has been used. The design procedure is quite straightforward and it can be summarized in the following steps.

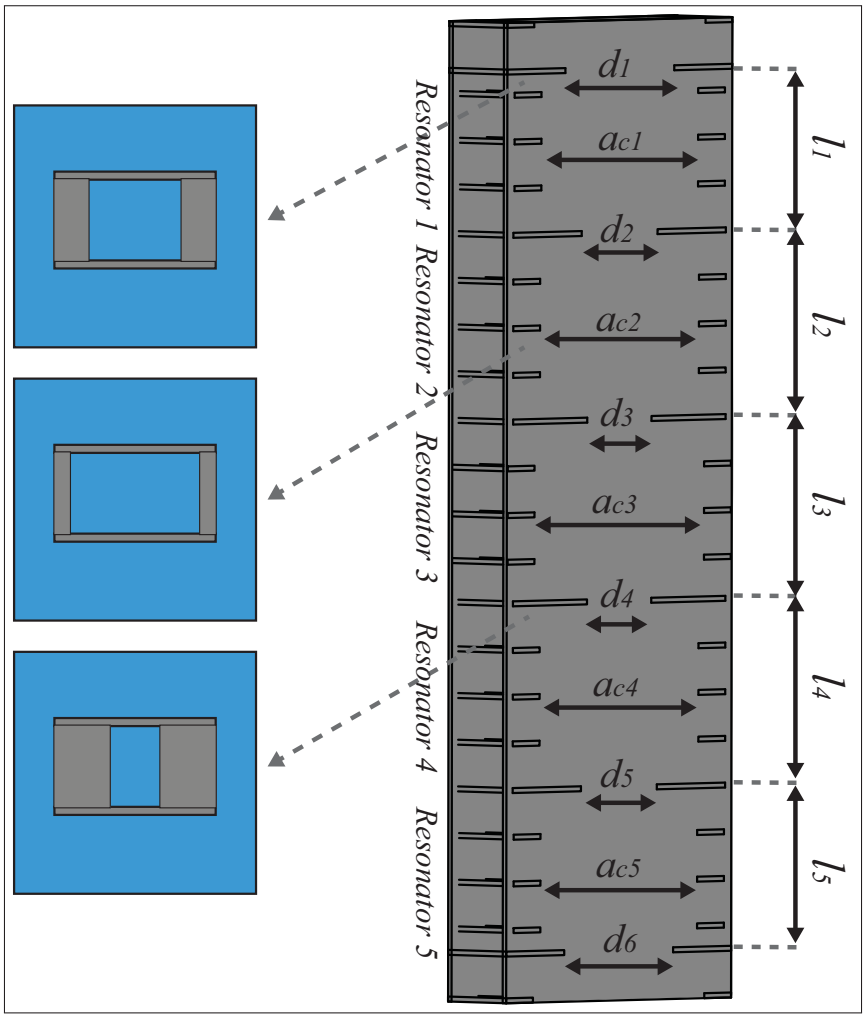

Figure 3.31 Geometry of V-LIW 5th order W-band filter and sample layers

Step 1: Solve (3.8) to determine the mid-band guided wavelength λ_0.

$$\lambda_{gl} sin(\frac{\pi\lambda_{g0}}{\lambda_{gl}}) + \lambda_{gh} sin(\frac{\pi\lambda_{g0}}{\lambda_{gh}}) = 0 \tag{3.8}$$

where λ_{gl} and λ_{gh} are the guided wavelength at lower and upper cut-off frequencies respectively.

Step 2: Find the normalized iris reactances at λ_{g0} by

$$X_{i,i+1} = \frac{\frac{L}{\sqrt{g_i g_{i+1}}}}{1 - \frac{L^2}{g_i g_{i+1}}} \quad i = 0 : n \tag{3.9}$$

where n is the order of the filter, g_i is the Chebyshev's low pass i^{th} element (Cohn, 1957) and L is defined by

$$L = \frac{\pi}{\omega'} \left[\frac{\lambda_{gl} - \lambda_{gh}}{\lambda_{gl} + \lambda_{gh}} \right] \tag{3.10}$$

in which ω' is the pass-band edge of the prototype low-pass filter.

Step 3: Determine the length of cavity resonators (l_{ci}) by

$$l_{ci} = \frac{\lambda_{g0}}{2} - \frac{\lambda_{g0}}{4\pi} \left[tan^{-1}\left[2X_{i+1}\right] + tan^{-1}\left[2X_i\right] \right] \tag{3.11}$$

Step 4: Obtain the iris's opening length (d_i). This is accomplished by finding d_i for which (3.12) provides us the same X_i as in step 2 (Marcuvitz, 1951).

$$\begin{aligned} X_i = & \frac{a}{\lambda_{g0}} tan^2 \frac{\pi d}{2a} \left[1 + \frac{3}{4} \left[\frac{1}{\sqrt{1 - \left(\frac{2a}{3\lambda}\right)^2}} - 1 \right] sin^2 \frac{\pi d}{a} \right. \\ & \left. + 2\left(\frac{a}{\lambda}\right)^2 \left[1 - \frac{4}{\pi} \frac{E(\alpha) - \beta^2 F(\alpha)}{\alpha^2} . \frac{E(\beta) - \alpha^2 F(\beta)}{\beta^2} - \frac{1}{12} sin^2 \frac{\pi d}{a} \right] \right] \end{aligned} \tag{3.12}$$

where α is $sin(\frac{\pi d}{2a})$, β is $cos(\frac{\pi d}{2a})$, and $F(\alpha)$ and $E(\alpha)$ are complete elliptic integrals of the first and second kind, respectively.

The design procedure is completed in step 4, however in most cases (3.11) leads to cavity lengths that are not possible to realize by a discrete number of layers. To address this problem, we assign closest feasible thickness as the cavity length and then modify the correspondent cavity width to keep resonance frequency the same at each resonator using following equation:

$$a_{ci} = \frac{1}{\sqrt{(\frac{1}{l_{ci}})^2 + \frac{1}{a}^2 - (\frac{1}{l_i})^2}} \tag{3.13}$$

where a_{ci} is the width of i^{th} cavity.

This procedure has been used to design a filter with an operation bandwidth from 87 GHz to 98 GHz and the passband ripples of 0.005 dB. Ferro A6M LTCC sheets with the dielectric constant of 6.21 and thickness of 93.98 µm have been utilized. An initial width of 960 µm has been chosen for the first and last sections of the V-LIW filter to be consistent with the one in V-LIW transition for W-band. Table 3.3 includes all parameters have been calculated following steps in design procedure.

The designed filter is then simulated and optimized using ANSYS HFSS. The optimized values of V-LIW width and iris' opening length along with associated errors are listed in Table 3.4. It should be noted that the error in the calculation of d_i is mainly due to the fact that (3.12) has been found for discontinuities between cavities with identical width, while in our case, as we discussed above, we have modified the width of V-LIW.

3.3.3.2 9th order V-band Chebyshev filter

The previous filter shows the excellent performance of V-LIW in filter design, however, that configuration is not suitable to be integrated with other components of a communication circuit. In a new model, we combine the proposed transitions in section III and the iris openings which

Table 3.3 Parameters of W-Band V-LIW filter from theoretical method

i	g_i	$X_{i-1,i}$	$l_{ci}\,(\mu m)$	$d_i\,(\mu m)$	$l_i\,(\mu m)$	$a_{ci}\,(\mu m)$
1	0.9984	0.9346	618.53	678.83	657.86	848.71
2	1.3745	0.3375	724.93	498.52	751.84	905.78
3	1.8283	0.2383	756.66	418.38	751.84	970.95
4	1.3745	0.2383	724.93	418.38	751.84	905.78
5	0.9984	0.3375	618.53	498.52	657.86	848.71
6	-	0.9346	-	678.83	–	–

Table 3.4 V-LIW pptimized dimensions and relative errors to the theoretical method

i	$d_i\,(\mu m)$	$Error\,(\%)$	$a_{ci}\,(\mu m)$	$Error\,(\%)$
1	610	10.13	878	3.45
2	425	14.74	890	1.74
3	360	13.95	950	2.15
4	360	13.95	890	1.74
5	425	14.74	878	3.45
6	610	10.13	–	–

have also been used in W-band filter to realize a filter with co-planar inputs in the same plane. Fig. 3.33 depicts the proposed filter. This filter has four sections: (i) CPW to V-LIW transitions, (ii) V-LIW sections, (iii) V-LIW to H-LIW transition (iv) H-LIW section. The iris openings and inductive posts are located in V-LIW and H-LIW sections respectively to form cavity resonators. Therefore, the transition sections are also used as resonators which leads to having more compact design.

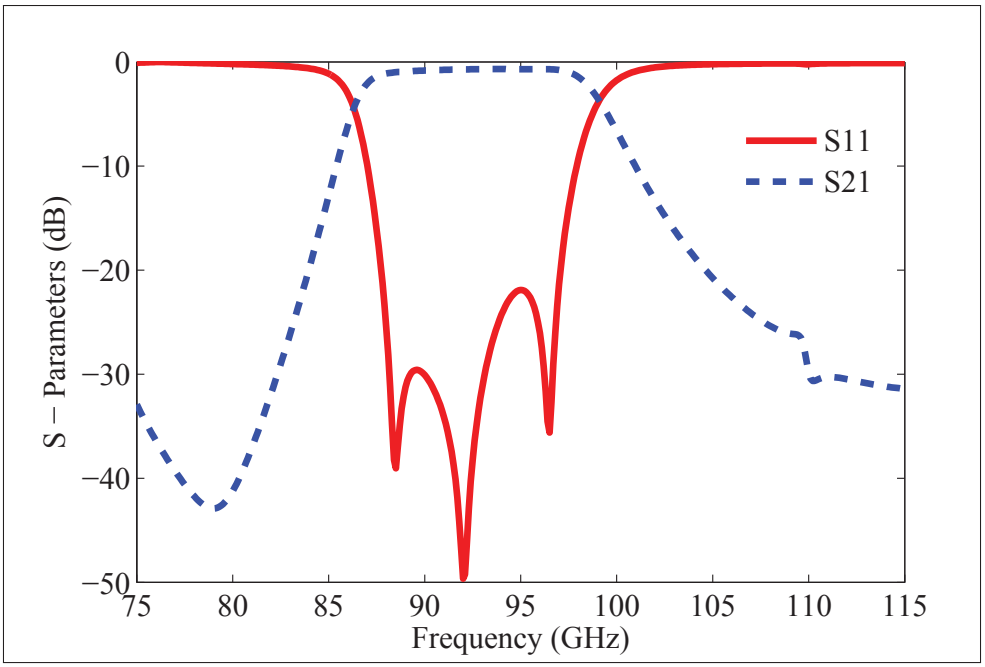

Figure 3.32 Simulation results of W-band V-LIW 5th order filter

The drawback of this new structure is, we achieve a more convenient design for integration, at the expense of a more complicated structure which makes almost impossible to provide a fully analytical design procedure. To find an acceptable starting point for optimization, one can follow the previous design procedure with certain considerations as below:

I: In the first (and last) resonator, the designed transition from CPW to V-LIW should be added. Then the position of this transition in the XY plane and also the aperture diameter where the signal via comes into the V-LIW have to be adjusted to provide the external quality factor (Q_{ext}) and coupling factor (k) given by Harle (2003):

$$Q_{ext\,in} = \frac{g_0 g_1 f_0}{BW} \tag{3.14}$$

$$Q_{ext\,out} = \frac{g_n g_{n+1} f_0}{BW} \tag{3.15}$$

$$k_{i,i+1} = \frac{BW}{f_0}\sqrt{\frac{1}{g_0 g_{i+1}}} \tag{3.16}$$

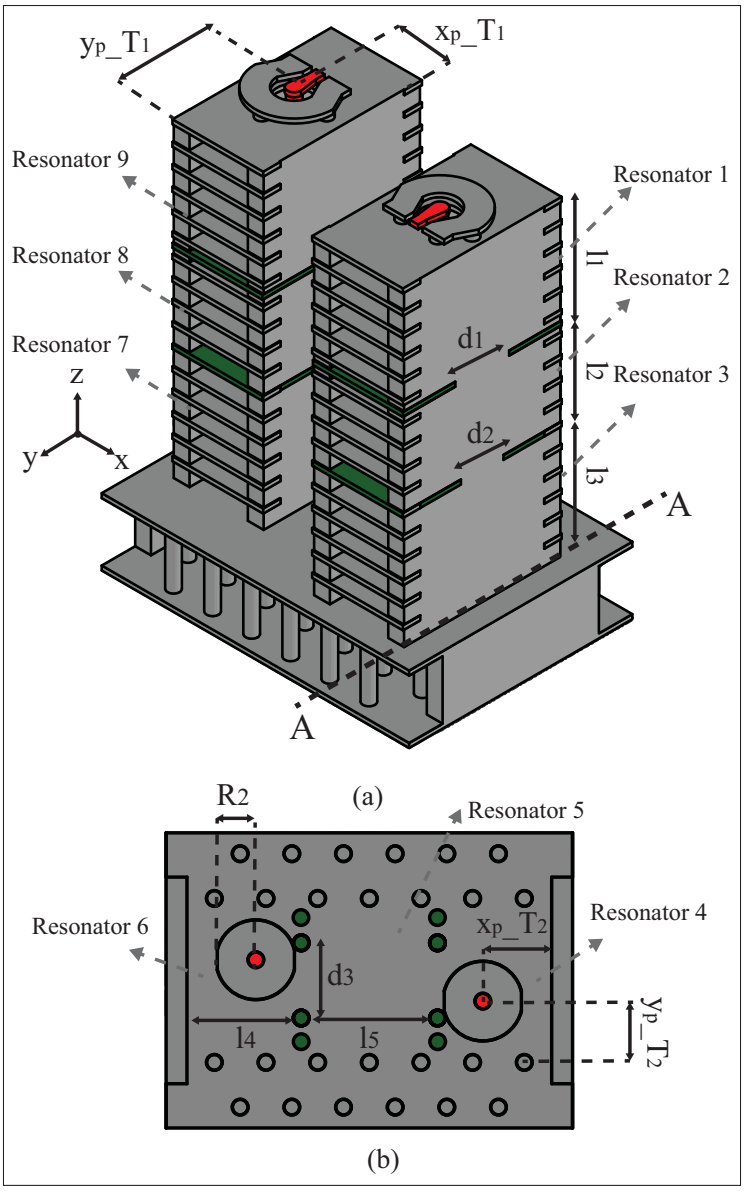

Figure 3.33 Geometry of 9th order V-LIW filter.
The green parts are iris discontinuities
(a) 3D view (b) section cut at AA

where BW is the bandwidth and f_0 is the center frequency corresponding to mid-band guided wavelength found by (3.8). The external quality factor for this resonators can be extracted from ANSYS HFSS simulation in association with a MATLAB code. This code has been written by authors based on (Kajfez, 2005).

II: For the second transition, between V-LIW and H-LIW, like the first transition, with adjusting the lateral position of transition and the aperture diameter, the desired coupling between third and fourth resonators can be achieved. It should be noted that the lengths of these cavities have to be optimized at the same time to keep the resonance frequency of the coupled resonators unchanged.

III: Two inductive posts are used to realize the coupling between fourth and fifth resonators. The distance between these two posts determines the level of coupling. This distance can be estimated by (3.12) and then applying the formula for effective width of SIW, presented in (Xu & Wu, 2005b).

Applying the presented method, we have designed and optimized a filter for unlicensed 60 GHz applications. The filter is targeted at 58 GHz to 62 GHz with pass-band ripples of 0.005 dB. The filter has been designed following the analytical procedure presented in the previous part of this section, then the steps, presented here, carried out one by one to have a fast and accurate optimization. Dupont 9k7 LTCC tapes with a permittivity of 7.1 are used to realize the desired filter. The LIW width in both sections, V-LIW and H-LIW, is 1428 μm. Table 3.5 includes the optimized dimensions for proposed filter, the dimensions which are not listed in this table can be found from either symmetry of the filter or dimensions for the transitions presented in previous sections.

Fig. 3.34 shows the simulation and fabrication of the V-LIW V-band filter. As it can be seen from this figure, the results are in good agreement. The measured filter has a return loss of better than 15 dB over the entire unlicensed band and an insertion loss of 2.1 dB at 60 GHz. A photograph of fabricated filter and an X-ray photograph of inside LTCC are illustrated in Fig. 3.35.

3.4 Conclusion

In this paper, we proposed a new guiding structure, named Vertical LTCC Integrated Waveguide (V-LIW), for multi-layer fabrication technologies. The proposed transmission line allows

Table 3.5 Parameters of V-Band V-LIW 9th order filter

Parameters	**Value**	**Parameters**	**Value**
$l1$	$1232\,\mu m$	$d3$	$655\,\mu m$
$l2$	$1008\,\mu m$	$x_p\_T_1$	$366\,\mu m$
$l3$	$1344\,\mu m$	$y_p\_T_1$	$714\,\mu m$
$l4$	$995\,\mu m$	$x_p\_T_2$	$600\,\mu m$
$l5$	$1187\,\mu m$	$y_p\_T_2$	$534\,\mu m$
$d1$	$620\,\mu m$	$R1$	$202.5\,\mu m$
$d2$	$490\,\mu m$	$R2$	$136\,\mu m$

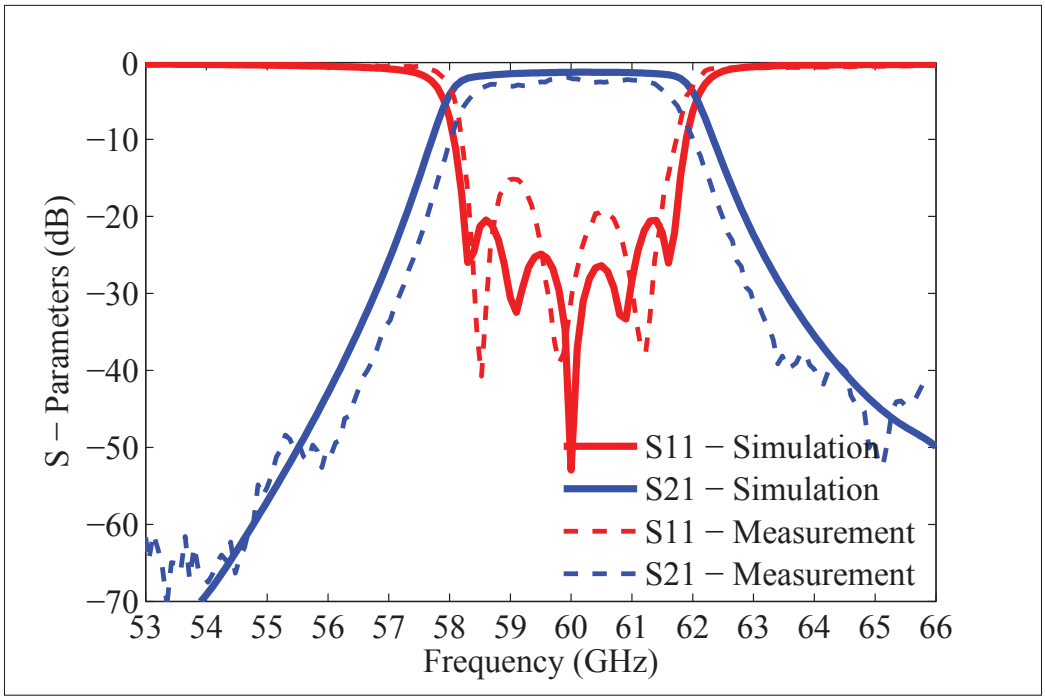

Figure 3.34 Simulation and measurement results for V-band V-LIW filter

us to integrate the passive components in the perpendicular direction to the surface. The characteristics of V-LIW are fully presented, and three different transitions have also been proposed to interconnect this line to the standard rectangular waveguides, coplanar waveguides, and con-

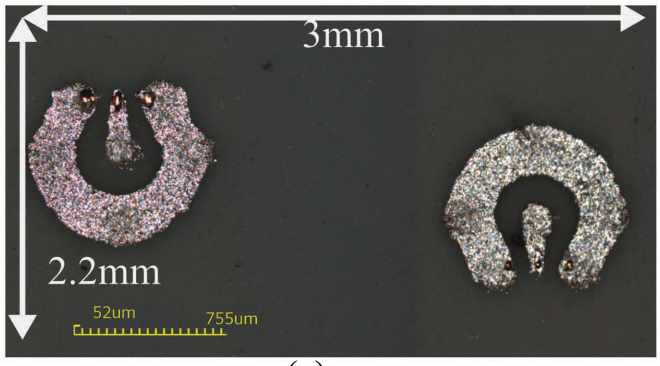

Figure 3.35 Fabricated V-band V-LIW filter (a) top view photograph, and (b) X-ray photograph of inside of LTCC filter

ventional horizontal SIW. Furthermore, the superior capabilities of V-LIW for designing compact 3D circuits have been demonstrated through designing different elementary components: two Filters, T-Junction power divider, and a coupler. The transitions, as well as the 3D circuits, are successfully fabricated and measured in LTCC. The authors envision that the proposed V-LIW to be an excellent candidate for the millimeter-wave compact 3D circuits, where highly integrated low loss structures are desired.

CONCLUSION AND RECOMMENDATIONS

In this thesis we investigated different solutions to improve performance of different circuity realized with low temperature co-fired ceramic (LTCC) technology at microwave and milimeter-wave frequencies. The ultimate objective was to advance the current realization techniques and process to design ultra low-loss and highly compact components and circuits which are required by the next generation of system-on-package solutions for upcoming services like 5G. It has been successfully shown through test and measurement that using our proposed structures, one can design passive circuits with functionalities and performances which are not offered by other techniques and technologies.

In the first part of thesis, a structure to realize suspended and virtually thick conductors has been proposed. Using this technique, several dielectric-free suspended lumped element inductors and capacitors have been designed and tested. These lumped components have shown significantly better performance compared to the exact same components fabricated by conventional methodso. Also, these components outperform all the reported lumped components in the literature in terms of quality factor and self resonance frequency which are the two key parameters to compare the performance of lumped elements. With the aid of these high SRF components, a band-pass lumped element Ku-band filter has been designed and successfully measured. The realization of this filter has shown that using the proposed structure the band in which the lumped components are applicable has been broaden at least twice time. In fact, we showed that using this technique, lumped element circuits can be realized at Ku-Band and potentially even higher frequencies before the size of components become too small to be fabricated.

In the second part of the thesis, a novel structure has been proposed to realized empty LTCC integrated waveguide (E-LIW). In this guiding structure, the inside dielectric has been completely removed which eliminates the dielectric loss and provide an ultra low-loss interconnec-

tion. Furthermore, a novel transition from (E-LIW) to dielectric-filled waveguide and CPW has been proposed. This transition has shown better performance while it is significantly shorter than other transitions used in the similar waveguides in the literature. A back to back transition using the proposed transition and E-LIW has been fabricated and successfully tested. This waveguide and the transitions are well-suited for interconnections and circuitries at millimeter-wave and above. At lower frequencies, the size of E-LIW become too large to be an interesting guiding structure.

In the third part of this thesis, a new guiding structure has been proposed to transfer signal in the perpendicular direction to the surface. This new transmission line, dubbed vertical LTCC integrated waveguide (V-LIW), enables us to design out-of-plane structures like E-Plane power divider for which conventional methods do not provide any fully embedded solutions. Moreover, V-LIW helps to use less foot-print area which is very valuable in small SOP module for placing active devices. A set of waveguide transitions and discontinues have been designed and presented to complete this waveguide's family. This includes a transition to standard waveguide, a transition to planar waveguide, a 90 degrees bend (transition to conventional LIW), and a T-junction. Using these blocks, three elementary passive components including a power divider, a coupler and a filter have been designed and successfully tested at V-band frequencies. It should be noted that, waveguide and passive components designed by V-LIW are particularly of interest at V-band and above where the dielectric could be thick enough to realize vertical structures.

For the future work, we see many research opportunities in this field. While in the dielectric-free suspended lumped elements and E-LIW transmission line the dielectric loss is removed, the conductor loss is still present and untouched. The conductor loss can be reduced by reducing surface roughness and also be increasing the skin depth at the band of interest. The surface finish could be improved by polishing the LTCC surface and sputtering conductors. Also, one

can increase the effective skin depth by making the conductor multi thin layers. Moreover, while several passive circuits using V-LIW have been presented in this thesis, one can design plenty of other structures using this new guiding structure. A millimeter-wave corrugated horn antenna or a duplexer are interesting options to be consider for this purpose. Also, with the same manner, one can realize the circular integrated waveguide as well which is very interesting considering circular waveguide in TE11 mode has the best loss performance. Moreover, realization of integrated tall waveguide can be consider to improve loss performance at very high frequencies like terahertz.

REFERENCES

ANSYS HFSS (Version 18.0.0). Consulted at http://www.ansys.com.

HFWorks (Version 5.0.0). Consulted at https://www.emworks.com.

Aliouane, S., Kouki, A. B. & Aigner, R. (2011, June). Very-high-Q solenoid RF inductors for SiP LTCC integration. *2011 IEEE MTT-S International Microwave Symposium*, pp. 1-1. doi: 10.1109/MWSYM.2011.5973469.

Bahl, I. J. (2003). *Lumped elements for RF and microwave circuits*. Artech house.

Bahloul, D., Amar, A. B. & Kouki, A. B. (2016). MEMS fabrication on LTCC substrates for RF applications: challenges and perspectives. *Additional papers and presentations*, 2016(CICMT), 000089–000094.

Belenguer, A., Esteban, H. & Boria, V. E. (2014). Novel empty substrate integrated waveguide for high-performance microwave integrated circuits. *IEEE transactions on microwave theory and techniques*, 62(4), 832–839.

Brown, R. L., Shapiro, A. A. & Polinski, P. W. (1993). Integration of passive components into MCMs using advanced low-temperature cofired ceramics. *International journal of microcircuits and electronic packaging*, 16(4), 328–338.

Brzezina, G., Roy, L. & MacEachern, L. (2009). Design enhancement of miniature lumped-element LTCC bandpass filters. *IEEE transactions on microwave theory and techniques*, 57(4), 815-823. doi: 10.1109/TMTT.2009.2015035.

Brzezina, G. & Roy, L. (2014). Miniaturized, lumped-element filters for customized system-on-package L-band receivers. *IEEE transactions on components, packaging and manufacturing technology*, 4(1), 26–36.

Bui, L. Q., Ball, D. & Itoh, T. (1984). Broad-band millimeter-wave e-plane bandpass filters (short papers). *IEEE transactions on microwave theory and techniques*, 32(12), 1655-1658. doi: 10.1109/TMTT.1984.1132908.

Cassivi, Y., Perregrini, L., Arcioni, P., Bressan, M., Wu, K. & Conciauro, G. (2002). Dispersion characteristics of substrate integrated rectangular waveguide. *IEEE microwave and wireless components letters*, 12(9), 333–335.

Chapra, S. C. (2005). Applied numerical methods with MATLAB for engineers and scientists. mcgraw-hill international edition.

Che, W., Deng, K., Wang, D. & Chow, Y. (2008a). Analytical equivalence between substrate-integrated waveguide and rectangular waveguide. *IET microwaves, antennas & propagation*, 2(1), 35–41.

Che, W., Deng, K., Wang, D. & Chow, Y. (2008b). Analytical equivalence between substrate-integrated waveguide and rectangular waveguide. *IET microwaves, antennas & propagation*, 2(1), 35–41.

Chen, X. P. & Wu, K. (2008a). Substrate integrated waveguide cross-coupled filter with negative coupling structure. *IEEE transactions on microwave theory and techniques*, 56(1), 142-149. doi: 10.1109/TMTT.2007.912222.

Chen, X.-P. & Wu, K. (2008b). Substrate integrated waveguide cross-coupled filter with negative coupling structure. *IEEE transactions on microwave theory and techniques*, 56(1), 142–149.

Cheng, Y. J., Bao, X. Y. & Guo, Y. X. (2013). 60-GHz LTCC miniaturized substrate integrated multibeam array antenna with multiple polarizations. *IEEE transactions on antennas and propagation*, 61(12), 5958-5967. doi: 10.1109/TAP.2013.2280873.

Cheng, Y. J., Hong, W. & Wu, K. (2010). Broadband self-compensating phase shifter combining delay line and equal-length unequal-width phaser. *IEEE transactions on microwave theory and techniques*, 58(1), 203–210.

Cheng, Y. J., Hong, W. & Wu, K. (2012). 94 GHz substrate integrated monopulse antenna array. *IEEE transactions on antennas and propagation*, 60(1), 121–129.

Choi, S. T., Yang, K. S., Tokuda, K. & Kim, Y. H. (2004). A V-band planar narrow bandpass filter using a new type integrated waveguide transition. *IEEE microwave and wireless components letters*, 14(12), 545-547. doi: 10.1109/LMWC.2004.837386.

Cohn, S. B. (1957). Direct-coupled-resonator filters. *Proceedings of the IRE*, 45(2), 187–196.

Dancila, D., Rottenberg, X., Tilmans, H. A. C., Raedt, W. D. & Huynen, I. (2011, Sept). 64 GHz seven-pole bandpass filter substrate integrated waveguide (SIW) in LTCC. *2011 IEEE MTT-S international microwave workshop series on millimeter wave integration technologies*, pp. 200-203. doi: 10.1109/IMWS3.2011.6061876.

Degerstrom, M., Gilbert, B. K. & Daniel, E. (2008). Accurate resistance, inductance, capacitance, and conductance (RLCG) from uniform transmission line measurements. *Electrical performance of electronic packaging, 2008 IEEE-EPEP*, pp. 77–80.

Delaney, K., Barrett, J., Barton, J. & Doyle, R. (1999). Characterization and performance prediction for integral capacitors in low temperature co-fired ceramic technology. *IEEE transactions on advanced packaging*, 22(1), 68–77.

Deshpande, M. D., Das, B. N. & Sanyal, G. S. (1979). Analysis of an end launcher for anX-band rectangular waveguide. *Ieee trans. microw. theory tech.*, 27, 731-735.

Deslandes, D. & Wu, K. (2003a). Single-substrate integration technique of planar circuits and waveguide filters. *IEEE transactions on microwave theory and techniques*, 51(2), 593-596. doi: 10.1109/TMTT.2002.807820.

Deslandes, D. & Wu, K. (2003b, May). Millimeter-wave substrate integrated waveguide filters. *CCECE 2003 - canadian conference on electrical and computer engineering. toward a caring and humane technology (cat. no.03ch37436)*, 3, 1917-1920 vol.3. doi: 10.1109/CCECE.2003.1226288.

Deslandes, D. & Wu, K. (2005). Analysis and design of current probe transition from grounded coplanar to substrate integrated rectangular waveguides. *IEEE transactions on microwave theory and techniques*, 53(8), 2487-2494. doi: 10.1109/TMTT.2005.852778.

Deslandes, D. & Wu, K. (2001a). Integrated microstrip and rectangular waveguide in planar form. *IEEE microwave and wireless components letters*, 11(2), 68–70.

Deslandes, D. & Wu, K. (2001b). Integrated microstrip and rectangular waveguide in planar form. *IEEE microwave and wireless components letters*, 11(2), 68–70.

Deslandes, D. & Wu, K. (2002). Design consideration and performance analysis of substrate integrated waveguide components. *Microwave conference, 2002. 32nd european*, pp. 1–4.

Deslandes, D. & Wu, K. (2006). Accurate modeling, wave mechanisms, and design considerations of a substrate integrated waveguide. *IEEE transactions on microwave theory and techniques*, 54(6), 2516–2526.

Doghri, A., Ghiotto, A., Djerafi, T. & Wu, K. (2012a, June). Compact and low cost substrate integrated waveguide cavity and bandpass filter using surface mount shorting stubs. *2012 IEEE/MTT-S international microwave symposium digest*, pp. 1-3. doi: 10.1109/MWSYM.2012.6259778.

Doghri, A., Ghiotto, A., Djerafi, T. & Wu, K. (2012b, Dec). Corrugated SIW L-folded antipodal parabolic tapered slot antenna. *2012 asia pacific microwave conference proceedings*, pp. 893-895. doi: 10.1109/APMC.2012.6421770.

Doghri, A., Djerafi, T., Ghiotto, A. & Wu, K. (2013, Oct). Schwinger coupler for substrate integrated circuits and systems. *2013 european microwave conference*, pp. 306-309.

Doghri, A., Djerafi, T., Ghiotto, A. & Wu, K. (2015). Substrate integrated waveguide directional couplers for compact three-dimensional integrated circuits. *IEEE transactions on microwave theory and techniques*, 63(1), 209–221.

Eun, K. C., Lee, Y. C., Lee, J. W., Song, M. S. & Park, C. S. (2004, June). Fully embedded LTCC spiral inductors incorporating air cavity for high Q-factor and SRF. *2004 proceedings. 54th electronic components and technology conference (IEEE Cat. No.04CH37546)*, 1, 1101-1103 Vol.1. doi: 10.1109/ECTC.2004.1319477.

Eurskens, W., Wersing, W., Gohlke, S., Wannemnacher, V., Hild, P. & Weigel, R. (1998, June). Design and performance of UHF band inductors, capacitors and resonators using LTCC technology for mobile communication systems. *1998 IEEE MTT-S international microwave symposium digest (cat. no.98ch36192)*, 3, 1285-1288 vol.3. doi: 10.1109/MWSYM.1998.700609.

Fabregas, I., Shamsaifar, K. & Rebollar, J. M. (1992, June). Coaxial to rectangular waveguide transitions. *Antennas and propagation society international symposium, 1992. ap-s. 1992 digest. held in conjuction with: URSI radio science meeting and nuclear EMP meeting., IEEE*, pp. 2122-2125 vol.4. doi: 10.1109/APS.1992.221447.

Germain, S., Deslandes, D. & Wu, K. (2003). Development of substrate integrated waveguide power dividers. *Electrical and computer engineering, 2003. IEEE CCECE 2003. canadian conference on*, 3, 1921–1924.

Gravel, N. LTCC process design rules.

Hao, Z. C., Hong, W., Chen, X. P., Chen, J. X., Wu, K. & Cui, T. J. (2005). Multilayered substrate integrated waveguide (MSIW) elliptic filter. *IEEE microwave and wireless components letters*, 15(2), 95-97. doi: 10.1109/LMWC.2004.842836.

Harle, L. (2003). *Microwave micromachined cavity filters*. (Ph. D. thesis, Citeseer).

Heilala, J., Keränen, K., Mäkinen, J.-T., Väätäinen, O., Kautio, K., Voho, P. & Karioja, P. (2005). LTCC technology for cost-effective packaging of photonic modules. *Assembly automation*, 25(1), 30–37.

Henry, M., Osman, N., Tick, T. & Free, C. (2008). Integrated air-filled waveguide antennas in LTCC for G-band operation. *Microwave conference, 2008. APMC 2008. asia-pacific*, pp. 1–4.

Hirokawa, J., Sakurai, K., Ando, M. & Goto, N. (1991). An analysis of a waveguide t junction with an inductive post. *IEEE transactions on microwave theory and techniques*, 39(3), 563-566. doi: 10.1109/22.75301.

Huang, Y. & Wu, K.-L. (2003). A broad-band LTCC integrated transition of laminated waveguide to air-filled waveguide for millimeter-wave applications. *IEEE transactions on microwave theory and techniques*, 51(5), 1613–1617.

Huang, Y., Wu, K.-L. & Ehlert, M. (2003). An integrated LTCC laminated waveguide-to-microstrip line t-junction. *IEEE microwave and wireless components letters*, 13(8), 338–339.

Imanaka, Y. (2005). *Multilayered low temperature cofired ceramics (LTCC) technology*. Springer Science & Business Media.

Imhof, H. & Schless, T. (2007). Interconnection substrates and passive integration – ceramic. *Component/subsystem technologies*.

Isapour, A. Q-factor extraction by MATLAB using Kajfez method. Consulted at http://ltcc.etsmtl.ca/examples.aspx.

Isapour, A. & Kouki, A. B. (2017). Empty LTCC integrated waveguide with compact transitions for ultra-low loss millimeter-wave applications. *IEEE microwave and wireless components letters*, 27(2), 144–146.

Joshi, H. & Chappell, W. J. (2006). Dual-band lumped-element bandpass filter. *IEEE transactions on microwave theory and techniques*, 54(12), 4169–4177.

Kajfez, D. (2005). *Q-factor*. Wiley Online Library.

keysight. VNA measurement uncertainty calculator.

Khatib, B. Y. E., Djerafi, T. & Wu, K. (2012). Substrate-integrated waveguide vertical interconnects for 3-D integrated circuits. *IEEE transactions on components, packaging and manufacturing technology*, 2(9), 1526-1535. doi: 10.1109/TCPMT.2012.2196516.

Kim, K.-I., Kim, J.-M., Kim, J.-M., Hwang, G.-C., Baek, C.-W. & Kim, Y.-K. (2005). Packaging for RF MEMS devices using LTCC substrate and BCB adhesive layer. *Journal of micromechanics and microengineering*, 16(1), 150.

Lazarus, M. (2010). The great spectrum famine. *IEEE spectrum*, 47(10), 26-31. doi: 10.1109/MSPEC.2010.5583459.

Lee, J.-H., DeJean, G., Sarkar, S., Pinel, S., Lim, K., Papapolymerou, J., Laskar, J. & Tentzeris, M. M. (2005). Highly integrated millimeter-wave passive components using 3-D LTCC system-on-package (SOP) technology. *IEEE transactions on microwave theory and techniques*, 53(6), 2220–2229.

Li, H., Hong, W., Cui, T. J., Wu, K., Zhang, Y. L. & Yan, L. (2003, June). Propagation characteristics of substrate integrated waveguide based on LTCC. *IEEE MTT-S international microwave symposium digest, 2003*, 3, 2045-2048 vol.3. doi: 10.1109/MWSYM.2003.1210562.

Lin, Y.-S., Liu, C.-C., Li, K.-M. & Chen, C. H. (2004). Design of an LTCC tri-band transceiver module for GPRS mobile applications. *IEEE transactions on microwave theory and techniques*, 52(12), 2718–2724.

Marcuvitz, N. (1951). *Waveguide handbook*. IET.

Montgomery, C. G., Dicke, R. H. & Purcell, E. M. (1948). *Principles of microwave circuits*. IET.

Mousavi, S. H. & Kouki, A. B. (2015). High-SRF VHF/UHF Lumped Elements in LTCC. *IEEE Microwave and Wireless Components Letters*, 25(1), 25–27.

Mousavi, S. H. & Kouki, A. B. (2016). Highly compact vhf/uhf dual-band/dual-function ltcc circuits: application to avionic systems. *IEEE Transactions on Components, Packaging and Manufacturing Technology*, 6(1), 12–22.

Mukherjee, S., Chongder, P., Srivastava, K. V. & Biswas, A. (2013, Nov). Design of a broadband coaxial to substrate integrated waveguide (SIW) transition. *2013 asia-pacific microwave conference proceedings (APMC)*, pp. 896-898. doi: 10.1109/APMC.2013.6694966.

Mumford, W. W. (1953). The optimum piston position for wide-band coaxial-to-waveguide transducers. *Proceedings of the IRE*, 41(2), 256-261. doi: 10.1109/JRPROC.1953.274216.

MuRata. Low Temperature Co-fired Ceramics (LTCC) Multi-layer Module Boards.

Parment, F., Ghiotto, A., Vuong, T.-P., Duchamp, J.-M. & Wu, K. (2015a). Air-filled substrate integrated waveguide for low-loss and high power-handling millimeter-wave substrate integrated circuits. *IEEE transactions on microwave theory and techniques*, 63(4), 1228–1238.

Parment, F., Ghiotto, A., Vuong, T.-P., Duchamp, J.-M. & Wu, K. (2015b). Air-filled substrate integrated waveguide for low-loss and high power-handling millimeter-wave substrate integrated circuits. *IEEE transactions on microwave theory and techniques*, 63(4), 1228–1238.

Pozar, D. M. (2009). *Microwave engineering*. John Wiley & Sons.

Qian, K. & Tang, X. (2011). Compact dual-band semi-lumped bandpass filter with LTCC technology. *Electronics letters*, 47(13), 755–757.

Ranjkesh, N. & Shahabadi, M. (2006). Reduction of dielectric losses in substrate integrated waveguide. *Electronics letters*, 42(21), 1230–1232.

Saad, S. M. (1990). A more accurate analysis and design of coaxial-to-rectangular waveguide end launcher. *IEEE trans. microw. theory tech.*, 38, 129-134.

Shafique, M. F., Saeed, K., Steenson, D. P. & Robertson, I. D. (2009). Laser prototyping of microwave circuits in LTCC technology. *IEEE Transactions on Microwave Theory and Techniques*, 57(12), 3254–3261.

Shafique, M. & Robertson, I. (2011). Laser prototyping of multilayer LTCC microwave components for system-in-package applications. *IET microwaves, antennas & propagation*, 5(8), 864–869.

Shahvirdi, T. & Banai, A. (2010). Applying contour integral method for analysis of substrate integrated waveguide filters. *Microwave symposium (MMS), 2010 mediterranean*, pp. 418–421.

Singh, A. & verma, S. (2009). *Fundamentals of microwave engineering*. PHI Learning.

Sutono, A., Pham, A., Laskar, J. & Smith, W. R. (1999a). Development of three dimensional ceramic-based MCM inductors for hybrid RF/microwave applications. *1999 IEEE Radio Frequency Integrated Circuits Symposium (Cat No.99CH37001)*, pp. 175-178. doi: 10.1109/RFIC.1999.805265.

Sutono, A., Heo, D., Chen, Y. J. E. & Laskar, J. (2001). High-Q LTCC-based passive library for wireless system-on-package (SOP) module development. *IEEE transactions on microwave theory and techniques*, 49(10), 1715-1724. doi: 10.1109/22.954775.

Sutono, A., Pham, A.-V., Laskar, J. & Smith, W. R. (1999b). RF/microwave characterization of multilayer ceramic-based MCM technology. *IEEE transactions on advanced packaging*, 22(3), 326–331.

Wade, P. (2006). Rectangular Waveguide to Coax Transition Design. Consulted at http://www.w1ghz.org/QEX/Rectangular_Waveguide_to_Coax_Transition_Design.pdf.

Wang, D., s. Chin, K., Che, W., c. Chang, C. & Wu, Y. (2014). 60 ghz duplexer design using dual-mode SIW filters with single-sided transmission zeros. *Electronics letters*, 50(21), 1529-1531. doi: 10.1049/el.2014.1288.

Wang, K., Wong, S. W., Sun, G. H., Chen, Z. N., Zhu, L. & Chu, Q. X. (2016). Synthesis method for substrate-integrated waveguide bandpass filter with even-order chebyshev response. *IEEE transactions on components, packaging and manufacturing technology*, 6(1), 126-135. doi: 10.1109/TCPMT.2015.2502420.

Wheeler, G. (1966). Broadband waveguide-to-coax transitions. *1958 IRE international convention record*, pp. 182-185.

Wilcox, D., Huang, R. & Anderson, D. (1997). The multilayer ceramic integrated circuit technology: Opportunities and challenges. *Int. symposium on microelektronics*, 17.

Williams, D. F. (2010). Rectangular-waveguide vector-network-analyzer calibrations with imperfect test ports. *Microwave measurement symposium (ARFTG), 2010 76th arftg*, pp. 1–8.

Wolff, I. (2007a). Design and technology of microwave and millimeterwave LTCC circuits and systems. *Signals, systems and electronics, 2007. ISSSE'07. international symposium on*, pp. 505–512.

Wolff, I. (2007b). Design and technology of microwave and millimeterwave LTCC circuits and systems. *Signals, systems and electronics, 2007. issse'07. international symposium on*, pp. 505–512.

Wu, J., Coller, D., Anderson, M. J. & Guth, G. (2004). RF SiP technology: integration and innovation. *International conference on compound semiconductor manufacturing*.

Xu, F. & Wu, K. (2005a). Guided-wave and leakage characteristics of substrate integrated waveguide. *IEEE transactions on microwave theory and techniques*, 53(1), 66-73. doi: 10.1109/TMTT.2004.839303.

Xu, F. & Wu, K. (2005b). Guided-wave and leakage characteristics of substrate integrated waveguide. *IEEE transactions on microwave theory and techniques*, 53(1), 66–73.

Yang, S. & Fathy, A. E. (2009). Design equations of arbitrary power split ratio waveguide T-junctions using a curve fitting approach. *International journal of RF and microwave computer-aided engineering*, 19(1), 91–98.

Young, L. (1963). Direct-coupled cavity filters for wide and narrow bandwidths. *IEEE transactions on microwave theory and techniques*, 11(3), 162-178. doi: 10.1109/TMTT.1963.1125629.

Yun, T.-S., Nam, H., Kim, K.-B. & Lee, J.-C. (2005, Dec). Iris waveguide bandpass filter using substrate integrated waveguide (SIW) for satellite communication. *2005 asia-pacific microwave conference proceedings*, 1, 4 pp.-. doi: 10.1109/APMC.2005.1606307.

Zhang, G., Wang, J., Pan, J. & Gu, H. (2015). Compact 60 ghz LTCC balun bandpass filter with two transmission zeroes. *Electronics letters*, 51(8), 637-638. doi: 10.1049/el.2014.4440.

Zhang, Q. & Lu, Y. (2008). E-band "T" shape transitions between substrate integrated waveguide and standard waveguide. *Microwave conference, 2008. APMC 2008. asia-pacific*, pp. 1–4.

Zhou, B., Sheng, W. & Zheng, Y. (2014a). Miniaturized lumped-element LTCC filter with spurious spikes suppressed vertically-interdigital-capacitors. *IEEE microwave and wireless components letters*, 24(10), 692–694.

Zhou, B., Sheng, W. & Zheng, Y. (2014b). Miniaturized lumped-element LTCC filter with spurious spikes suppressed vertically-interdigital-capacitors. *IEEE Microwave and Wireless Components Letters*, 24(10), 692–694.

Zhou, B., Ma, Q., Wang, Q., Yan, L., Zhou, N. & Cheng, C.-H. (2017). Highly intergrated X-band LTCC receiver module. *Progress in electromagnetics research*, 71, 51–58.